Georgia State University

ScholarWorks @ Georgia State University

Geosciences Theses

Department of Geosciences

Spring 5-7-2016

Authigenic Clays used as Terrestrial Climate Proxies: Locality 80, Olduvai Gorge, Tanzania

Alexandra M. Simpson

Follow this and additional works at: https://scholarworks.gsu.edu/geosciences_theses

Recommended Citation

Simpson, Alexandra M., "Authigenic Clays used as Terrestrial Climate Proxies: Locality 80, Olduvai Gorge, Tanzania." Thesis, Georgia State University, 2016.
doi: https://doi.org/10.57709/8528695

This Thesis is brought to you for free and open access by the Department of Geosciences at ScholarWorks @ Georgia State University. It has been accepted for inclusion in Geosciences Theses by an authorized administrator of ScholarWorks @ Georgia State University. For more information, please contact scholarworks@gsu.edu.

AUTHIGENIC CLAYS USED AS TERRESTRIAL CLIMATE PROXIES:

LOCALITY 80, OLDUVAI GORGE, TANZANIA

by

ALEXANDRA MARIE SIMPSON

Under the Direction of Daniel Michael Deocampo, PhD

ABSTRACT

Authigenic clays are potential proxies for paleoclimate change when formed under saline conditions. Between 1.9 -1.7 mya, Olduvai was a closed-hydrologic basin into which Al- and Fe- rich detrital clays were transported from surrounding soils. Authigenic Mg-rich smectite formed within the basin due to chemical alteration in alkaline and saline conditions. 40 samples were chosen from a stratigraphic section in the center of the paleolake and analyzed to characterize the geochemical facies of the material using XRD, EMPA, and FTIR. ~70% of samples were Mg-rich with clay d060 XRD peaks between 1.506-1.523Å. EMPA indicated (Al_2O_3 + Fe_2O_3)/MgO ratios ranged from 0.2-4.8, 21 had ratios >1.0, indicating higher (Al_2O_3 + Fe_2O_3) content. These clay data correlated with bulk XRF data, indicating diagenetic controls on bulk composition. Therefore, bulk geochemistry can potentially indicate paleoclimate change when influenced by Mg-rich phyllosilicate formation.

INDEX WORDS: Clay Mineralogy, Paleoclimate, Limnogeology, Authigenic Clays, Geochemistry

AUTHIGENIC CLAYS USED AS TERRESTRIAL CLIMATE PROXIES:

LOCALITY 80, OLDUVAI GORGE, TANZANIA

by

ALEXANDRA MARIE SIMPSON

A Thesis Submitted in Partial Fulfillment of the Requirements for the Degree of

Master of Science

in the College of Arts and Sciences

Georgia State University

2016

Copyright by
Alexandra Marie Simpson
2016

AUTHIGENIC CLAYS USED AS TERRESTRIAL CLIMATE PROXIES:

LOCALITY 80, OLDUVAI GORGE, TANZANIA

by

ALEXANDRA MARIE SIMPSON

Committee Chair: Daniel Michael Deocampo

Committee: W. Crawford Elliott

Nadine Kabengi

Electronic Version Approved:

Office of Graduate Studies

College of Arts and Sciences

Georgia State University

May 2016

DEDICATION

I'd like to dedicate this thesis to my Mom, who has always been my biggest fan, my cheerleader, and my inspiration. She has taught me how to be strong and independent, to always follow my dreams, and to never be ashamed of who I am and what I am capable of accomplishing. She is an everlasting fountain of support and wisdom, and I am proud and lucky to have been raised by her.

ACKNOWLEDGEMENTS

First and foremost, I would like to thank the Geosciences Department at Georgia State University, not only have I made memories here that I will cherish for the rest of my life, but I have learned more than I could ever imagined and been supported by a wonderful community. To my advisor and mentor, Dr. Deocampo, for his guidance and wisdom. For pushing me but also letting me figure out things on my own, I am and will always be a better scientist for it. To my committee, Dr. Elliott and Dr. Kabengi. To Dr. Elliott for getting me excited and interested about Clay Mineralogy in the first place, and to Dr. Kabengi for providing her expertise on this subject matter.

I'd like to acknowledge the ACACIA grant #EAR-1349599 and the National Science Foundation for providing me with my GRA to conduct this research. As well as NSF grant #EAR-1029020 for the XRD to use at GSU. To Dr. Gail Ashley for being a pioneer in Olduvai research and East African paleolake studies. To Dr. Jeremy Delaney for helping with my EMPA analysis at Rutgers University. Dr. Javier Cuadros at the Natural History Museum in London, for not only letting me visit and conduct my FTIR analysis there, but for guiding me every step of the way. A special thanks to Nate Rabideaux and Karim Minkara, my office mates who helped me stay sane and talk all kinds of nonsense to get through this crazy process.

Finally, I'd like to acknowledge my friends and family for letting me vent, describe, and chat endlessly about my research and this incredible journey. I'm very lucky to have such an incredible support system.

TABLE OF CONTENTS

LIST OF TABLES

LIST OF FIGURES

LIST OF ABBREVIATIONS

Mya……Million Years Ago
Ma……Mega-annum
Mg^{2+}……Magnesium
Al^{3+}……Aluminum
Fe^{2+}……Ferrous Iron
Fe^{3+}……Ferric Iron
K^{+}……Potassium
Si……Silicon
OCI……Octahedral Cation Index
NVH……Ngorongoro Volcanic Highland
EAR……East African Rift
SiO_2……Silicon Dioxide
HCO_3……Bicarbonate
XRF……X-Ray Fluorescence
Al_2O_3……Aluminum Oxide
MgO……Magnesium Oxide
>……Greater than
<……Less than
µm……Micrometer
EMPA……Electron Microprobe Analysis
XRD……X-Ray Diffraction
θ……Theta
λ……Wavelength
mA……Milliamps
kV……Kilovolts
mL……Milliliters
FTIR……Fourier Transform Infrared Spectroscopy
IR……Infrared
cm^{-1}……Reciprocal Wavelength
mg……Milligrams
KBr……Potassium Bromide
Fe_2O_3……Iron (III) Oxide
CaO……Calcium Oxide
OH^{-}……Hydroxide
Å……Angstrom

LIST OF EQUATIONS

1 INTRODUCTION

1.1 African Quaternary Paleoclimate

Paleoenvironmental reconstructions are critical in understanding environmental and climate change, and the relation of these changes to hominin evolution. Currently, detailed records of Milankovitch cycles and monsoonal processes are obtainable through marine sediment cores in regards to major climatic events, but there is still a need for terrestrial records to construct models regarding early human development (Deocampo, 2004). Recent evidence points to early hominin evolution in East Africa as strongly affected by climate change, therefore, the use of paleoenvironmental proxies is imperative to understanding studies of behavior, paleoecology, and evolution of early hominins and other vertebrates (Hay, 1990; Potts, 1996).

The Late Pliocene to Early Pleistocene (1.7-1.9 mya) has been identified as historically significant to hominin evolution and migration according to several theories. The *aridity hypothesis*, which suggests long-term trends towards aridity and the expansion of the savannah over time, pushed the progression of speciation as aridification accelerated (deMenocal, 1995; Reed, 1997; deMenocal, 2004). The *turnover pulse hypothesis*, suggests trends of acute climactic shifts caused speciation and varying levels of migration or adaptation (Vrba et al., 1995; Carto et al., 2009). Additionally, the *variability selection hypothesis*, found in Potts (1999), suggests that episodes of wide climate erraticism enacted adaptive structures and behaviors by hominins in response to environmental change of extreme complexity. These episodes of varying aridity can be linked to changes in the Intertropical Convergence Zone and alterations in the delivery of moisture from the Indian Ocean Monsoon (Trauth et al., 2005; Kingston, 2007). Fluctuations from wetter to more arid climates caused changes in the vertebrate ecosystems and the progression of hominin development (Bobe and Behrensmeyer, 2004; Potts, 1996; Potts, 1998; Potts, 2013).

Quaternary paleolake beds along the East African Rift are important localities of paleontological fossil assemblages of early hominid species (Trauth et al., 2005; Trauth et al., 2009). Within these beds, stratigraphy formed through sediment accumulation and contain potentially sensitive indicators of paleoclimate change and variation (Forester et al., 2012). These proxies can be linked to the identification of climate change variability (Deocampo and Jones, 2013). For quite some time, these proxies have been strictly biotic, such as diatom flora and other biomarkers (Cohen, 2003; Fritz, 2008; Owen et al., 2011). In some cases, environmental conditions can result in a lack of possible proxies for paleolimnology, and raise the need for indicators without the use of preserved biota.

Some of these lakes developed saline and alkaline conditions during the time periods of aridity and low dilute inflow from surrounding areas. Therefore, these hostile conditions resulted in a significant lack of preservation of biotic indicators as proxies for paleoclimatic change (Hay, 1976; Ashley, 2007; Ashley et al., 2009). Paleolakes along the East African Rift hold stratigraphic successions of various environmental indicators (Ashley, 2007). Some of these lakes held highly concentrated water for long periods of time, allowing authigenic facies to form that may be associated with specific paleoclimate conditions.

1.2 Authigenic Clay Minerals in Saline Lakes

Sedimentary processes subject deposited material to alteration due to factors such as sedimentary structure, climate variation, and depositional environment. Marine, lacustrine, and fluvial environments can cause interactions with detrital minerals and water, forming *in situ* mineral facies (Boggs, 1995). Clay minerals, being subject to alteration, are associated with Earth processes that are found near the Earth's surface due to the need for thermodynamic stability during formation and phase change (Weaver and Pollard, 1973; Meunier, 2005; Deocampo, 2015).

When considering the aqueous geochemistry of surface water, the main controls are 1) geology of host rock; 2) surrounding climate; and 3) hydrology of the surface water in question, which can be

related to tectonics, e.g. forming closed basins. When these clays form *in situ*, they can have a direct effect on the elemental budgets of the pore fluids and waters involved with mineral precipitation (Bristow et al., 2012). In hydrologically-closed lakes, the degree of ion concentration of lake water is much higher, and therefore can precipitate and diagenetically alter minerals in higher abundances than in other lacustrine settings (Leng and Marshall, 2004).

Some intervals of the Green River Formation in the western part of the United States are dominated by authigenic silicates, including Mg-rich smectite, formed over a period of 8 Ma due to several fluctuations in arid to humid climate conditions, forming more authigenic minerals during dry periods due to higher ion concentration in the lake water during diagenesis (Bradley and Fahey, 1962; Dyni, 1976; Smith et al., 2008). Consequently, authigenic mineral assemblages can sometimes dominate sediments and lake basin stratigraphy (Deocampo, 2015).

Magnesium (Mg^{2+}) silicates commonly form in saline alkaline lake environments under certain conditions, (1) the lake water is high in both alkalinity and aqueous silica (e.g. due to weathering volcaniclastics); (2) there are substantial time intervals in which there is low dilute inflow; (3) there is high evaporative concentration resulting in high salinity (Deocampo, 2015). An abundance of detrital dioctahedral smectite can result in interstratification of Mg-rich clays within the deposited material if these conditions are met (Hay and Kyser, 2001; Deocampo et al., 2009).

Specifically, authigenic trioctahedral smectite can be formed as a result, which occurs under conditions of low temperature diagenesis, hydrothermal alteration, and the wetting and drying of smectite (Jones, 1986; Hover and Ashley, 2003; Hover et al., 2005). Clay minerals found in mudstones need to be characterized as detrital or authigenic, and whether there is evidence for Mg-enrichment in the octahedral layer (Deocampo, 2015).

According to Moore and Reynolds (1997), layer silicates (kaolinite, illite, and smectite; in the case of terrestrial mudstones) have a tetrahedral and an octahedral sheet, where the tetrahedral sheet

has a dominant cation that is naturally Si^{4+} but can be substituted by Al^{3+} or Fe^{3+}, with 2 cations per 5 oxygen ions. The octahedral sheet consists of two planes of oxygen ions with cations in the center of the edge-linked octahedra constructed by the oxygen atoms. The cations in the octahedral sheet are usually Al^{3+}, Mg^{2+}, Fe^{2+} or Fe^{3+}. The tetrahedral and octahedral sheets are connected depending on their cation-to-anion ratio.

When distinguishing cation occupancy in the octahedral layer, there are two possibilities, dioctahedral and trioctahedral. Trioctahedral clays have a cation-to-anion ratio of 1:2, where divalent cations dominate the octahedral layer, such as Mg^{2+} and Fe^{2+}, and fill each octahedral site available to reach electric neutrality with the surrounding hydroxyls. Dioctahedral clays feature trivalent cations such as Al^{3+} and Fe^{3+} in the octahedral layer. In these minerals, there is a 1:3 cation-to-anion ratio. Only 2 of the 3 octahedral sites are filled due to the higher positive charge of the cations in this layer (Figure 1.1) (Moore and Reynolds, 1997).

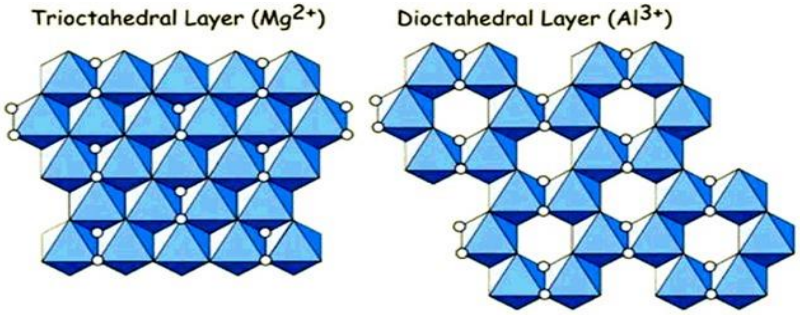

Figure 1.1 Octahedral layers of trioctahedral and dioctahedral cation occupancy*

Carroll and Bohacs (1999) lake classification, relating water and sediment supply with potential accommodation gives environmental parameters for possible lake settings in Figure 1.2 (A). Resultant clay endmembers according to specific octahedral cation occupancy can be found in the Octahedral Cation Index (OCI) ternary plot (Figure 1.2 (B)), where characteristic cations (M=montmorillonite,

*https://leorunfast.files.wordpress.com/2010/03/mica_o-sheet

Sa=saponite, Se=sepiolite, N=nontronite, K=kaolinite) determine overall phyllosilicate structure (Deocampo, 2015). Among the phyllosilicates that are trioctahedral and dioctahedral, smectite and illite can vary between both.

As stated before, dioctahedral smectite can diagenetically alter to trioctahedral smectite in terrestrial mudstones if the previously identified qualifications are met (Hay and Kyser, 2001; Deocampo, 2015). Specifically, dioctahedral smectite and kaolinite have been identified as the

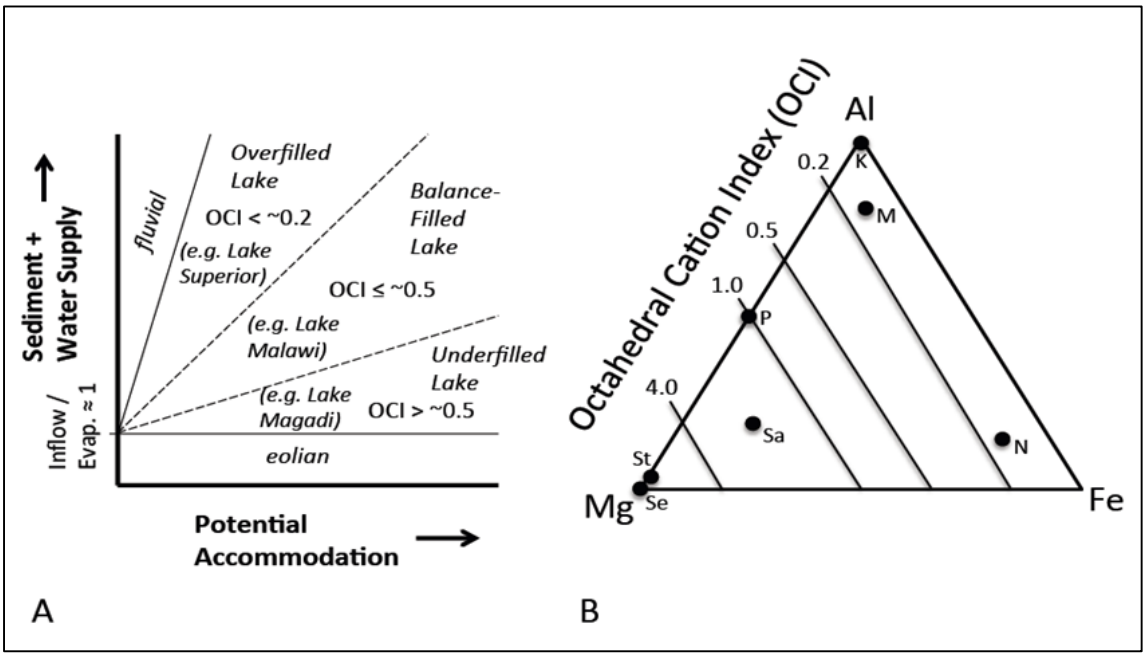

Figure 1.2 (A) Carroll and Bohacs lake classification (B) Octahedral Cation Index endmembers as displayed on a ternary plot (Deocampo, 2015)

detrital clays found in the drainage of Ngorongoro Volcanic Highland, located to the east of Olduvai Gorge and found in the main drainage from previous studies (Deocampo, 2004; Deocampo, et al., 2009; Deocampo, 2015).

1.3 Geologic Setting of Olduvai Gorge

Olduvai Gorge is located in Tanzania on the western shoulder of The East African Rift (EAR) in East Africa (Figure 1.3). Fault-related volcanoes and large depressions in which lakes have formed can be

found along the active rift (Hay, 1976). The Ngorongoro Volcanic Highland (NVH) is located at the eastern branch of the EAR system in Northern Tanzania (Figure 1.4) (Hay, 1970; Hay, 1976; Hay, 1990; Mollel, 2012). The NVH has

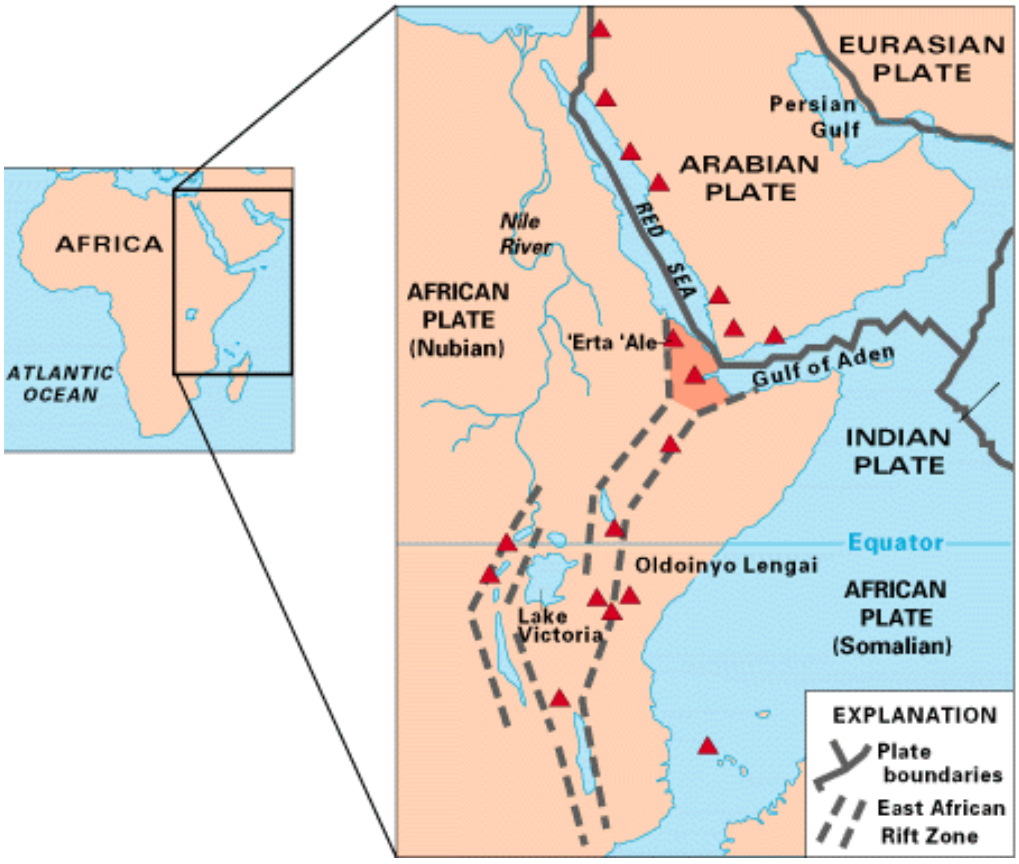

Figure 1.3 East African Rift System*

volcanoes that range in age from the late Miocene to recent, and features compositions ranging from basaltic to trachytic and carbonatites (Hay, 1976; Hay and Kyser, 2001; Deocampo, 2005; Ashley, 2007). These eruptive sources produced volcanic ashes that collected into surrounding lake basins around the area, preserving stratigraphic columns that can be now be studied as paleoenvironmental indicators (Hay, 1976).

Olduvai Gorge, which is located to the west of the NVH, on the western flank of the rift, was a

* http://pubs.usgs.gov/gip/dynamic/East_Africa.html

hydrologically-closed lake during the late Pliocene to early Pleistocene (Hay, 1976). Lake Olduvai's dilute inflow acquired lake water alkalinity due to dissolution of volcanic glass and lavas collected from the NVH and produced high initial SiO_2 and HCO_3 concentrations (Jones and Weir, 1983; Jones, 1986). Along with the volcaniclastics collecting into the lake bed, detrital dioctahedral smectite, which can be altered into Mg-rich smectite in closed-lake basins with high saline/alkaline conditions, was deposited into the paleolake (Hay, 1976).

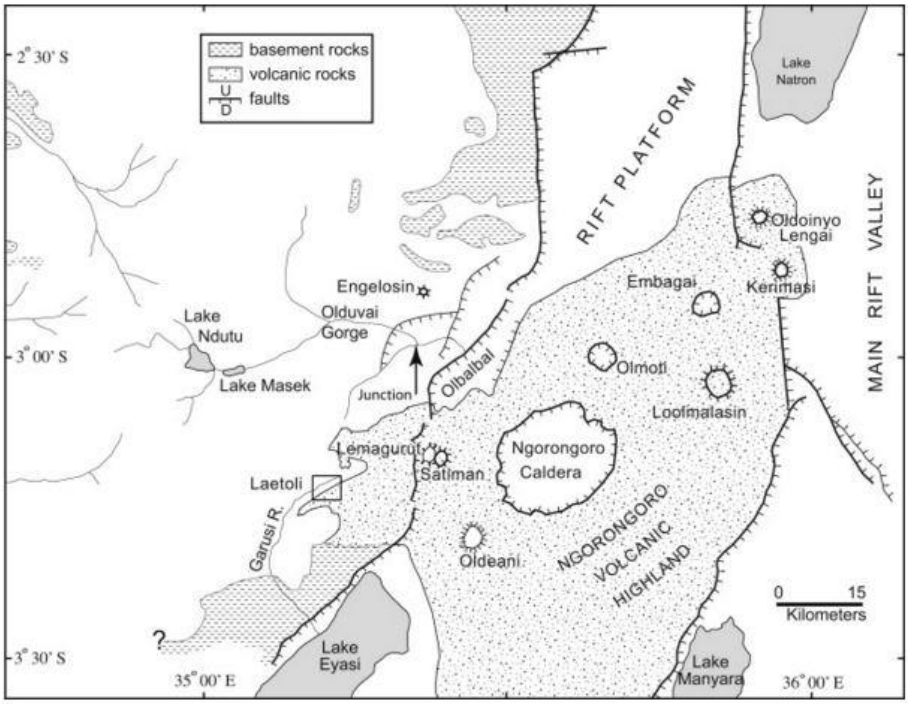

Figure 1.4 Ngorongoro Volcanic Highland and its proximity to Olduvai Gorge (Mees et al., 2007)

Locality 80, which is located in the central basin of Olduvai Gorge (Figure 1.5) is thought to have the most continuous lacustrine conditions preserved (Hay, 1976). It was estimated that as much as 70% of the basin fill was precipitated from lake water, featuring mainly silicate minerals (Hay and Kyser, 2001).

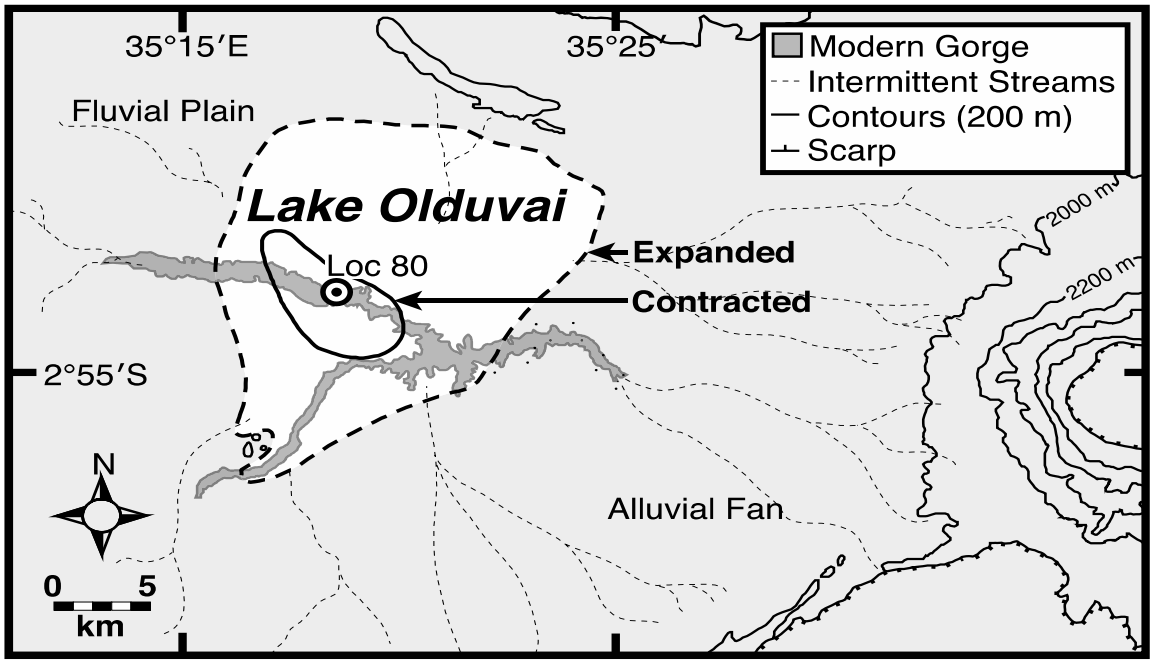

Figure 1.5 Olduvai Gorge, Tanzania, Locality 80 (Deocampo, 2015)

1.4 Statement of Purpose

In lake settings with low dilute inflow and small amount of detrital input, authigenic clays can form in highly alkaline/saline waters through Mg uptake in the diagenesis of dioctahedral smectite, forming authigenic trioctahedral smectite (Hay and Kyser, 2001). Fluctuations in the area's paleoclimate can be identified within the lacustrine stratigraphy through abundance of detrital dioctahedral smectite and kaolinite or authigenic trioctahedral smectite interstratified with illite, representing wetter climate conditions or arid climate conditions, respectively (Jones and Deocampo, 2003).

Understanding paleoclimate shifts helps us better understand the Earth's climatic patterns, and proxies for paleoclimatic shifts are needed to assist in identifying these trends. Because most proxies are biological, there is a large gap in paleoclimate identification in situations where these proxies are not available (Deocampo, 2015). This study will calculate geochemical ratios indicating authigenic trioctahedral smectite vs. detrital dioctahedral smectite found in a stratigraphic section taken from Locality 80 at Olduvai Gorge, Tanzania. Using previously collected data from the area (Berry, 2012), we will test how these indicators affect the bulk geochemistry, providing proxies for paleoclimate change.

2 ANALYTICAL METHODOLOGY

2.1 Sample Collection and Selection

Samples from Olduvai Gorge Locality 80 were provided by Dr. Gail Ashley of Rutgers University in New Jersey. A total of 167 samples were collected from the excavated outcrop (Figure 1.5). Once the stratigraphy was logged, the samples were collected by Drs. Gail Ashley, R.W. Renaut, and Richard Hay on July 9-11, 1999. The collection of these samples were a part of the Olduvai Landscape Paleoanthropology Project (OLAPP). Of these 167 bulk samples, 40 samples (Table 2.1) were chosen based on bulk X-ray fluorescence (XRF) analysis collected by Patricia Berry in 2012 at Georgia State University in Atlanta, GA. The samples were selected to represent a range of Al-rich and Mg-rich whole rock compositions. Figure 2.1 provides the XRF Al_2O_3/MgO ratios displayed according to depth at time of collection, points in red are the samples selected for this study's clay analysis (Berry, 2012). Samples chosen for this study are highlighted in red.

Additionally, ages assigned for the collection depths (Table 2.1) are adapted from published dates by Hay and Kyser (2001), as well as sedimentation rates; which are 1 meter per 5,900 years for Units 1 and 2, while Units 3 and 4 are represented by 8,300 years per 1 meter. Sedimentation rates contain the Olduvai subchron which is based on the paleomagnetic stratigraphy. The age scale is based on dates collected from tuff deposits found in the section, specifically: Tuff 1A; 1.92 Ma, Tuff 1B; 1.83 Ma, and Tuff 1F; 1.79 Ma. More details can be found in Berry (2012) and Hay and Kyser (2001).

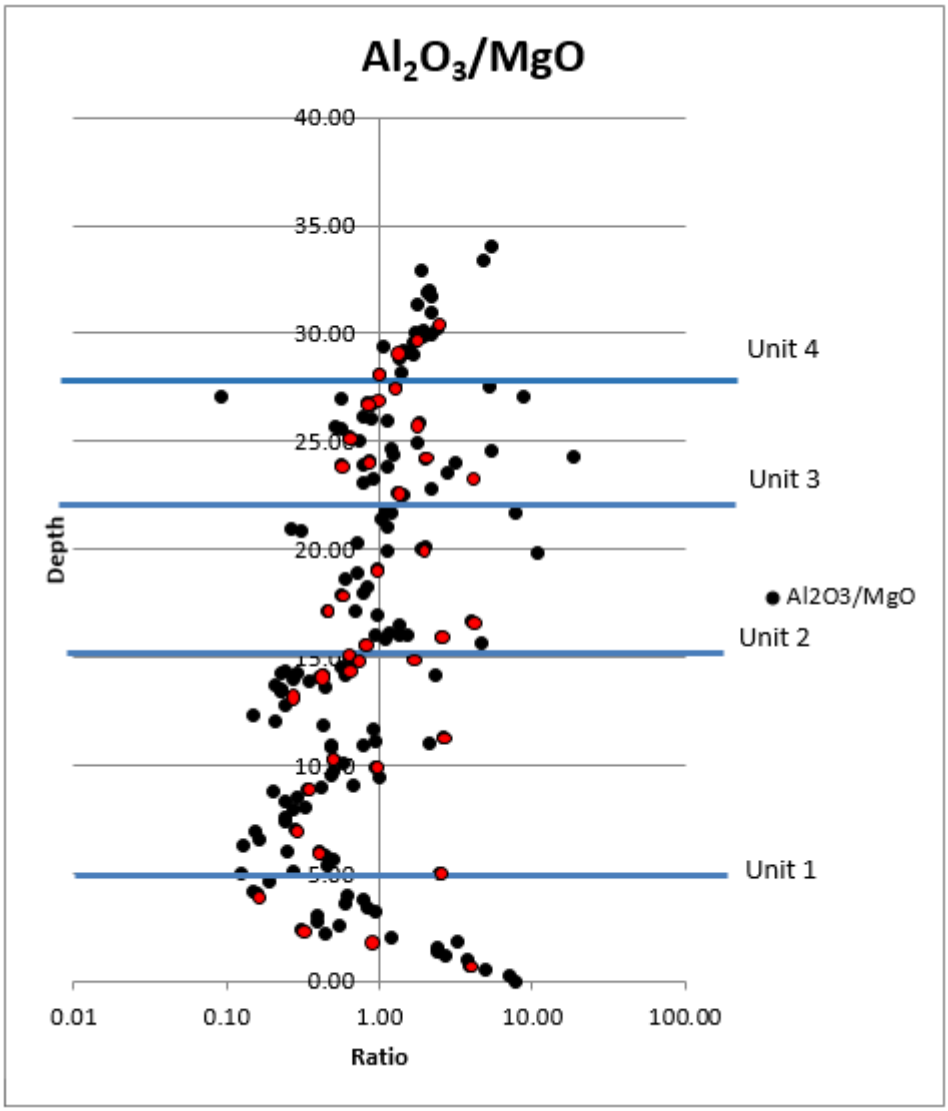

Figure 2.1 Al_2O_3/MgO XRF data according to depth, Olduvai Gorge (Berry, 2012). Samples selected for this study are shown in red.

Table 2.1 Samples selected for clay analysis according to variations in Al-enrichment and Mg-enrichment from bulk composition XRF results (Berry, 2012)

Locality 80: Sample Selection						
Depth from bottom (m)	**Sample ID**	**Age**	**Al_2O_3**	**Fe_2O_3**	**MgO**	**Al_2O_3 / MgO**
0.75	GA-L-4-99	1.9370	12.8	7.8	3.3	3.8
2.2	GA-L-11-99	1.9296	6.6	4.3	14.9	0.4
2.8	GA-L-14-99	1.9265	5.7	4.1	14.4	0.4
4.1	GA-L-21-99	1.9199	2.2	1.7	13.7	0.2
5	GA-L-25-99	1.9153	9.6	9.0	3.9	2.5
5.8	GA-L-29-99	1.9112	4.7	3.6	10.4	0.5
7	GA-L-35-99	1.9051	5.3	3.5	18.9	0.3
8.5	GA-L-112-99	1.8975	4.5	3.4	15.5	0.3
9.95	GA-L-120-99	1.8901	7.1	4.9	7.7	0.9
10.8	GA-L-123-99	1.8857	5.6	4.1	11.6	0.5
11.3	GA-L-128-99	1.8832	9.0	11.1	3.5	2.6
13.6	GA-L-78-99	1.8714	6.8	4.0	13.7	0.5
14.15	GA-L-84-99	1.8686	4.6	3.4	10.7	0.5
14.3	GA-L-87-99	1.8679	4.1	3.2	17.8	0.2
15	GA-L-91-99	1.8643	5.2	3.3	8.1	0.7
15.05	GA-L-92-99	1.8640	7.3	9.0	4.5	1.6
15.7	GA-L-95-99	1.8607	13.2	5.7	2.9	4.5
15.9	GA-L-97-99	1.8597	11.1	6.5	4.4	2.5
16	GA-L-99-99	1.8592	10.5	6.6	6.9	1.5
16.05	GA-L-101-99	1.8589	6.2	3.8	6.5	1.0
16.7	GA-L-104-99	1.8556	11.6	4.3	2.9	4.3
17.1	GA-L-135-99	1.8536	6.8	6.3	15.1	0.5
18	GA-L-139-99	1.8490	8.9	4.7	11.4	0.7
19.1	GA-L-143-99	1.8434	9.0	5.4	9.3	1.0
20.05	GA-L-147-99	1.8385	11.6	5.5	6.1	1.9
22.6	GA-L-65-99	1.8248	11.3	7.5	8.6	1.3
23.3	GA-L-62-99	1.8199	9.9	4.8	10.8	0.9
23.95	GA-L-58-99	1.8154	6.8	4.6	12.0	0.6
24.1	GA-L-56-99	1.8143	8.3	4.2	9.7	0.9
24.4	GA-L-53-99	1.8122	9.5	4.3	7.7	1.2
24.95	GA-L-50-99	1.8084	11.2	8.8	6.4	1.8
25.6	GA-L-47-99	1.8038	7.1	6.1	12.7	0.6
25.85	GA-L-45-99	1.8021	10.4	6.3	5.7	1.8
26.8	GA-L-38-99	1.7954	7.9	5.4	9.6	0.8
27	GA-L-37-99	1.7940	5.4	4.3	9.7	0.6
27.55	GA-L-157-99	1.7856	9.8	5.0	7.7	1.3
28.1	GA-L-156-99	1.7863	9.2	6.7	9.3	1.0
29	GA-L-160-99	1.7800	7.9	5.7	4.7	1.7
29.2	GA-L-163-99	1.7786	5.0	3.9	3.5	1.4
29.55	GA-L-165-99	1.7762	8.9	6.3	5.3	1.7

2.2 Initial Sample Preparation

To ensure proper extraction of the <1µm fraction, bulk samples were crushed using a ball pestle impact grinder (Figure 2.2) and put under ultrasound sonification for one minute with a Branson Model 450 Digital Sonifier (Figure 2.3). Afterwards, the samples were placed in centrifuge tubes and centrifuged for 1.5 hours at 8,500 rpm with an Accuspin 400 from Fischer Scientific. Consequently, the coarser fraction sunk to the bottom while the smaller clay fraction remained in the supernatant, the clay fractions were scraped and then accessible for further analysis (Figure 2.4).

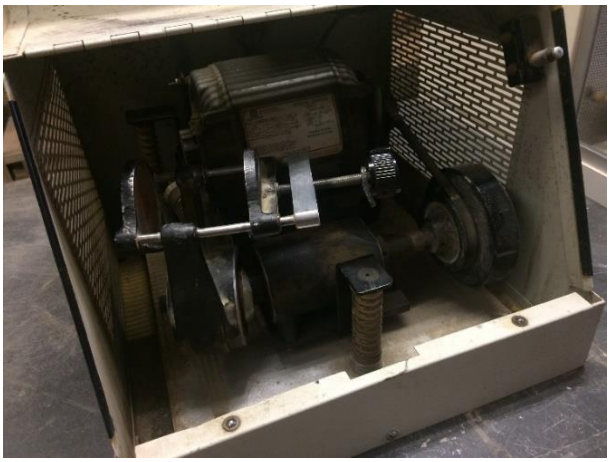

Figure 2.2 Ball and Pestle Impact Grinder

Figure 2.3 **Branson Digital Sonifier**

Figure 2.4 Sample selection for each analysis

2.3 Electron Microprobe Analysis (EMPA)

Electron Microprobe Analysis is an investigative tool used to determine the chemical composition of the minerals on a microscopic scale (Jansen and Slaughter, 1982). EMPA utilizes excited X-rays by a focused electron beam in which the X-ray spectrum gives out information regarding lines characteristic of the elements present in the material (Reed, 2005). According to Reed (2005) EMPA analysis is conducted using a tungsten filament electron source and enhanced by a positive anode plate from 3 to 30,000 electron volts. Electrons pass through the plate and are focused by a series of magnetic lenses and apertures. A beam of electrons produce a scan pattern that results in excitation within the sample. The electrons from the beam emitted by the EMPA interact with electrons bound in the inner electron shells of the elements. This causes movement of outer electrons into the innermost electron shells, as a result, a characteristic photon is emitted specific to the energy of the electron shell and element in question. Molecular details and chemical analysis are achieved by identifying the distinctive X-rays from the sample. A schematic of the instrument can be found in Figure 2.5 (Reed, 2005).

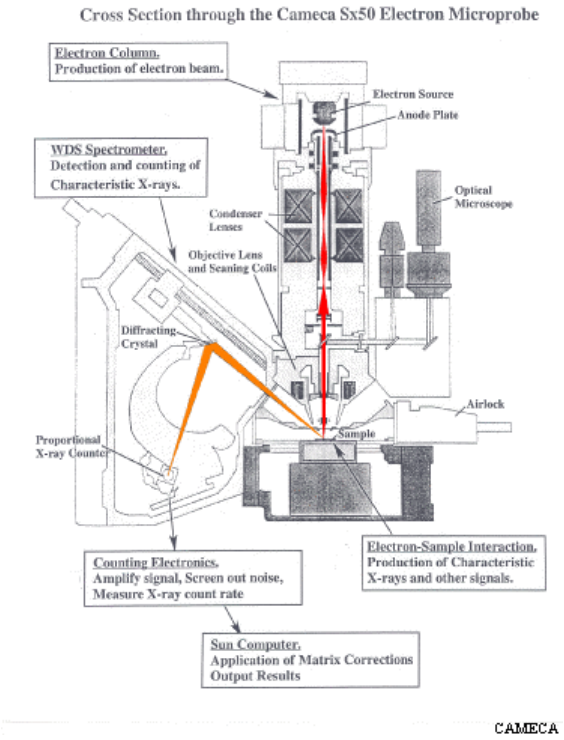

Figure 2.5 Electron Microprobe schematic*

2.4 EMPA Sample Preparation and Procedure

Electron Microprobe Analysis (EMPA) was conducted at Rutgers University in New Brunswick, New Jersey by Dr. Jeremy S. Delaney. To prep for the analysis, clay fraction samples were collected out of centrifuge tubes, place in crucibles, and heated to 600°C for 5 minutes each (Figure 2.6 and 2.7) using a Thermolyne 1300 Furnace. The purpose of heating was to drive off all crystal water and make the samples denser, reducing the likelihood of EMPA analysis of void space (Deocampo, 2004). The instrument used was a JEOL JXA-8200 Superprobe (Figure 2.8) located in the Department of Earth and Planetary Sciences. Once arrived, the samples were polished and mounted in epoxy resin and analyzed for element chemistry (Deocampo et al., 2009).

* http://pirlwww.lpl.arizona.edu/~domanik/UA_Microprobe/Intro.html

The microprobe was run with a 15 kV beam voltage and 5-10 nA beam current. The analysis spot on the sample was defocused to minimize the diffusive loss of mobile elements from the material. Additionally, Basic MZAF, a time-correction procedure used to correct intensity loss that can occur during analysis, was implemented (Dunn, 1989). A total of three analyses were run on each sample.

Figure 2.6 Thermolyne 6000 used for heating clay samples

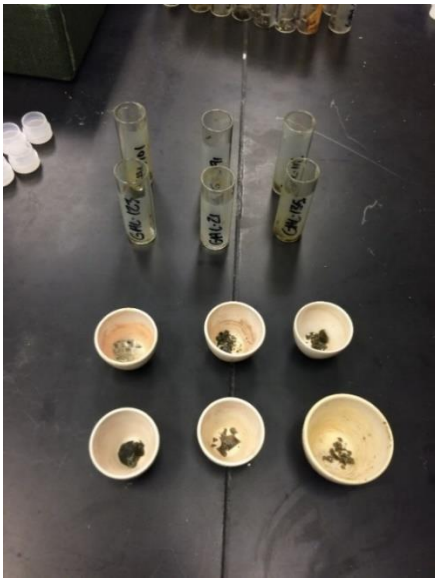

Figure 2.7 Six samples after heating for EMPA analysis

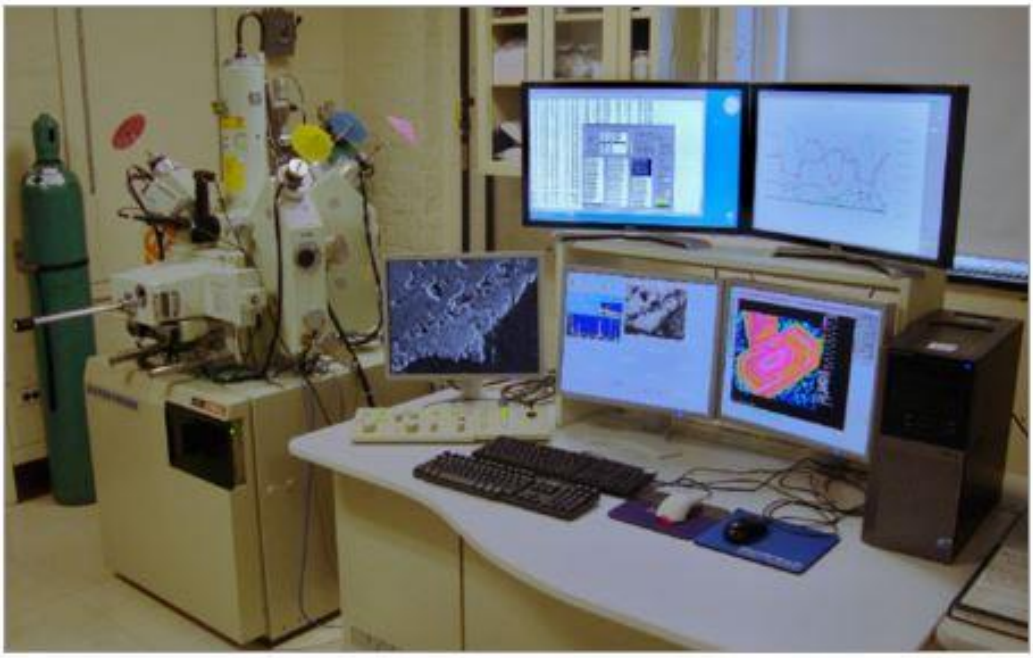

Figure 2.8 JEOL JXA-8200 Superprobe located at Rutgers University

2.5 X-Ray Diffraction (XRD)

X-Ray Diffraction (XRD) is an investigative technique that can be used for the identification of crystalline phases of minerals (Cullity, 1978; Moore and Reynolds, 1997). XRD implements Bragg's law (Figure 2.9). Mathematically, this theory can be explained by the equation $n\lambda = 2d\sin\theta$. Where λ = wavelength, d = d-spacing in between atoms, θ = angle in between incident angle and crystal surface, interacting as $n\lambda = 2d\sin\theta$. In other words, Bragg's law indicates there are certain angles (2-theta) at which positive interference of diffracted photons will produce a peak in X-ray diffractive intensities, their relationship to the wavelength is due to Bragg's law (Bragg, 1912).

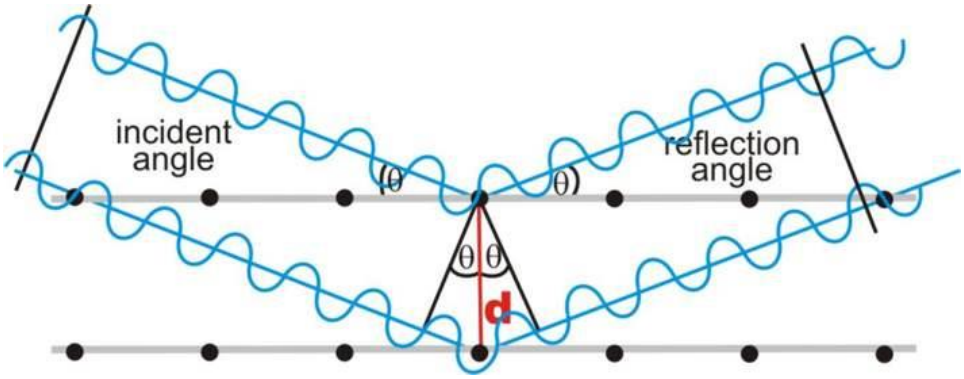

Figure 2.9 Bragg's Law*

XRD analysis involves a cathode that is heated and generates X-rays at 45 kilovolts (kV) of electrical potential and 40 milliamps (mA) of electrical current resulting in a power supply emitted through a Copper (Cu) X-ray tube. A wavelength (λ) with characteristic radiation is produced. The incident beam hits the surface of the sample and the diffracted beam at the angle measured produces distinctive peak patterns specific to the material being scanned by the instrument (Moore and Reynolds, 1997).

2.6 XRD Sample Preparation and Procedure

Oriented X-Ray Diffraction analyses were conducted on the 40 chosen samples after clay extraction with a PANalytical X'Pert Pro (Figure 2.12). After centrifuging each bulk sample, a small amount was skimmed off the top and placed on glass slides to prepare for clay analysis, two diffractograms were produced for each sample; air-dried, which was completed after the initial preparation of the clay slides and ethylene glycol solvated.

Figure 2.10 d060 scan preparation

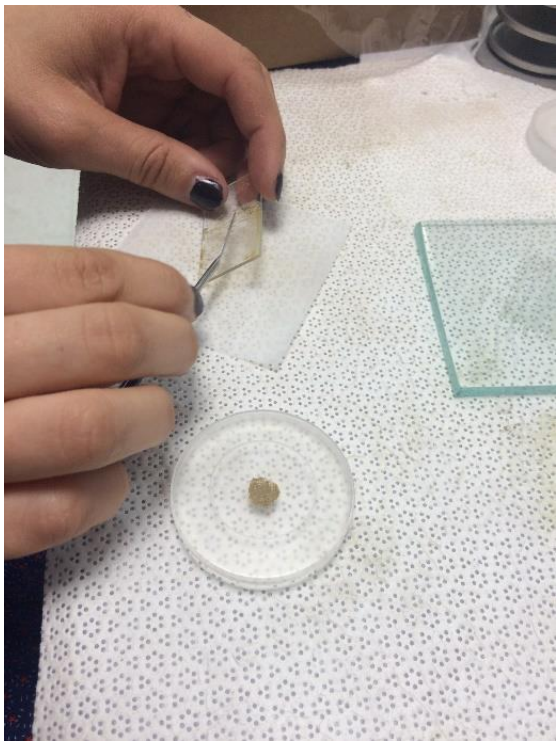

Figure 2.11 d60 scane preparation, zero-background slide

Figure 2.12 PANalytical X'Pert Pro

Ethylene glycol solvation, or glycolation, is achieved by placing the oriented clay slides in an environment in which the clay can be exposed to the vapor of the reagent which expands interlayer void space found within the material. Glycolation requires about 100-200mL of ethylene glycol placed in a glass dish on a platform where the slides can absorb the vapor. After at least 8 hours, the glycolated slides can be analyzed immediately and identified for characteristic swelling properties (Moore and Reynolds, 1997).

Afterwards, the slides air-dried for another 8 hours to ensure evaporation of the ethylene glycol, and then were scraped onto a zero-background slide for analysis of the 060 reflection (Figures 2.10 and 2.11). The randomly oriented pattern for the d060 scan allows for the identification of cation occupancy in the octahedral sheet, helping distinguish between trioctahedral and dioctahedral structure (Moore and Reynolds, 1997). All settings and times for all XRD analyses can be found in Table 2.2.

Table 2.2 XRD Scan Specifications

XRD Scan Specifications		
	Oriented Scans	060 Scans
Instrument	PANalytical X'Pert Pro XRD	
Voltage	45 kV	45 kV
Current	40 mA	40 mA
Soller Slits	0.04 rad.	0.04 rad.
Programmable Divergence Slit (PDS)	1/8˚	1/8˚
Fixed Anti- Scatter Slit	Fixed 1/16˚	Fixed 1/4˚
Fixed Incident Beam Mask	20mm	11.6mm
Programmable Anti-Scatter Slit (PASS)	Fixed 1/8	Fixed 1/8
Scan Axis	3.0˚-60.0˚	59.0˚-63.0˚
Step Size	0.0262˚	0.0131
Scan Time	30 mins	27:29 mins
PIXcel ID Active Length	3.347˚	3.347˚
Beta Filter	Ni	Ni
Sample Stage	PW3071/xx bracket	Reflection Spinner PW 3064/60

For 060 reflection data, the 2θ angles read were between 58.50-62.50˚ 2θ, with a d-spacing of ~1.480-1.525Å, indicating the cation octahedral occupancy of the authigenic material (Moore and Reynolds, 1997; Hay and Kyser, 2001). Figure 2.13(B) illustrates the possible variation of cation endmembers in the phyllosilicate octahedral layer (Deocampo, 2015), where the placement of the peak indicates Al/Fe-rich or Mg-rich occupancy.

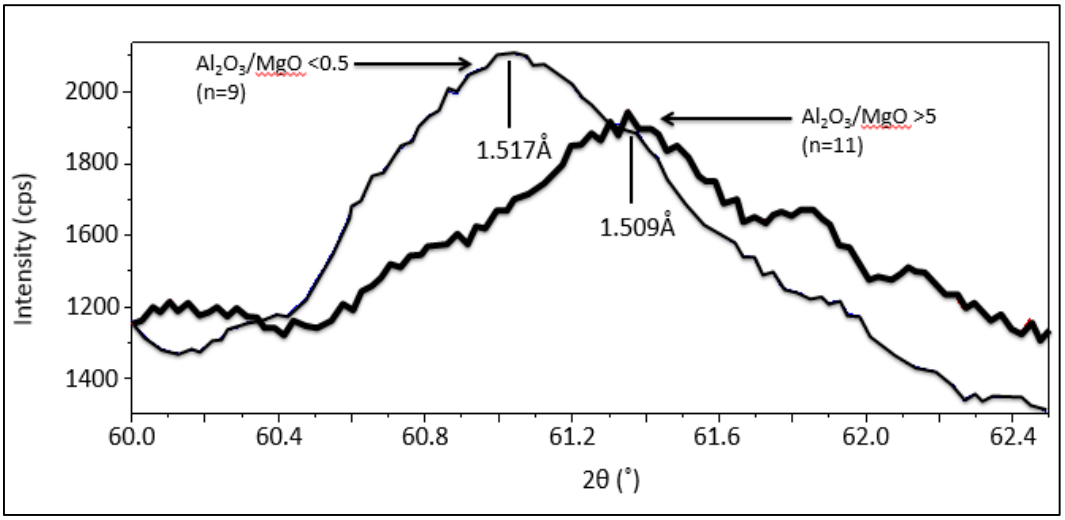

Figure 2.13 d060 variability and with OCI ratios. Figure from Deocampo, 2015.

2.7 Fourier Transform Infrared Spectroscopy (FTIR)

Fourier Transform Infrared Spectroscopy is an infrared method of absorption spectroscopy that is rapid, economical, and non-destructive (Russell and Fraser, 1994). When considering clay minerals, infrared (IR) radiation absorption depends on factors such as: atomic mass, as well as the length, strength, and force pertaining to the structures of the minerals in question. The overall symmetry of each atom in the unit cell is also a factor, concerning the vibrations internally given by 3n-6, where n is the number of particles within the unit. When collecting IR vibrations, there is an alteration in dipole moment which is subject to infrared adsorption, this is read by the IR instrument.

To obtain an accurate reading with infrared, the wavelength spectrum should be over the scope of 4000-250 cm^{-1}, ensuring a complete reading of all potential IR vibrations within the clay. Once excited by the FTIR beam, the wavelength is recorded within the given spectrum, providing details on the clay's geochemistry. FTIR uses the Michelson Interferometer (Figure 2.14), where light from a polychromatic IR source is emitted to a beam splitter (Shankland, 1964).

Ideally, some light is refracted towards the fixed mirror and some light is directed towards the moving mirror. Consequently, some light is directed back from the mirrors back to the splitter and some

of the original light goes through the sample slot, resulting in constructive interference within the wavelengths and reflects the adsorption bands detected by the IR source (Griffiths and DeHaseth, 2007).

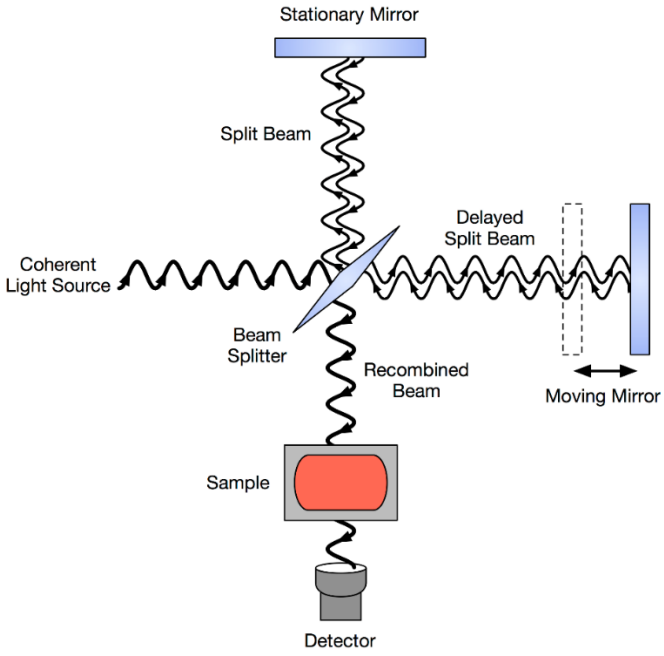

Figure 2.14 Michelson Interferometer used in FTIR*

2.8 FTIR Sample Preparation and Procedure

Fourier Transform Infrared Spectroscopy (FTIR) analysis was conducted by myself in London, England at the Natural History Museum under the supervision of Dr. Javier Cuadros. Sample preparation involved the technique described in Russell and Fraser (1994) where dispersion of each sample in Potassium Bromide (KBr) pressed discs was implemented using approximately 0.5 milligrams (mg) of sample and 199.50mg of KBr. Once combined, the KBr and sample were ground in a mortar and pestle (Figure 2.15) and pressed into pellets using a ring press (Figure 2.16) at 10 tons for 3 minutes each. Additionally, a blank with only KBr was pressed to calibrate the instrument before readings.

*http://www.analyticalspectroscopy.net/ap3-8.html

Figure 2.15 Sample and KBr after grinding with mortar and pestle

Figure 2.16 Ring press for pellets

The FTIR instrument used was a Perkin-Elmer Spectrum One (Figure 2.17). For each reading, the instrument was set at a resolution of 400 cm^{-1}, with a range between 4,000 cm^{-1} - 250 cm^{-1}, under scan type: sample. The amount of IR absorption was indicated along the y-axis of the scan, and the

wavenumbers per absorption were along the x-axis of the scan reading, each sample was scanned eight times and averaged to ensure a complete reading. Before each batch of samples, the blank was run to ensure calibration of the instrument. Each sample scan took approximately 20 seconds to complete. After running each sample, the peaks were examined for noticeable trends indicating characteristic hydroxyl-stretching and hydroxyl-bending bands (these peaks can be found in Table 3.2) indicative of the octahedral cation occupancy of each phyllosilicate (Figure 2.18) (Cuadros and Dudek, 2006; Deocampo et al., 2009).

Figure 2.17 Perkin-Elmer Spectrum One FTIR

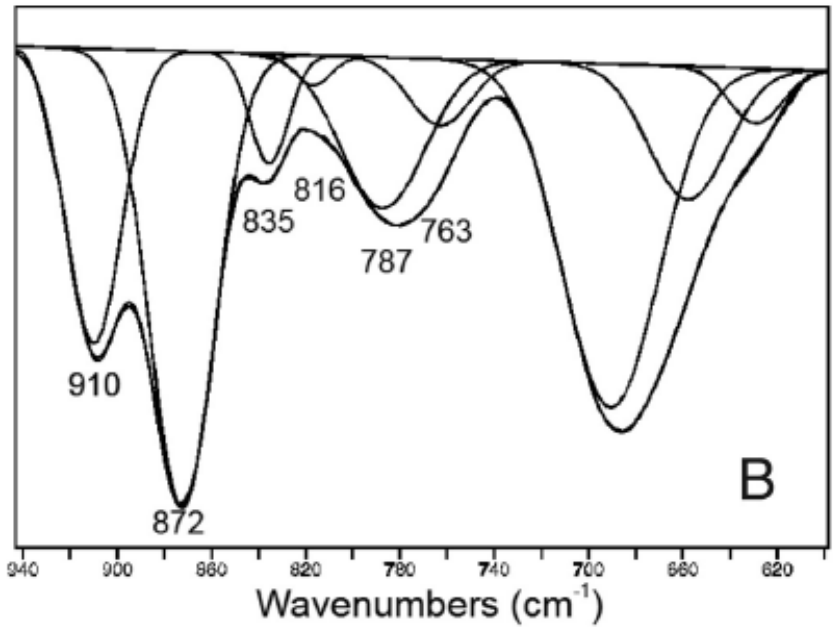

Figure 2.18 Bands characteristic to hydroxyl-bending cations (Deocampo et al., 2009)

2.9 Statistical Methodology

Linear regression plots were generated using datasets from all 3 clay analyses. Bulk composition XRF data (Al_2O_3 + Fe_2O_3)/MgO ratios were correlated with d060 results from clay XRD analysis, as well as (Al_2O_3 + Fe_2O_3)/MgO ratio weight percent data obtained from EMPA analysis. Correlation plots were generated for IR bands identified for Mg^{2+} and Fe^{3+} cation occupancy in the octahedral layer of clays with bulk XRF MgO/(Al_2O_3 + Fe_2O_3). For all regression plots, significant relationships between the variables was tested with R^2 and p-values (Freedman, 2009).

3 RESULTS AND DISCUSSION

3.1 EMPA Results

To obtain the geochemical composition, three EMPA scans were run on each of the samples. The average of the three normalized oxide values were taken to represent the geochemical data of the bulk submicron fraction. Ferric Iron was assumed to be fixed in the octahedral layer of the clays indicating octahedral occupancy at Fe^{3+}, therefore, the FeO weight percent was multiplied by 1.11 to ensure Fe_2O_3 as opposed to Ferrous Iron. The weight percent $(Al_2O_3 + Fe_2O_3)/MgO$ ratio values ranged from 0.2-4.6, 21 had ratios that were greater than 1, indicating higher $(Al_2O_3 + Fe_2O_3)$ content in the structure than MgO. Of these, GA-L-4, 25, and GA-L-99-160 were over 2.0 $(Al_2O_3 + Fe_2O_3)/MgO$. Of the 19 samples that were less than 1 $(Al_2O_3 + Fe_2O_3)/MgO$, 4 samples were less than a 0.5 ratio, indicating considerably more Mg^{2+} content. Some samples had large variability in the three EMPA scans, which was most likely attributed to sample heterogeneity during collection. CaO, found commonly in carbonate minerals, can overshadow the presence of smaller fraction cations found in the authigenic clays, causing less consistency in the scans (Reed, 2005).

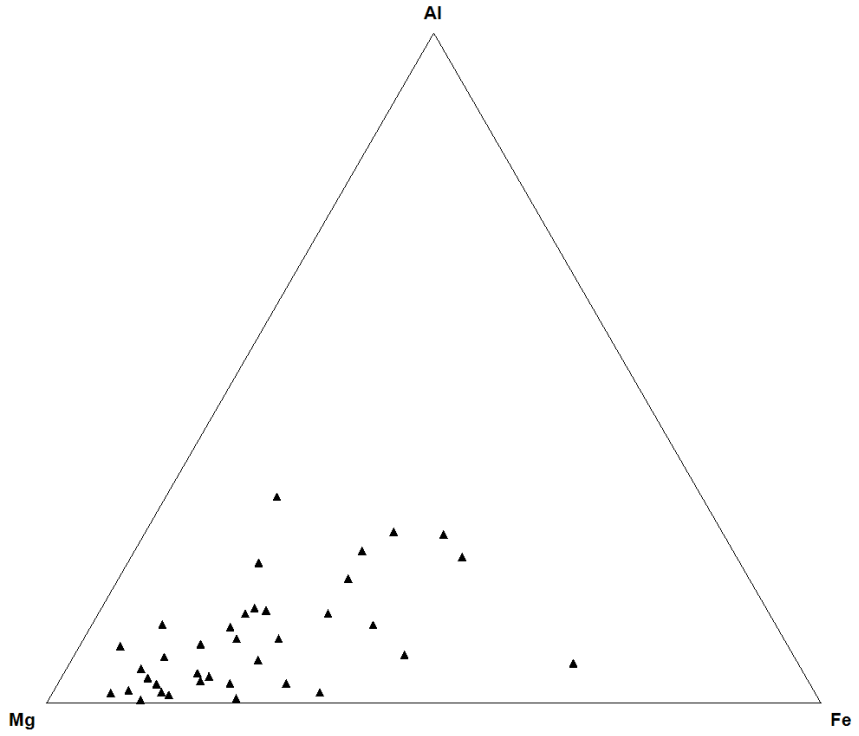

Figure 3.1 Olduvai Gorge, Locality 80 octahedral cation occupancy data

Figure 3.1 features EMPA weight percent data for Al-Fe-Mg octahedral occupancy for all 40 samples. Most samples had a majority of Mg-rich occupancy, with some sharing more Al and Fe cation abundance. GA-99-25, 95, 163, and 165 had CaO values over 6.0; likely representing carbonates in the sample that were not sufficiently removed. As a result, the weight percent data are skewed since a pure authigenic clay sample was not collected, carbonate removal was not performed prior to collection due to possibility of destruction of the fragile clay fraction, possible implementation of the use of Sodium Acetate in future work could help remove authigenic carbonates from the samples. Potassium (K^+) in these samples ranged from 2.0-8.0 weight percent, which coincides with the presence of illite in smectite samples and pure illite phases. All weight percent data and ratios can be found in Table 3.1.

Table 3.1 EMPA weight % data. Each reported value represents an average of 3 analyses.

	Elements in Weight Percent								
SAMPLE ID	**SiO_2**	**TiO_2**	**Al_2O_3**	**FeO**	**MgO**	**$(Al_2O_3 + Fe_2O_3)/MgO$**	**CaO**	**Na2O**	**K2O**
GA-L-99-165	53.9	2.4	6.9	8.0	10.6	1.5	9.1	2.2	6.6
GA-L-99-163	53.2	1.8	5.3	10.7	10.6	1.7	11.3	1.3	5.6
GA-L-99-160	59.1	2.2	8.3	10.8	10.4	2.0	1.3	1.8	6.4
GA-L-99-156	59.2	1.2	5.6	1.1	19.7	1.7	0.3	3.4	5.4
GA-L-99-154	58.1	1.7	3.3	15.3	11.6	0.6	2.5	2.9	4.8
GA-L-99-147	61.5	0.9	8.1	6.6	15.0	1.0	0.2	2.6	5.4
GA-L-99-143	57.6	2.0	8.4	7.4	16.0	1.0	0.4	2.8	5.6
GA-L-99-139	60.4	0.8	5.8	6.7	18.5	0.7	0.3	3.4	4.3
GA-L-99-135	57.0	0.9	5.4	5.2	23.3	0.5	0.6	3.1	4.2
GA-L-99-128	58.1	1.1	5.2	8.0	19.1	0.7	0.4	3.3	4.9
GA-L-99-123	61.9	1.0	5.0	2.2	19.6	0.5	0.5	4.0	3.8
GA-L-99-120	59.4	1.4	6.5	7.4	15.0	1.1	0.3	4.8	5.0
GA-L-99-112	60.5	0.7	4.6	4.2	23.1	0.4	1.2	2.8	3.0
GA-L-99-104	58.8	0.8	3.4	15.0	14.2	1.4	1.0	4.0	3.3
GA-L-99-101	60.6	1.2	6.7	6.9	15.8	0.9	0.5	2.9	5.1
GA-L-99-99	60.0	2.0	7.5	9.3	13.7	1.3	0.8	1.8	5.8
GA-L-99-97	60.0	1.5	9.0	7.4	12.2	1.4	2.7	1.2	6.8
GA-L-99-95	60.1	1.0	10.2	6.9	10.0	1.8	7.7	1.2	8.0
GA-L-99-92	54.3	2.0	6.8	10.3	12.9	1.4	1.8	1.4	5.1
GA-L-99-91	59.6	1.2	4.8	6.1	18.9	0.6	0.4	1.5	3.9
GA-L-99-87	62.4	0.7	3.0	3.2	23.2	0.3	1.3	3.8	2.9
GA-L-99-84	59.4	1.0	4.0	4.3	21.8	0.4	0.8	4.0	3.9
GA-L-99-78	56.5	1.0	4.9	6.9	22.8	0.6	0.7	5.0	4.0
GA-L-99-65	58.3	1.4	7.9	8.1	14.5	1.2	0.5	3.2	6.3
GA-L-99-62	58.1	1.1	5.9	7.0	20.0	0.7	0.4	3.5	4.6
GA-L-99-58	55.1	3.2	7.7	8.8	16.0	1.1	1.9	2.6	5.2
GA-L-99-56	58.6	1.5	5.4	5.0	20.5	0.6	0.5	5.3	2.8
GA-L-99-53	57.3	0.5	2.6	7.3	22.6	0.5	0.4	4.7	3.9
GA-L-99-50	58.1	0.6	4.3	14.3	14.7	1.4	0.3	5.2	2.6
GA-L-99-47	57.9	1.4	6.0	8.2	18.9	0.8	0.7	2.4	4.4
GA-L-99-45	56.3	1.3	6.6	8.0	15.0	1.4	1.1	2.8	5.5
GA-L-99-38	58.1	2.8	6.3	9.1	14.6	1.1	1.6	2.0	5.7
GA-L-99-37	60.1	0.4	7.1	5.9	15.1	1.1	5.8	1.0	2.9
GA-L-99-35	57.4	1.0	6.1	5.3	21.4	0.5	1.8	3.2	4.2
GA-L-99-29	54.2	1.1	6.4	6.5	22.0	0.6	2.7	2.5	4.9
GA-L-99-25	43.5	0.5	11.2	19.6	7.5	4.6	8.3	2.8	5.3
GA-L-99-21	56.1	0.4	2.9	2.7	28.4	0.2	5.4	2.2	2.0
GA-L-99-14	59.8	0.5	4.6	4.1	24.4	0.4	1.0	3.6	2.0
GA-L-99-11	57.9	1.3	8.2	12.2	11.1	1.2	1.7	1.4	6.5
GA-L-99-4	57.8	1.8	9.5	14.3	6.8	3.8	1.4	1.7	6.2

3.2 FTIR Results

Each sample underwent infrared analysis to determine the hydroxyl bending and stretching of the hydroxyl (OH^-) bonds with the cations found in the octahedral layer of the clays. The wavelength peaks were distinguishable by familiar characteristics found with most phyllosilicates. Although, some readings were less developed as opposed to completely matured clays due to lack of full formation during the *in situ* incorporation of Mg^{2+} during higher salinities.

Clay variations were identified using Wilson (1992). Here, the characteristics of the SiO peaks were identified to help determine the presence of interstratified illite-smectite and indicators of dioctahedral or trioctahedral cation placement. SiO peaks are indicative of interstratified illite-smectite at 1031 cm^{-1} with a small peak at 1090 cm^{-1}. Trioctahedral smectites have a lower wavenumber and range from 1010 cm^{-1}, 1002 cm^{-1}, and 1013 cm^{-1} (hectorite, saponite, and stevensite, respectively). Dioctahedral smectites have SiO wavenumber peaks at 1029-1038 cm^{-1} and 1004 cm^{-1}, which are indicative of montmorillonite and nontronite, respectively.

Illites, which vary between muscovite-like (greater Al and Fe content) and phengite-like (greater Mg content), have SiO peaks at 1026 cm^{-1} and 1024 cm^{-1}, respectively. Table 3.2 displays the SiO bands for each of the FTIR readings in each sample, although there were no pure illites identified, there was kaolinite and illite observed in some samples. These peaks can be indicative but can also vary due to cation pull on the hydroxyl bands between the tetrahedral and octahedral layers, structural imperfections, and diagenetic processes.

When considering cation placement, there are specific peaks that can be found due to OH deformation bands and their vibration specific to the pull of the particular cation in place. These peaks can be found in Table 3.2. OH bending bands, which determine the cation occupancy and dioctahedral or trioctahedral abundance, range from 940-550 cm^{-1} and are also listed in Table 3.2. These reference

bands were adapted from Russel and Fraser (1994); Kloprogge and Frost (2001); and Deocampo et al. (2009).

A total of ~52% samples had distinguishable Fe_2 peaks, indicating dioctahedral occupancy. While ~85% of the samples had peaks indicating trioctahedral Mg^{2+} occupancy. All but 2 samples (GA-L-99-78 and GA-L-99-160) had peaks indicative of Mg_2Fe occupancy, while all samples had peaks for FeMg occupancy. The only samples with peaks at Al_2 were GA-L-99-92 and GA-L-99-112. When considering SiO peaks, they varied from 1010-1038 cm^{-1}. GA-L-99-53 had the peak at 1038 cm^{-1}, suggesting a more dioctahedral influence.

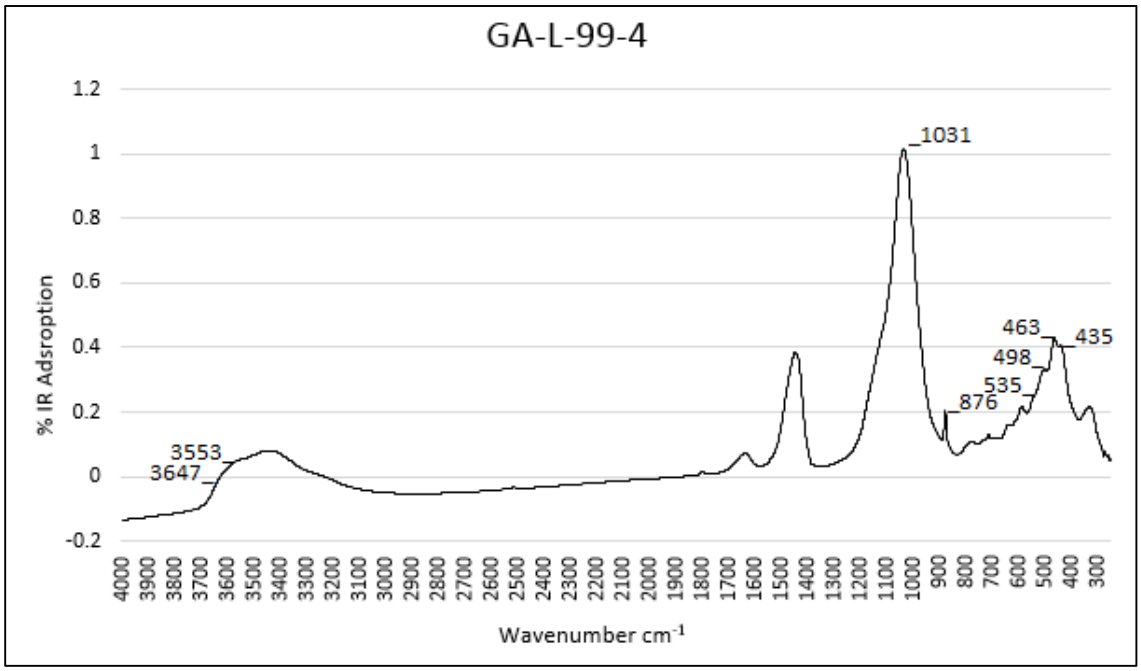

Figure 3.2 GA-L-99-4 FTIR Scan

Some samples, as expected, had peaks indicating carbonate and feldspar, these samples were most likely contaminated due to improper removal of all material that was not predominately the submicron fraction. These minerals were especially noticeable in samples: GA-L-99-25, GA-L-99-37, and GA-L-99-157. GA-L-99-4's FTIR scan can be found in Figure 3.2. The structure of illite was identified in the double hydroxyl stretching peaks at 535 cm^{-1}, 498 cm^{-1}, 463 cm^{-1}, and 435 cm^{-1}. The OH-bending band at

3674 cm^{-1} is also indicative of illite, indicating more dioctahedral cation structure i.e. Al^{3+} and Fe^{3+}, as opposed to Mg^{2+}.

Sample GA-L-99-128's infrared spectra is found in Figure 3.3. GA-L-99-128 is particularly a clear example of a trioctahedral, Mg-rich smectite the characteristic OH-bending band at 3675 cm^{-1} is characteristic to saponite and stevensite, both are trioctahedral smectites. Furthermore, characteristic of trioctahedral smectites, the OH-stretching band at 656 cm^{-1} indicated Mg^{2+} octahedral occupancy, and the one strong band at 466 cm^{-1}, with smaller bands on each side at 532 cm^{-1} and 442 cm^{-1} fall into the smectite category. The SiO band is distinctive to stevensite at 1014 cm^{-1}, confirming very low Al^{3+} content coupled with high Mg^{2+} content and occupancy, which is very similar to the other IR readings in this study when considering the overall broader peaks as opposed to very distinguishable peaks indicative of full crystallization, these broader peaks are due to the lack of completely phyllosilicate development *in situ* during diagenesis.

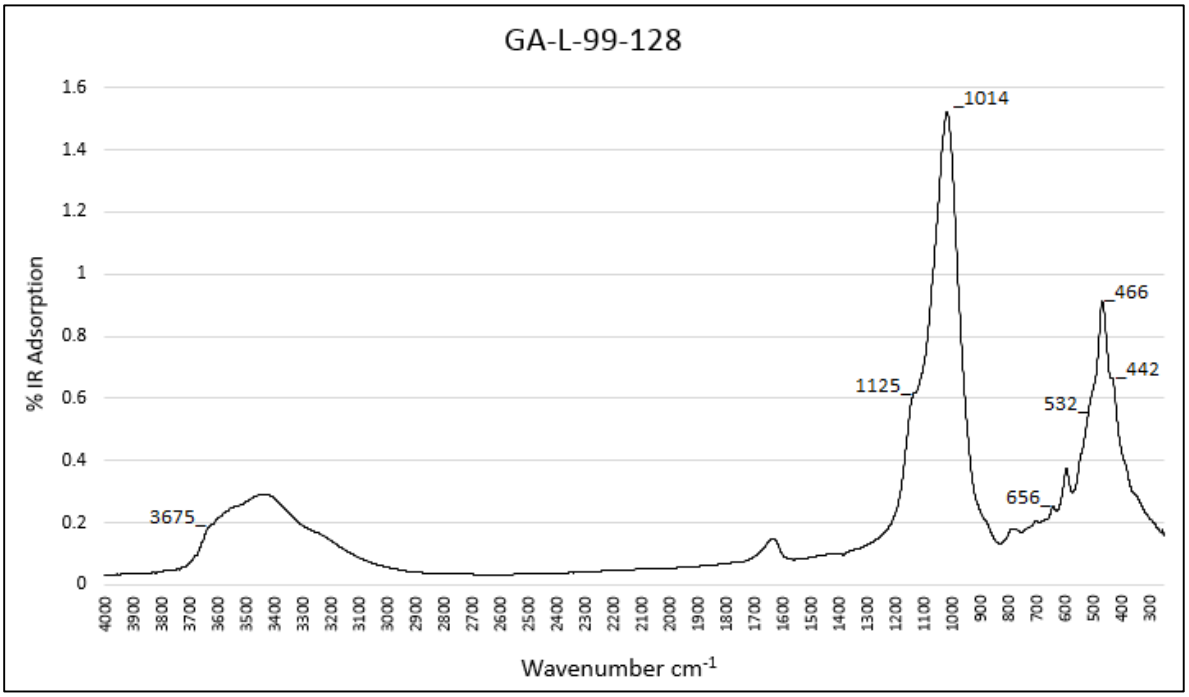

Figure 3.3 GA-L-99-128 FTIR Scan

Table 3.2 FTIR hydroxyl-stretching values

		Sample ID						
Cation(s)	Peak (cm^{-1})	GA-L-99-4	GA-L-99-11	GAL-99-21	GAL-99-25	GA-L-99-29	GA-L-99-35	GA-L-99-37
Al_2	911							
AlFe	874	876		874				867
AlMg	837	835						842
Fe_2	816	816	816	816		817	807	818
FeMg	780	776	785	783	776	781	780	769
Mg_2Al	737		731	727	724		727	
Mg_2Fe	705	711	690	708	702	711	689	713
Mg_3	657		650	654		653	651	637
SiO	Variable	1031	1014	1010	1021	1012	1012	1012

		Sample ID						
Cation(s)	Peak (cm^{-1})	GA-L-99-38	GA-L-99-45	GAL-99-47	GAL-99-50	GA-L-99-53	GA-L-99-56	GA-L-99-58
Al_2	911	910						
AlFe	874	868	873	875	869	869	873	875
AlMg	837	834						
Fe_2	816	810	810	815	815			810
FeMg	780	769	769	780	769	771	771	769
Mg_2Al	737					725	733	
Mg_2Fe	705	711	711	697	695	712	690	706
Mg_3	657	656	656	648	647	652	648	647
SiO	Variable	1012	1021	1014	1019	1038	1010	1012

Table 3.2 continued

		Sample ID						
Cation(s)	Peak (cm^{-1})	GA-L-99-62	GA-L-99-65	GAL-99-78	GAL-99-84	GA-L-99-87	GA-L-99-91	GA-L-99-92
Al_2	911							897
AlFe	874		881	876	873		875	872
AlMg	837				827	831		
Fe_2	816	820				811		
FeMg	780	778	781	785	783	785	783	788
Mg_2Al	737		745		735			726
Mg_2Fe	705	798	695		711	697	699	700
Mg_3	657	656	658	659	648	654	658	647
SiO	Variable	1010	1012	1010	1010	1016	1010	1017

		Sample ID						
Cation(s)	Peak (cm^{-1})	GA-L-99-95	GA-L-99-97	GAL-99-99	GAL-99-101	GA-L-99-104	GA-L-99-112	GA-L-99-120
Al_2	911						900	
AlFe	874	873	873	870	883	873	875	873
AlMg	837			837		827		834
Fe_2	816	816	810		807	814		811
FeMg	780	778	775	789	780	787	783	782
Mg_2Al	737	730	739					
Mg_2Fe	705	695	699	689	695	700	699	695
Mg_3	657	660	649	648	662	654	658	646
SiO	Variable	1014	1014	1022	1012	1012	1010	1012

Table 3.2 continued

		Sample ID						
Cation(s)	Peak (cm^{-1})	GA-L-99-123	GA-L-99-128	GAL-99-135	GAL-99-139	GA-L-99-143	GA-L-99-147	GA-L-99-156
Al_2	911							
AlFe	874	873	879	864	866		873	876
AlMg	837							
Fe_2	816	816		820	816	820	821	
FeMg	780	787	793	783				
Mg_2Al	737		737					
Mg_2Fe	705	697	709	693	690	690		712
Mg_3	657	654	656	662	648	658	659	
SiO	Variable	1012	1014	135	1010	1010	1012	1010

		Sample ID			
Cation(s)	Peak (cm^{-1})	GA-L-99-157	GA-L-99-160	GAL-99-163	GAL-99-165
Al_2	911				
AlFe	874	873	872	864	866
AlMg	837				
Fe_2	816	816	815	820	816
FeMg	780	787	779	783	
Mg_2Al	737		735		
Mg_2Fe	705	697			
Mg_3	657	654	653	662	658
SiO	Variable	1012	1014	1035	1010

3.3 XRD Results

3.3.1 XRD Oriented Clay Analysis

Clay analysis was conducted on each sample to identify dominant clay phases. Samples varied from illite to smectite, with the majority of samples showing instratified illite-smectite. Pure

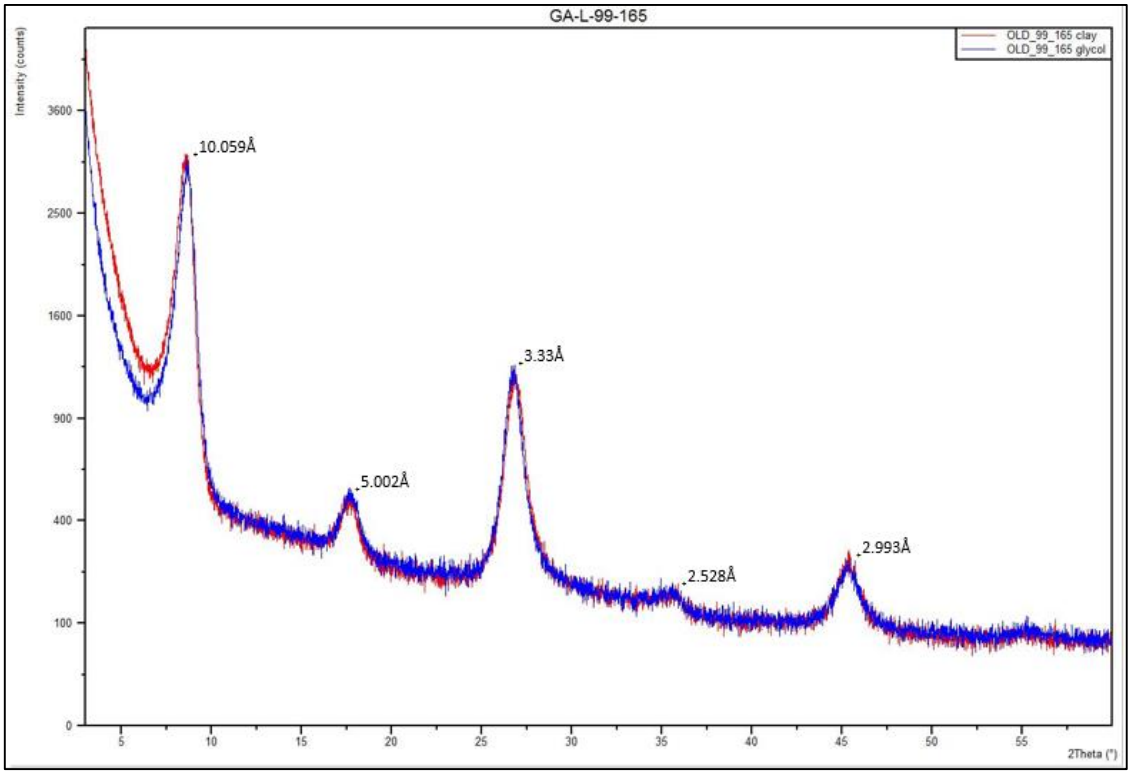

Figure 3.4 Glycolated and air-dried XRD data for GA-L-99-165

phases of smectite and illite were found in samples GA-L-99-4, 45, 156, 160, 163, and 165. Characteristic of illite, the air-dried and glycolated XRD diffractograms for these samples have peaks at or around 10.00Å as the 001 peak and 5.00Å at 002, for these particular samples there is no evidence of a smectite peak (Moore and Reynolds, 1997). All pure illite readings show the same trends in air-dried and glycolated readings.

GA-L-99-165 (Figure 3.4) was found at the top of the stratigraphic section, near the ~1.7 mya mark in the stratigraphy (Berry, 2012; Hay and Kyser, 2001). Other samples along the section gave evidence for smectite-illite interstratification, with dominance in more smectite. Figures 3.5, 3.6, and 3.7 show three examples: GA-L-99-87, GA-L-99-14, and GA-L-99-112; of which all have smectite peaks with smaller, less distinguished, discrete illite peaks. When glycolated, smectite has a d-spacing of around 17.00Å due to the swelling between siloxane surfaces (Moore and Reynolds, 1997).

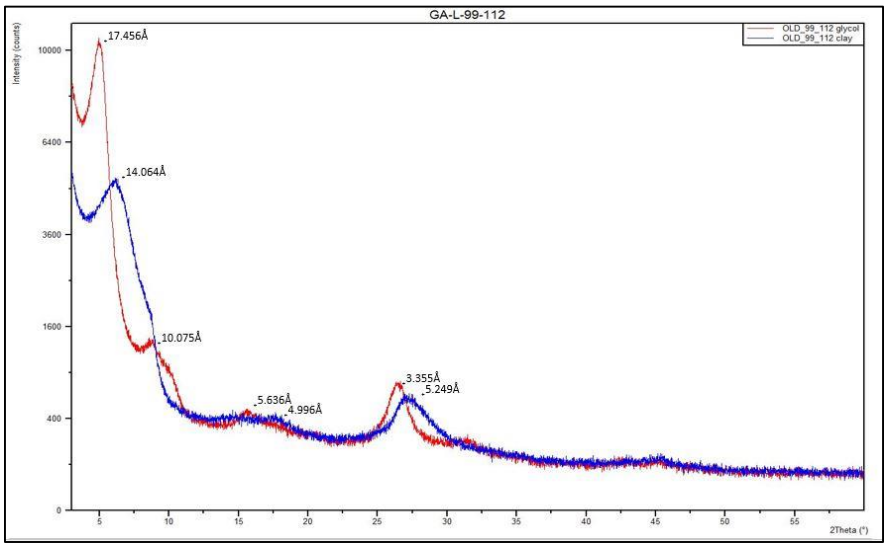

Figure 3.5 Glycolated and air-dri-ed XRD data for GA-L-99-112

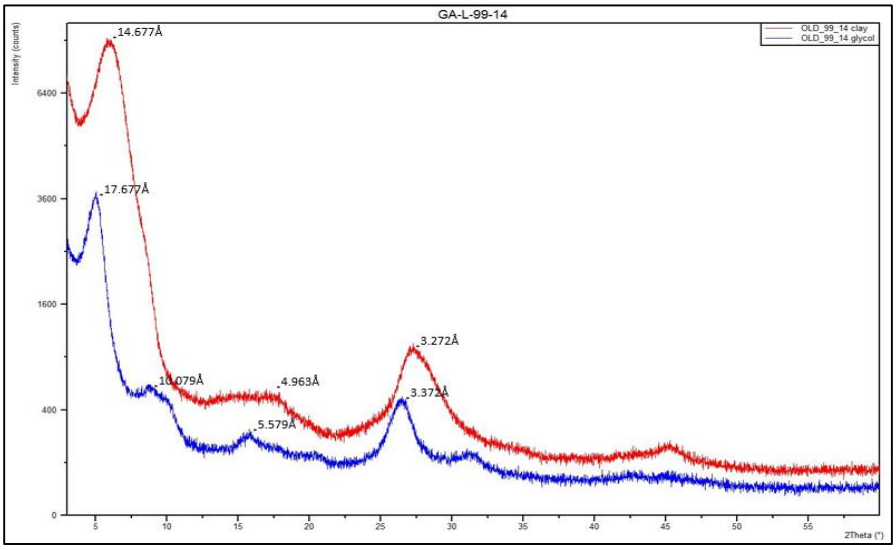

Figure 3.6 Glycolated and air-dried XRD data for GA-L-99-14

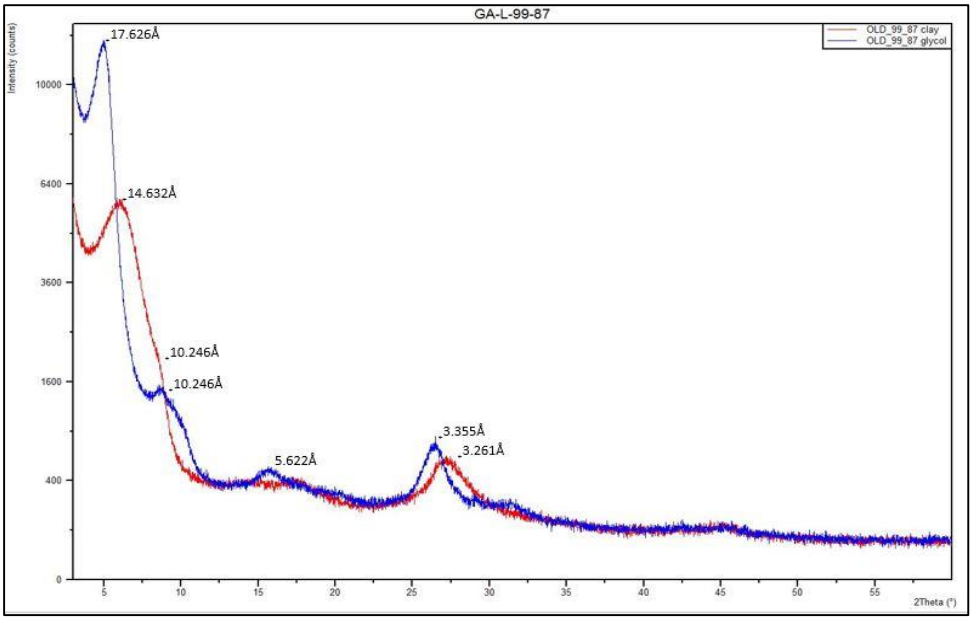

Figure 3.7 Glycolated and air-dried XRD data for GA-L-99-87

The variation in octahedral composition (dioctahedral or trioctahedral) is distinguished by the d060 readings, which can be found in section 3.3.2. Most samples, except for the pure illite phases mentioned previously in the section, show variations in smectite with discrete illite throughout. GA-L-99-25 and GA-L-99-92 both showed results of pure smectite with some kaolinite and no illite present. In addition, GA-L-25, 92, 95, 97, and 128 all had peaks indicating the presence of detrital kaolinite at a d-spacing of ~7.16Å (Moore and Reynolds, 1997).

In addition to the clay readings, samples GA-L-99-25, 38, 92, 99, and 163 showed peaks for carbonates at ~3.86Å, indicating sample heterogeneity during extraction. Feldspar peaks were found in samples GA-L-99-25 and GA-L-99-128 at ~4.21Å, additionally showing evidence for sample heterogeneity (Moore and Reynolds, 1997). These samples had very little clay fraction available during extraction, attributing to difficulty in obtaining the <1µm fraction.

3.3.2 d060 XRD Analysis

The clays found in each sample from the air-dried and glycolated XRD analyses indicated variations between dioctahedral and trioctahedral phyllosilicates (Moore and Reynolds, 1997). Samples varied between Mg-rich and Al + Fe rich according to the d-spacing results from the d060 peaks (Deocampo, 2004).

Table 3.3 indicates the d-spacing readings and 2θ for each sample. d060 peak readings for the samples ranged between d-spacing: 1.509-1.523Å and 60.71-61.50° 2θ. Samples ranging from 60.89-61.25° were identified as trioctahedral (Saponite-Mg-rich Montmorillonite), while samples ranging from 60.90-61.60° have a dioctahedral component, indicating Fe-rich Montmorillonite-Nontronite (Deocampo et al., 2009). Most samples are within these two ranges, suggesting a trioctahedral and dioctahedral intermediate phase, perhaps attributed to the presence of Mg^{2+} and Fe^{3+} in most samples. Because both ranges are very similar, the distinction between Mg-rich and Fe + Al-rich 2θ angle was separated at 61.25°, to distinguish between a more trioctahedral or dioctahedral influence, since both are present in most samples. $Phase_{060}$ column in Table 3.3 indicates clays with a 2θ angle less than 61.25° as Mg-rich, while samples with angles greater than 61.25° are indicated as Fe + Al-rich. Most samples proved to be Mg-rich. Some clays with weaker Mg-rich peaks, indicating some dioctahedral cation influence; were GA-L-25, 35, 38, 65, 91, 99, and 147-99. Samples GA-4, 45, 156, 160, 163, and 165-99 proved to have dominantly divalent cations within the octahedral layer. Al + Fe-rich octahedral occupancy showed in illites previously identified from the air-dried and glycolated XRD analysis, while interstratified illite found with smectite proved to be more Mg-rich.

Of these samples, GA-L-99-4, 25, 38, 91, and 99 were given a range of d060 Å readings since the peaks were relatively indistinguishable. They were also taken out of further correlations in this study since a specific peak could not be determined (Table 3.3).

Table 3.3 Sample d060 and 2θ results

Sample ID	d-spacing	060 °2θ	$Phase_{060}$
GA-L-99-4	1.509-1.511	61.49	Al+Fe-rich*
GA-L-99-11	1.523	60.75	Mg-rich
GA-L-99-14	1.524	60.71	Mg-rich
GA-L-99-21	1.522	60.84	Mg-rich
GA-L-99-25	1.520-1.523	60.94	Fe+Al-rich*
GA-L-99-29	1.521	60.83	Mg-rich
GA-L-99-35	1.518	61.00	Fe+Al-rich
GA-L-99-37	1.522	60.83	Mg-rich
GA-L-99-38	1.508-1.512	61.44	Fe+Al-rich*
GA-L-99-45	1.522	60.81	Mg-rich
GA-L-99-47	1.521	61.08	Mg-rich
GA-L-99-50	1.519	60.86	Mg-rich
GA-L-99-53	1.521	60.86	Mg-rich
GA-L-99-56	1.523	60.78	Mg-rich
GA-L-99-58	1.523	60.80	Mg-rich
GA-L-99-62	1.520	60.90	Mg-rich
GA-L-99-65	1.513	61.20	Fe+Al-rich
GA-L-99-78	1.523	60.72	Mg-rich
GA-L-99-84	1.517	61.05	Mg-rich
GA-L-99-87	1.518	60.99	Mg-rich
GA-L-99-91	1.512-1.520	61.02	Fe+Al-rich*
GA-L-99-92	1.518	60.99	Mg-rich
GA-L-99-95	1.514	61.07	Mg-rich
GA-L-99-97	1.518	60.97	Mg-rich
GA-L-99-99	1.512-1.509	61.38	Fe+Al-rich*
GA-L-99-101	1.517	61.05	Mg-rich
GA-L-99-104	1.518	60.95	Mg-rich
GA-L-99-112	1.520	60.91	Mg-rich
GA-L-99-120	1.516	61.10	Mg-rich
GA-L-99-123	1.517	61.02	Mg-rich
GA-L-99-128	1.518	61.02	Mg-rich
GA-L-99-135	1.519	60.93	Mg-rich
GA-L-99-139	1.518	60.96	Mg-rich
GA-L-99-143	1.519	60.94	Mg-rich
GA-L-99-147	1.514	61.20	Fe+Al-rich
GA-L-99-156	1.518	60.99	Mg-rich
GA-L-99-157	1.519	60.94	Mg-rich
GA-L-99-160	1.515	61.14	Fe+Al-rich

GA-L-99-163	1.511	61.28	Fe+Al-rich
GA-L-99-165	1.514	61.14	Fe+Al-rich

Five sample d_{060} readings are shown in Figure 3.8, where the distinction between readings due to cation occupancy in the octahedral layers is observed. In this figure, GA-L-99-99 has the most dioctahedral occupancy at 1.509Å, while GA-L-99-91 and GA-L-99-160 are both dioctahedral as well, but with more Mg^{2+} occupancy. GA-L-99-21 and GA-L-99-101 fall into the trioctahedral phase with more Mg^{2+} content. While the d060 readings are excellent indicators for cation occupancy, there is also overlap due to the presence of Ferric and Ferrous Iron, in the Fe-rich montmorillonite, as mentioned previously. FTIR data helps narrow down the clays octahedral occupancy and distinguish between authigenic clays formed from diagenesis and detrital clays deposited from the NVH (Mees et al., 2007, Deocampo, 2004). EMPA data was assumed to have Ferric Iron occupancy in weight percent.

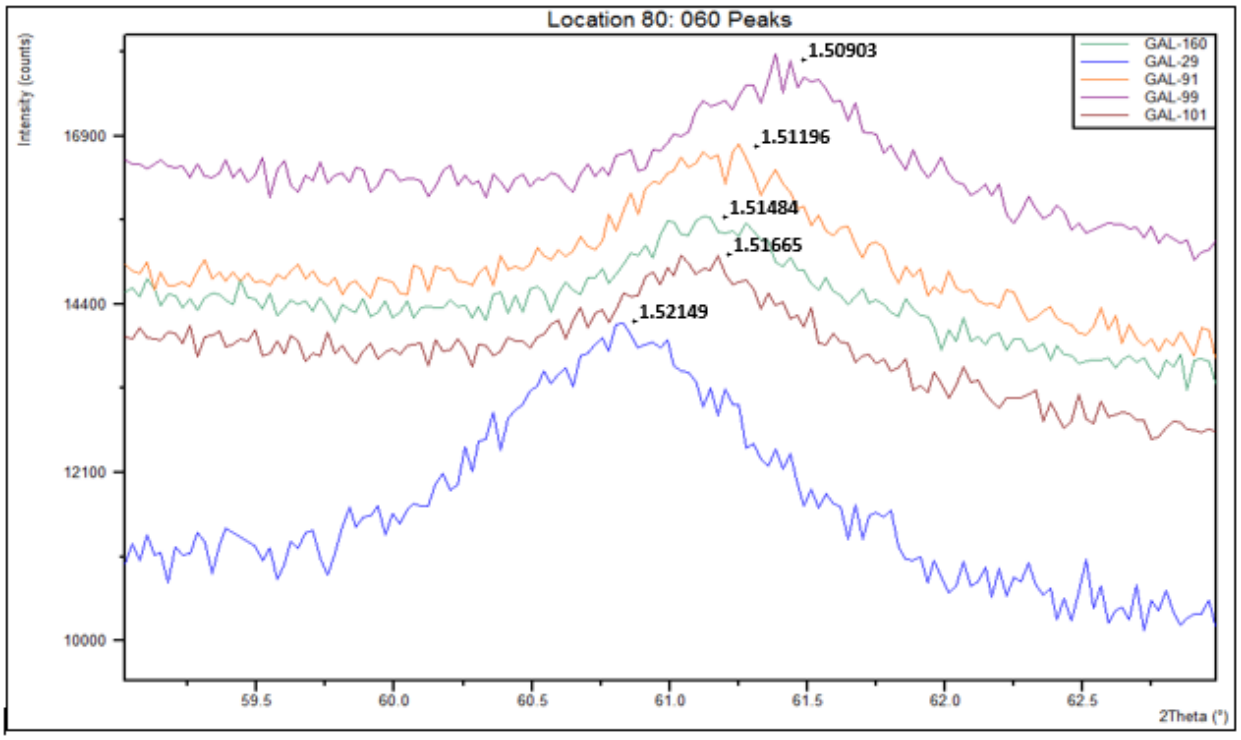

Figure 3.8 d060 peaks from Olduvai Gorge: Locality 80

3.4 FTIR Data Discussion

The FTIR data proved to show smaller peaks than expected with normal, fully-crystallized clays. The clays, exhibited what is common for the area when considering authigenic material, as it has been previously found that no purely trioctahedral phase of smectite has been detected in the lake basin (Mees et al., 2007; Deocampo, 2004). When considering the peaks indicating octahedral cation phases, the area under the curve was calculated for the pure Fe^{3+} and Mg^{2+} phase peaks (Equation 3.1) to identify correlation with bulk XRF geochemistry collected by Berry (2012). The area under the curve for each cation phase was determined by the following formula, using IR peak identification found in Deocampo et al. (2009):

Equation 3.1 Area under the curve cation calculation for FTIR data

$$\frac{(Mg^{2+})}{(Mg^{2+} + Fe^{3+} + Al^{3+})} \qquad \frac{(Fe^{3+})}{(Mg^{2+} + Fe^{3+} + Al^{3+})}$$

An octahedral occupancy of Al^{3+} was found in GA-L-99-4, 92, and 112 indicating the presence of kaolinite or dioctahedral Al-rich smectite in the samples. There was an abundance of trioctahedral Mg^{2+} and dioctahedral Fe^{3+} peaks, therefore only a correlation of bulk geochemistry and Fe^{3+} and Mg^{2+} clays was generated. Additionally, some samples did not have peaks for Fe^{3+} and Mg^{2+}, so in linear correlation analysis, they were not included in the data. Out of the 40 samples analyzed, 25 had values for Fe^{3+} and Mg^{2+} which could be correlated for potential significance with bulk geochemistry. Of those 25, 2 samples, GA-L-4-99 and GA-L-56-99 were excluded from the comparison due to extraneous outliers in the data. These two samples both had questionable peaks that were not completely identified as pure phases of the octahedral cations.

The Mg_3 hydroxyl-bending peak was identified as 654 cm^{-1} (Deocampo et al., 2009). When comparing the trioctahedral (Mg-rich) FTIR area under the curve ratios and XRF $MgO/(Al_2O_3 + Fe_2O_3)$ bulk geochemistry ratios (Figure 3.9), the correlation was 0.55 and a p value of <.0001. This is a strong

positive correlation indicating an increase in Mg^{2+} within the bulk samples and in octahedral Mg^{2+} content in the authigenic clay. This indicates the diagenetic processes that form Mg-rich clays also affect the geochemistry within the bulk samples found in the stratigraphy of the lake basin.

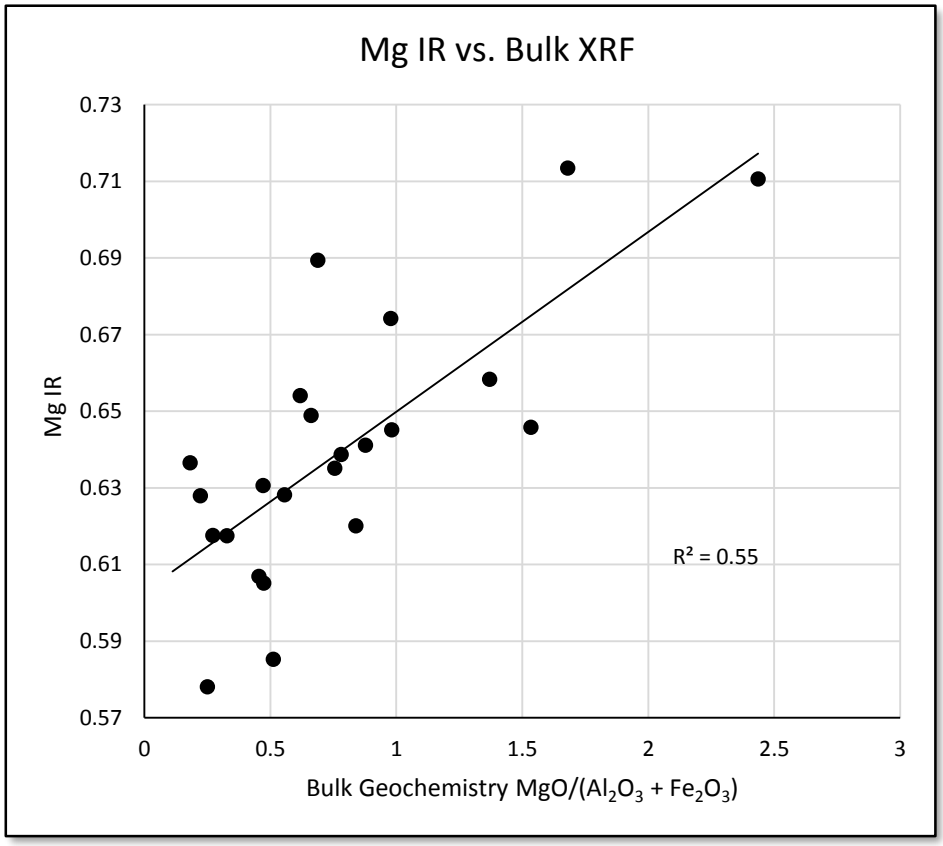

Figure 3.9 Mg^{2+} IR scan area under the curve correlated with bulk XRF ratio

Additionally, a correlation was found comparing the bulk geochemical readings and Fe-rich clays. In this case, the smectites found in the samples are either nontronite or Fe-rich montmorillonite, with some Mg^{2+} and Al^{3+} present. This correlation used the Fe_2 hydroxyl- bending peak at 816 cm^{-1} as found in Deocampo et al. (2009) with the removal of outliers GA-L-99-4 and 56 due to unclear peaks within the infrared data. With a R^2 value of 0.55, the bulk geochemistry ratio expressed as $MgO/(Al_2O_3+Fe_2O_3)$ increases with a decline in Fe cations (Figure 3.10). Potentially indicating a relationship between the presence of less altered detrital clays and Fe found in the bulk samples. Indicating the lack of diagenesis

due to freshwater flushing and detrital deposition in the area during wetter periods in the paleoenvironment.

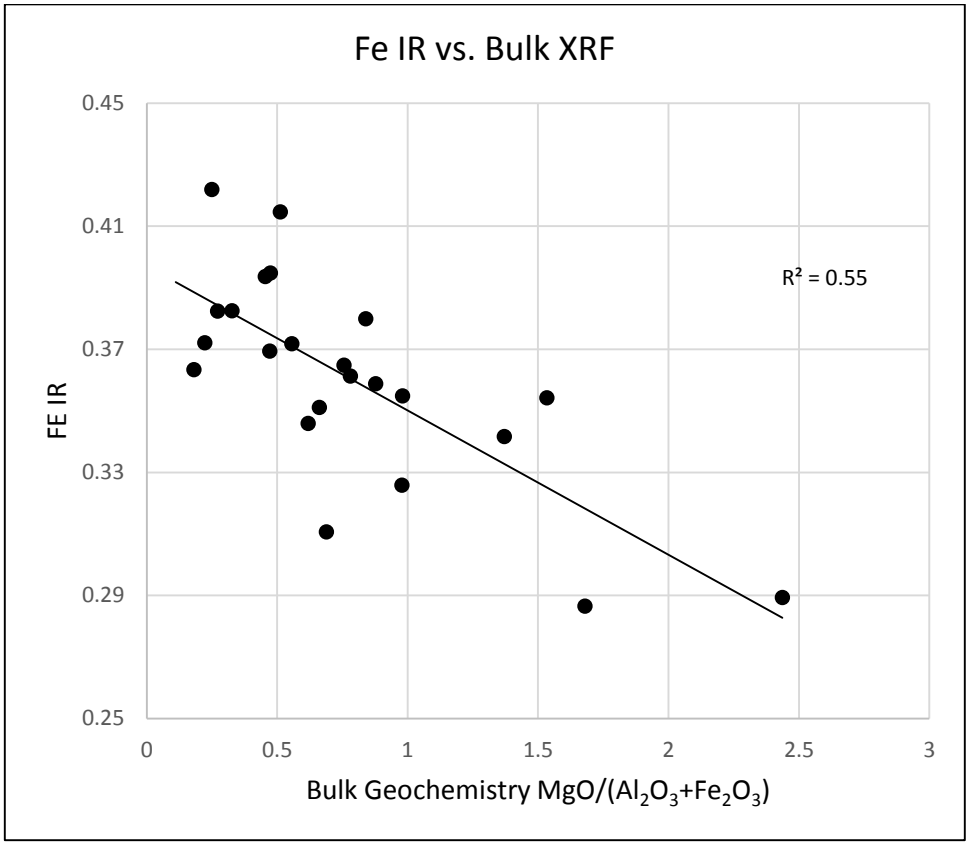

Figure 3.10 Fe^{3+} IR scan area under the curve correlated with bulk XRF ratio

3.5 XRD Data Discussion

XRD oriented clay readings were cross-referenced with the d060 scans to identify the octahedral occupancy of the material. The pure illite clays: GA-99-4, 45, 160, 163, and 165 were identified possibly detrital or purely authigenic. The potential detrital origin would result from very little diagenetic alteration due to the lack of interstratification with smectite and reduced Mg^{2+} content, which was confirmed as low from the EMPA analysis and d060 XRD scans (Table 3.4). Interstratified illite-smectite indicates saline and alkaline environments due to the important sink for Mg in clays (Hay and Kyser, 2001), which was not shown in these samples. High K^{+} values for these samples also indicates a

possibility that these illites are purely authigenic, formed from the uptake of K^+ through early diagenesis of saline and alkaline fluids or the wetting and drying of detrital dioctahedral smectite through the illitization of smectite (Jones, 1986; Eberl, 1993; Crawford and Haynes, 2002; Lanson et al., 2009). Mechanisms for pure authigenic illite formation, in this specific case, would need to be investigated further.

Table 3.4 XRD and EMPA Results

	XRD Results		EMPA Results	
Sample ID	**d060**	**Identified Clay**	**K_2O**	**$(Al_2O_3+Fe_2O_3)$ /MgO**
GA-L-99-4	1.506-1.511	Illite	6.2	3.8
GA-L-99-11	1.523	Illite-Smectite	6.5	1.2
GA-L-99-14	1.524	Illite-Smectite	2.0	0.4
GA-L-99-21	1.522	Illite-Smectite	2.0	0.2
GA-L-99-25	1.520-1.523	Smectite, Kaolinite	5.3	4.6
GA-L-99-29	1.521	Illite-Smectite	4.9	0.6
GA-L-99-35	1.518	Illite-Smectite	4.2	0.5
GA-L-99-37	1.522	Illite-Smectite	2.9	1.1
GA-L-99-38	1.508-1.512	Illite-Smectite	5.7	1.1
GA-L-99-45	1.522	Illite	5.5	1.4
GA-L-99-47	1.521	Illite-Smectite	4.4	0.8
GA-L-99-50	1.519	Illite-Smectite	2.6	1.4
GA-L-99-53	1.521	Illite-Smectite	3.9	0.5
GA-L-99-56	1.523	Illite-Smectite	2.8	0.6
GA-L-99-58	1.523	Illite-Smectite	5.2	1.1
GA-L-99-62	1.52	Illite-Smectite	4.6	0.7
GA-L-99-65	1.513	Illite-Smectite	6.3	1.2
GA-L-99-78	1.523	Illite-Smectite	4.0	0.6
GA-L-99-84	1.517	Illite-Smectite	3.9	0.4
GA-L-99-87	1.518	Illite-Smectite	2.9	0.3
GA-L-99-91	1.512-1.520	Illite-Smectite	3.9	0.6
GA-L-99-92	1.518	Smectite, Kaolinite	5.1	1.4
GA-L-99-95	1.514	Illite-Smectite, Kaolinite	8.0	1.8
GA-L-99-97	1.518	Illite-Smectite, Kaolinite	6.8	1.4
GA-L-99-99	1.512-1.509	Illite-Smectite	5.8	1.3
GA-L-99-101	1.517	Illite-Smectite	5.1	0.9

GA-L-99-104	1.518	Illite-Smectite	3.3	1.4
GA-L-99-112	1.52	Illite-Smectite	3.0	0.4
GA-L-99-120	1.516	Illite-Smectite	5.0	1.1
GA-L-99-123	1.517	Illite-Smectite	3.8	0.5
GA-L-99-128	1.518	Illite, Smectite, Kaolinite	4.9	0.7
GA-L-99-135	1.519	Illite-Smectite	4.2	0.5
GA-L-99-139	1.518	Illite-Smectite	4.3	0.7
GA-L-99-143	1.519	Illite-Smectite	5.6	1.0
GA-L-99-147	1.514	Illite-Smectite	5.4	1.0
GA-L-99-156	1.518	Illite- Smectite	4.8	0.6
GA-L-99-157	1.519	Illite-Smectite	5.4	1.7
GA-L-99-160	1.515	Illite	6.4	2.0
GA-L-99-163	1.511	Illite	5.6	1.7
GA-L-99-165	1.514	Illite	6.6	1.0

The remaining samples had variable transitioning occupancy from more Fe^{3+} to more Mg^{2+}-rich in the octahedral layer, while ~72% of the samples had d060 peaks indicating Mg-rich occupancy. There were still varying amounts of Fe + Al occupancy within the octahedral layer, which was overshadowed by the presence of more Mg^{2+} and less Fe^{3+} and Al^{3+} in the structure.

As stated the above results section 3.3.2, 060 XRD patterns indicated dioctahedral and trioctahedral phases throughout the sample selection. To see if the diagenesis of the detrital material into either an authigenic trioctahedral illite or smectite affected the bulk geochemistry, d060 angstrom peaks were correlated with the bulk geochemistry $(Al_2O_3+Fe_2O_3)/MgO$ ratios collected XRF data from Berry (2012). GA-25, 38, 65, 91 and 99-99 were also removed as outliers from the correlation due to inconclusive peaks after three separate d060 readings.

The correlation (Figure 3.11) of d060 readings as the dependent variable and bulk geochemistry XRF readings from Berry (2012) had a correlation of $R^2 = 0.27$. While not a strong correlation, it is still present, showing trends in d060 readings and the ratio of $(Al_2O_3+Fe_2O_3)/MgO$. There is a decrease in d060 values with reduction in Al_2O_3 and Fe_2O_3 in the bulk XRF data, which supports previous

observations that a decrease in angstrom peaks, as well as 060 angles, indicates more Al^{3+} and Fe^{3+} in both the bulk and clay geochemistry (Moore and Reynolds, 1997). The effect on bulk geochemistry with diagenesis of clays within the lake basin over time is indicated by similarities in the oxide ratios.

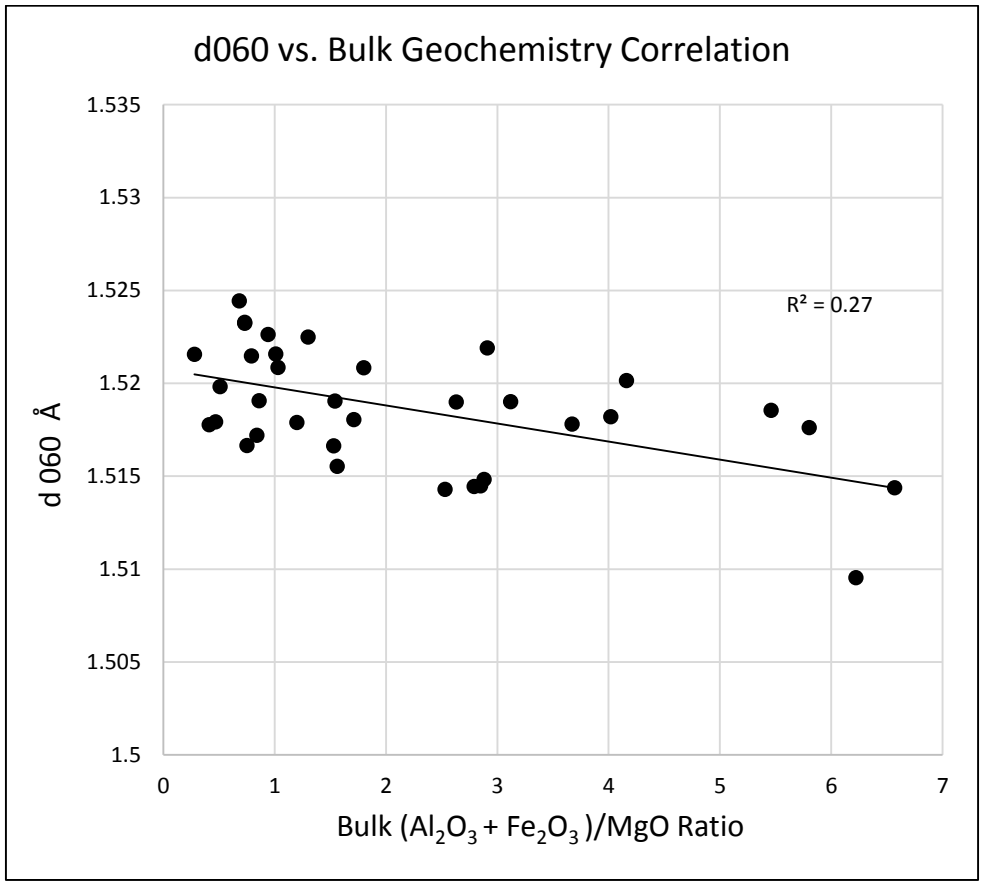

Figure 3.11 d060 subfraction XRD readings correlated with bulk geochemistry XRF ratios

3.6 EMPA Data Discussion

The weight percent measured by EMPA of MgO, Al_2O_3, and Fe_2O_3 for each sample were calculated and analyzed. Of the purely illitic samples (GA-L-99-4, 45, 160, 163, and 165) identified by the XRD analyses, the $(Al_2O_3 + Fe_2O_3)/MgO$ ratios exceeded 1.7, which were the highest in Al and Fe content with the exceptions of GA-L-99-25 and GA-L-99-37. The 2 latter samples were identified as heterogenous after comparing with their FTIR scans in which there is evidence of authigenic carbonate and feldspar bands. The illites with higher dioctahedral cation occupancy was concluded to be a detrital, muscovite-like phase, originating from the NVH as previously identified in Mees et al. (2007). All other samples had

varying weight percent data of $Al_2O_3 + Fe_2O_3$ and MgO occupancy, indicating diagenetic processes and interstratification of illite-smectite.

A correlation plot for the XRF bulk geochemistry and EMPA data was constructed to identify the relationship between clay diagenesis and bulk rock geochemical composition. The ($Al_2O_3 + Fe_2O_3$) /MgO ratio of weight percent for the bulk XRF and EMPA clay data were compared on a correlation plot (Figure 3.12). The results indicated an increase in ($Al_2O_3 + Fe_2O_3$) within the bulk samples when there was an increase in ($Al_2O_3 + Fe_2O_3$) on the molecular level as indicated by the EMPA scans. A strong positive correlation was observed between the two at R=0.69. Five samples; GA-L-99-4, 25, 95, 104 and 128, were removed from the correlation due to fluctuating readings caused by sample heterogeneity, as well as GA-L-99-53 and 99 due to the presence of carbonate. These samples particularly proved difficult in regards to extracting the submicron fraction due to lack of material available after centrifugation. Other minerals, particularly carbonates, were identified by high CaO weight percent in the samples and therefore identified as contaminated.

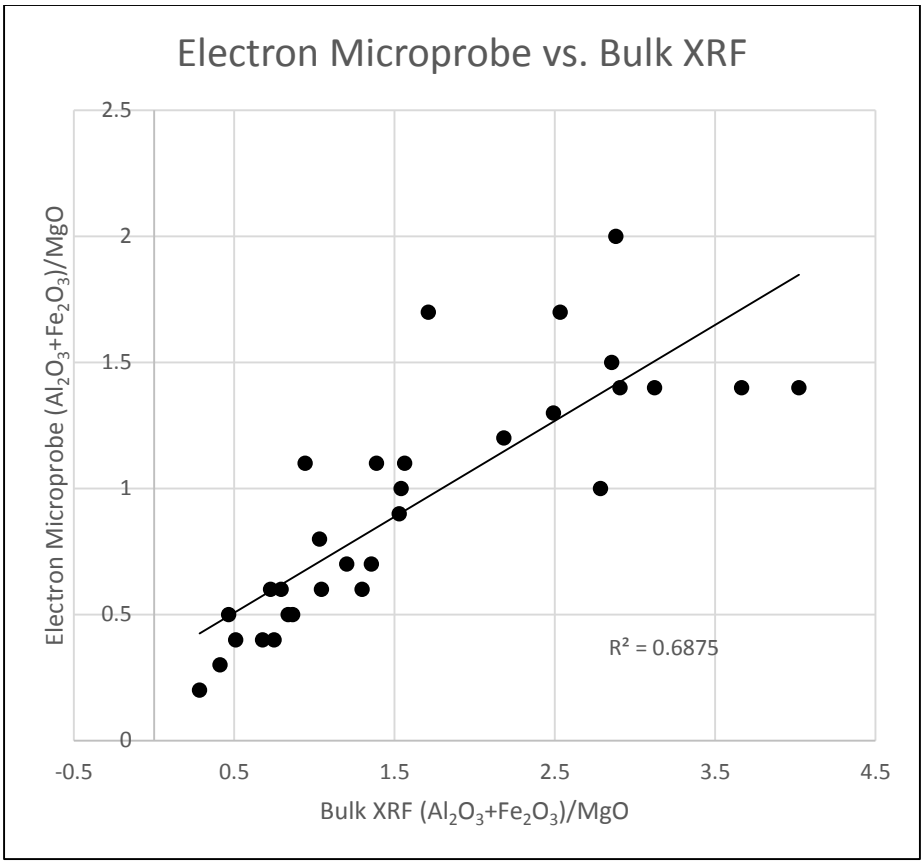

Figure 3.12 Bulk XRF geochemical data and EMPA weight percent

3.6.1 EMPA Time-Series

Additionally, a time-series plot was created according to the ages assigned to the core by Dr. Gail Ashley in 1999 at time of excavation, and compared with the bulk XRF time-series plot generated by Patricia Berry's the bulk XRF results (Figure 2.1). The EMPA time-series was smoothed by applying a three-point moving average to help test for cyclicity between more humid (higher Al_2O_3+Fe_2O_3 content) and more arid (MgO content) paleoevironments (Figure 3.13).

As seen in the figure, major events of salinity are indicated by trends of Mg-rich bulk and clay composition and more humid climate conditions are indicated by higher Fe and Al constituents in the bulk and clay samples. Five specific fluctuations in climate are identified by lines in red. Along the 25.0 meter mark in Unit 3, there is a noticeable abundance in MgO, indicating more arid conditions, the higher Mgo content corresponds to ~1.804 mya. Additionally, in Unit 1 of the stratigraphy, there are two

evident swings in arid climate conditions along the ~1.860 (14.0m) and ~1.909 (7.5m) mya mark due to the abundance of correlating MgO rise in both clay and bulk composition. Before the ~1.909 mya mark in the sample selection, there is evidence of wetter climate conditions due to a steady increase in Al^{3+} and Fe^{3+} as the depth increases, the first stratigraphic increase in MgO is at ~1.804 mya. Other wetter paleoclimatic shifts can be found at ~1.838 (20.0m) and ~1.884 (11.00m) mya. These ages are based on the age model of Hay and Kyser (2001).

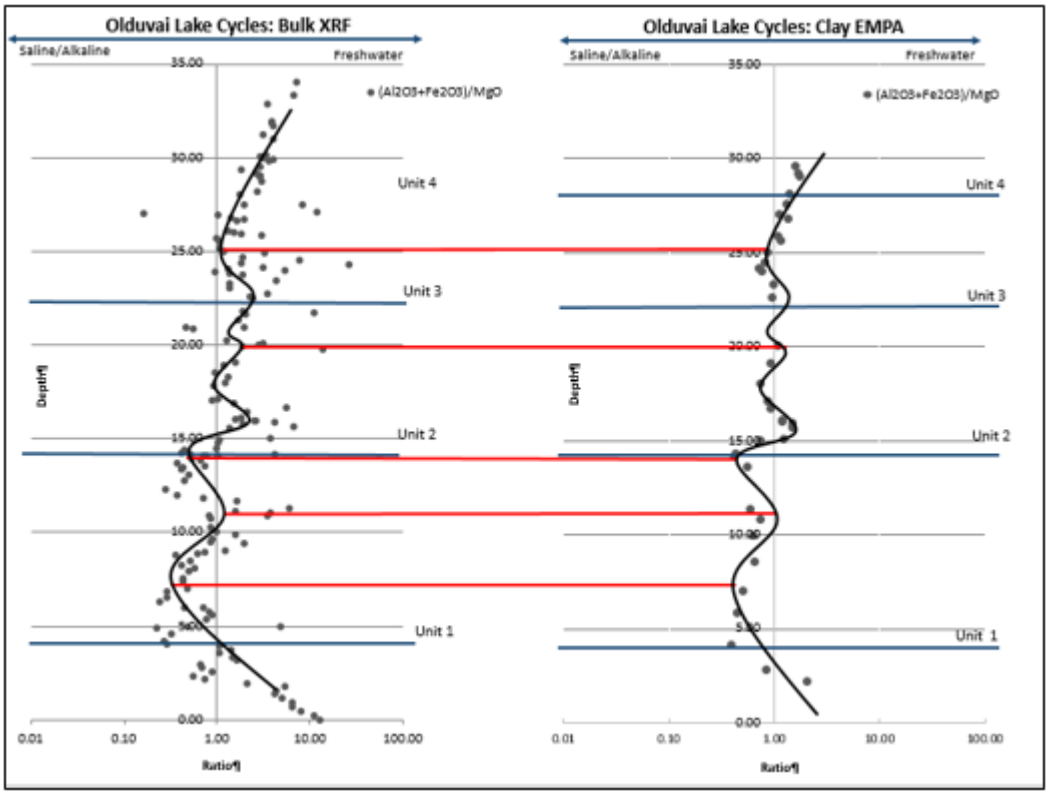

Figure 3.13 Bulk XRF and EMPA clay data time-series comparative analysis. Both curves show a 3-point running average.

4 CONCLUSIONS

Paleoclimatic shifts are important to understand due to the insight they provide into Earth processes and early evolution of species. East African paleolakes store important indicators that can reconstruct paleoclimate change over long periods of time (Hay, 1970; Ashley, 2007) Terrestrial mudstones, which are found in these lake beds, can form Mg-rich silicates if the following conditions are met: (1) the lake water is high in aqueous silica due to weathering volcaniclastics from a nearby source; (2) there are substantial time intervals in which there is low dilute inflow; (3) there is high evaporative concentration resulting in alkaline water chemistry (Deocampo, 2015).

These Mg-rich silicates can form *in situ* as phyllosilicates and can be used as proxies for paleoevironmental identification. The XRD air-dried and glycolated scans gave evidence for illite-smectite interstratified minerals, which are likely byproducts of authigenic Mg-rich clay layer formation of detrital dioctahedral smectite and kaolinite. Al+Fe-rich illite was also found at the top and bottom of the stratigraphy, either representing purely a detrital phase or an authigenic illite formed with higher K^+ ionic concentration in the lake. Additionally, the d060 readings coupled with the clay analysis indicated Mg-uptake in the majority of samples, while some samples had less Mg than others, of which there was less diagenetic alteration.

FTIR results gave insight into large amounts of Mg-rich clays as well as an abundance of Fe^{3+} and some Al^{3+} in the octahedral layer, coupling well the XRD results. Detrital kaolinite, along with dioctahedral smectite, are found throughout the section indicating more humid climate conditions. EMPA analysis weight percent data proved the presence of variations of divalent and trivalent cation octahedral occupancy. Which coincides with the FTIR readings and the clay samples showing trends of less alteration into fully-formed authigenic clays, due to the lack of time or conditions for full Mg-silicate facies formation, indicating a more humid climate.

When correlating the data collected with the bulk composition XRF results, there are similarities in the trends of octahedral cation occupancy within the clays and the bulk samples. Therefore, detrital processes involved in forming authigenic clays alters bulk composition, and reflects changes in paleoenvironment when monitoring cation abundance in clay samples. Bulk geochemical data in such paleolakes, which may be collected as discrete samples or with core-scanning XRF technologies, can therefore provide perspectives on submicron-scale authigenic phases.

4.1 Future Work

Using authigenic clays as paleoclimate indicators will need to be explored further, since there is not a lot of research regarding the identification of paleoclimate shifts using these clays in areas with similar conditions. It would be wise to study some areas in which authigenic clays have formed in similar lake beds and comparing it to previously studied climatic changes from other studies.

Regarding Olduvai, another stratigraphic section from a separate area ~300 meters away from Locality 80 was collected by Dr. Deocampo and PhD candidate Nathan Rabideaux from Georgia State University in July 2015, the clays have been extracted and d060 scans are being analyzed for similarities in cation octahedral occupancy and compared to Locality 80 results. Similarities will indicate and help solidify the potential for using these authigenic clays as proxies for ancient climatic shifts.

REFERENCES

Ashley, G.M. 2007. Orbital rhythms, monsoons, and playa lake response, Olduvai Basin, equatorial East Africa (ca. 1.85-1.74 Ma). Geology, v. 35, p. 1091-1094.

Ashley, G.M. Tactickos, J.C. and Owen, R.B. 2009. Hominin use of springs and wetlands: Paleoclimate and archeological records from Olduvai Gorge (similar to 1.79-1.74 Ma). Palaeogeogrpahy, Palaeloclimatology, Palaeoecology. v. 52, p. 1-16.

Berry, P.A. 2012. Lake Cycles and Sediments: Locality 80, Olduvai Gorge, Tanzania. Unpublished M.S. Thesis, Georgia State University, 72 pp.

Bobe, R. and Behrensmeyer, A.K. 2004. The expansion of grassland ecosystems in Africa in relation to mammalian evolution and the origin of the genus Homo. Palaeogeography, Palaeoclimatology, Palaeoecology, v. 207, p. 399-420.

Boggs, S. 1995. Principles of Sedimentology and Stratigraphy. New York, New York, Pearson, Inc.

Bradley, W.H. and Fahey, J.J. 1962. Occurrence of stevensite in the Green River Formation of Wyoming. American Mineralogist, v. 47, p. 996-997.

Bragg, W.H. 1912. On the direct or indirect nature of the ionization by X-rays. Phil. Mag., v. 35, p. 647.

Bristow, T.F., Kennedy, M.J., Morrision, K.D., and Mrofka, D.D. 2012. The influence of authigenic clay formation on the minerology and stable isotopic record of lacustrine carbonates. Geochemica et Cosmochimica Acta, v. 90, p. 64-82.

Carto, S.L., Weaver A.J., Hetherington R., Lam Y. and Wiebe E.C. 2009. Out of Africa and into an ice age: on the role of global climate change in the late Pleistocene expansion of early modern humans out of Africa. Journal Human Evolution, v. 56, p. 139-151.

Carroll, A.R. and Bohacs, K.M. 1999. Stratigraphic classification of ancient lakes: balancing tectonic and climatic controls. Geology, vol. 27, p. 99-102.

Cohen, A.S. 2003. Paleolimnology, the history and evolution of lake systems. Oxford University Press, 528 pp.

Crawford, E.W. and Haynes, J.T. 2002. The chemical character of fluids forming diagenetic illite in the southern Appalachian Basin: American Mineralogist, v. 87, p. 1519-1527.

Cuadros, J. and Dudek, T. 2006. FTIR investigation of the evolution of the octahedral sheet of kaolinite-smectite with progressive kaolinization. Clays and Clay Minerals, v. 54, p. 1-11.

Cullity B.D. 1978. Elements of X-Ray Diffraction (2nd ed.). Addison-Wesley Publishing Company. Reading, Massachusetts: 470 pp.

demenocal, P.B. 1995. Plio-Pleistocene African Climate. Science, v. 270, p. 53-59.

deMenocal, P.B. 2004. African climate change and faunal evolution during the Plio-Pleistocene. Earth and Planetary Science Letters, v. 220, p. 3-24.

Deocampo, D.M. 2004. Authigenic clays in East Africa: Regional trends and paleolimnology at the Plio-Pleistocene boundary, Olduvai Gorge, Tanzania. Journal of Paleolimnology, v. 31, p. 1-9.

Deocampo, D.M. 2005. Evaporative evolution of surface waters and the role of aqueous CO2 in magnesium silicate precipitation: Lake Eyasi and Ngorongoro Crater, northern Tanzania. South African Journal of Geology, v. 108, p. 493-504.

Deocampo, D.M., Cuadros, J., Wing-Dudek, T., Olives, J., and Amouric, M. 2009. Saline lake diagenesis as revealed by coupled mineralogy and geochemistry of multiple ultrafine clay phases: Pliocene Olduvai Gorge, Tanzania. American Journal of Science, v. 309, p. 834-868.

Deocampo, D.M. and Jones, B.F. 2013. Geochemistry of Saline Lakes. *Treatise on Geochemistry*, v. 5, p. 82-89.

Deocampo, D.M. 2015. Authigenic clay minerals in lacustrine mudstones. The Geological Society of America, Special Paper 515, p. 49-59.

Dunn, T. 1989. MZAF: A BASIC program for off-line correction of electron microprobe data by the ZAF method. Computers and Geosciences. v. 15, p. 9-17.

Dyni, J.R. 1976. Trioctahderal smectite in the Green River Formation, Duchesne County, Utah: An X-Ray diffraction study of clay minerals in some lacustrine rocks of Eocene age exposed in the southwestern part of the Uinta Basin. U.S. Geological Survey Professional Paper 967. p. 14.

Eberl, D. D. 1993. Synthesis of Illite-Smectite from Smectite at Earth Surface Temperatures and High pH: Clay Minerals, v. 28, p. 49-60.

Forester, V., Junginger, Langkamp, A., Tsige, O., Afsawossen, G., Umer, A., Lamb, M., Wennrich, H., Rethemeyer, V., Nowaczyk, J., Trauth, M., Schaebitz, F. 2012. Climactic change records in the sediments of the Chew Bahir basin, Southern Ethiopia during the last 45,000 years. Quaternary International, v. 274, p. 25-37.

Freedman, D. 2009. Statistical Models: Theory and Practice. Cambridge University Press, London, UK. 507 pp.

Fritz, S.C. 2008. Deciphering climatic history from lake sediments. Journal of Paleolimnology, vol. 39, p. 5-16.

Griffiths, P.R. and DeHaseth, J.A. 2007. Fourier Transform Infrared Spectroscopy. Wiley, UK. 560 pp.

Hay, R.L. 1970. Silicate reactions in three lithofacies of a semiarid basin, Olduvai Gorge, Tanzania. Mineralogical Society of America Special Paper v. 3, p. 237-255.

Hay, R.L. 1976. Geology of the Olduvai Gorge. University of California Press, 203 pp.

Hay, R. L. 1990, Olduvai Gorge; A case history in the interpretation of hominid paleoenvironments in East Africa, in Laporte, L. F., editor, Establishment of a Geologic Framework for Paleoanthropology: Geological Society of America Special Paper v. 242, p. 23–37.

Hay, R.L. and Kyser, T.K. 2001. Chemical Sedimentology and paleoenvironmental history of Lake Olduva, a Pliocene lake in northern Tanzania: Geological Society of America Bulletin, v. 113, p. 1505-1521.

Hover, V.C. and Ashley, G.M. 2003. Geochemical signatures of paleodepositional and diagenetic environments: a STEM/AEM study of authigenic clay minerals from an arid rift basin, Olduvai Gorge, Tanzania. Clays and Clay Minerals, v. 51, p. 231-251.

Hover, V. C., Ashley, G. M., Driese, S. G., Owen, R. B., and McBrearty, S. 2005. Authigenic Mg-rich smectite and 10-Aa clay minerals in East African Rift-valley lacustrine sediments; what do compositions tell you about geochemical depositional environments? Clay Minerals Society, v. 30, p. 54-55.

Jansen, W. and Slaughter, M. 1982.Elemental mapping with Electron Microprobe. American Mineralogist v.67, p. 521–533.

Jones, B.F. and Weir, A.H., 1983. Clay minerals in Lake Albert, an alkaline saline lake. Clays and Clay Minerals, v. 31, p. 161-172.

Jones, B.F. 1986. Clay mineral diagenesis in lacustrine sediments. In Mumpton, F.A. (Ed.), Studies in Diagenesis, U.S. Geological Survey Bulletin v. 1578, p. 291-300.

Jones, B.F. and Deocampo, D.M. 2003. Geochemistry of Saline Lakes. In Drever, J.I. (Ed.), Surface and Ground Water, Weathering, Erosion, and Soils. Treatise on Geochemistry, v. 5, p. 393- 424.

Kingston J.D. 2007. Shifting adaptive landscapes: progress and challenges in reconstructing early hominid environments. Am. J. Phys. Anthropol. v. 134, p.20-58.

Kloprogge, J.T. and Frost, R.L. 2001. Infrared emission spectroscopic study of the dehydroxylation of some natural and synthetic saponites: Neues Jahrbuch fur Mineralogie-Monatshefte, v. 10, p. 446–463.

Lanson, B. Sakharov, B. A., Claret, F., and Drits, V. A. 2009. Diagenetic smectite-to-illite transition in clay-rich sediments: A reappraisal of X-ray diffraction results using the multispecimen method: American Journal of Science, v. 309, p. 476-516.

Leng, M.J. and Marshall, J.D., 2004. Palaeoclimate interpretation of stable isotope data from lake sediment archives.Quaternary Science Reviews, v. 23, p. 811-831.

Mees, F. Segers, S., and Van Ranst, E. 2007. Palaeoenvironmental significance of the clay mineral composition of Olduvai basin deposits, northern Tanzania. Journal of African Earth Sciences, v. 47, p. 39-48.

Meunier, A. 2005. Clays. Springer, Berlin. 472 pp.

Moore, D. and Reynolds, R. 1997. X-Ray Diffraction and the Identification and Analysis of Clay Minerals.

Mollel, Godwin F. 2012. The Ngorongoro Volcanic Highland and its relationships to volcanic deposits at Olduvai Gorge and East African Rift volcanism. Journal of Human Evolution, v. 63, p. 274-283.

Owen, R.B., Renaut, R.W., Potts, R., and Behrensmeyer, A.K. 2011. Geochemical trends through time and lateral variability of diatom floras in the Pleistocene Olorgesailie Formation, southern Kenya Rift Valley. Quaternary Research, v. 76, p. 167-179.

Potts, R. 1996. Evolution and climate variability. Science, v. 273, p. 922-923.

Potts, R. 1998. Environmental hypotheses of hominin evolution. Yearbook of Physical Anthropology, v. 41, p. 93-136.

Potts, R. 1999. Variability selection in hominid evolution. Evolutionary Anthropology, v. 7, p. 81-96.

Potts, R. 2013. Hominin evolution in settings of strong environmental variability. Quaternary Science Reviews, v. 73, p. 1-3.

Reed, K.E. 1997. Early hominid evolution and ecological change through the African Plio-Pleistocene. J. Hum. Evol. v. 32, p. 289–322.

Reed, S.J. 2005. Electron Microprobe Analysis and Scanning Electron Microscopy in Geology. London, United Kingdom. Cambridge University Press.

Russell, D.J. and Fraser, A.R. 1994. Infrared methods, in Wilson, M. J., Editor, Clay Mineralogy: Spectroscopic and Chemical Determinative Methods: London, Chapman and Hall, p. 11–67.

Shankland, R.S. 1964. Michelson–Morley experiment. American Journal of Physics, v. 31, p.16–35.

Smith, M.E., Carroll, A.R., and Singer, B.S. 2008. Synoptic reconstruction of major ancient lake system: Eocene Green River Formation, western United States. Geological Society of America Bulletin, v. 120, p. 54-84.

Trauth, M.H., Maslin, M., Deino, A., and Strecker, M.R. 2005. Late Cenozoic moisture history of East Africa. Science, v. 309, p. 475-483.

Trauth, M.H., Larrasoana, J.C., and Mudelsee, M. 2009. Trends, rhythms and events in Plio-Pleistocene African climate. Quaternary Science Reviews, v. 28, p. 399-411.

Vrba, E.S., Denton, G.H., Partridge, T.C. and Burckle, L.H. 1995. Paleoclimate and Evolution. Yale University Press, New Haven. 545 pp.

Wilson M.J. 1992. Clay Minerology: Spectroscopic and Chemical Determinative Methods. London, United Kindom. Chapman and Hall, Inc.

Weaver, C.E. and Pollard, L.D. 1973. The Chemistry of Clay Minerals: Elsevier, Amsterdam, 213 pp

APPENDICES

Appendix A: Element Oxide data from EMPA (3 scans)

	Elements in Weight Percent									
SAMPLE ID	**Si**	**Ti**	**Al**	**Fe**	**Mg**	**Ca**	**Na**	**K**	**O**	**TOTAL**
GA-L-99-165	39.02	2.02	5.40	6.70	7.57	10.36	1.92	4.98	22.04	77.96
GA-L-99-165	39.80	2.13	5.23	6.47	7.08	9.71	1.41	5.08	23.09	76.91
GA-L-99-165	44.37	1.38	5.18	5.91	9.57	0.96	1.77	5.05	25.82	74.18
GA-L-99-163	41.32	1.25	3.95	8.87	8.15	10.27	0.72	4.26	21.21	78.79
GA-L-99-163	38.67	1.71	4.07	7.86	7.61	6.37	1.13	4.25	28.34	71.66
GA-L-99-163	40.65	1.18	3.84	8.16	8.11	9.22	0.96	4.08	23.79	76.21
GA-L-99-160	51.74	1.96	8.09	8.25	8.54	1.59	1.58	5.80	12.44	87.56
GA-L-99-160	53.30	1.48	6.88	10.17	9.72	0.67	1.60	5.53	10.64	89.36
GA-L-99-160	52.31	2.31	7.14	9.63	9.39	1.22	1.66	5.64	10.69	89.31
GA-L-99-156	51.33	1.44	4.16	7.09	13.14	0.24	2.45	5.72	14.44	85.56
GA-L-99-156	42.30	0.82	3.85	4.20	13.78	0.26	1.89	4.38	28.53	71.47
GA-L-99-156	20.69	0.29	2.35	0.38	8.65	0.13	1.64	1.22	64.66	35.34
GA-L-99-154	52.35	1.67	3.06	13.52	10.54	2.32	2.44	4.44	9.67	90.33
GA-L-99-154	52.89	1.55	3.13	13.68	10.58	2.14	2.63	4.28	9.11	90.89
GA-L-99-154	53.09	1.50	2.86	13.92	10.37	2.37	2.75	4.37	8.77	91.23
GA-L-99-147	46.67	0.67	6.13	4.96	11.33	0.17	1.91	4.06	24.10	75.90
GA-L-99-143	52.53	2.15	8.42	6.45	14.90	0.41	3.02	5.28	6.84	93.16
GA-L-99-143	52.54	1.81	7.49	6.99	14.53	0.38	2.14	4.90	9.21	90.79
GA-L-99-143	52.82	1.51	7.03	6.65	14.53	0.39	2.40	5.07	9.60	90.40
GA-L-99-139	54.84	0.76	5.43	6.02	16.66	0.23	2.68	4.01	9.38	90.62
GA-L-99-139	55.68	0.67	5.20	6.16	17.47	0.27	3.69	3.89	6.97	93.03
GA-L-99-139	56.35	0.81	5.35	6.18	16.86	0.27	2.89	3.90	7.38	92.62
GA-L-99-135	42.97	0.77	4.05	4.42	20.63	0.31	3.22	3.19	20.45	79.55

	Elements in Weight Percent									
SAMPLE ID	**Si**	**Ti**	**Al**	**Fe**	**Mg**	**Ca**	**Na**	**K**	**O**	**TOTAL**
GA-L-99-135	50.74	0.67	5.21	4.28	16.48	0.47	1.55	3.08	17.51	82.49
GA-L-99-128	50.19	0.65	4.49	6.13	17.03	0.32	2.83	4.01	14.36	85.64
GA-L-99-128	51.56	1.12	4.59	7.89	16.54	0.41	2.54	4.54	10.80	89.20
GA-L-99-128	52.70	1.21	4.86	7.07	17.11	0.43	3.38	4.41	8.83	91.17
GA-L-99-123	56.90	0.94	4.55	5.02	17.93	0.43	3.61	3.48	7.15	92.85
GA-L-99-123	56.62	0.96	4.62	4.99	17.82	0.49	3.83	3.45	7.21	92.79
GA-L-99-123	55.93	0.87	4.32	1.97	17.92	0.34	3.59	3.45	11.61	88.39
GA-L-99-120	55.09	1.31	5.90	6.99	13.88	0.32	4.65	4.53	7.33	92.67
GA-L-99-120	54.43	1.35	6.00	7.41	13.83	0.31	3.98	4.53	8.14	91.86
GA-L-99-120	55.53	1.28	6.23	6.93	13.77	0.28	4.79	4.65	6.53	93.47
GA-L-99-112	7.34	0.13	1.94	0.59	11.10	21.87	0.58	1.25	55.20	44.80
GA-L-99-112	56.03	0.71	4.28	3.86	21.45	1.13	2.72	2.80	7.01	92.99
GA-L-99-112	55.46	0.71	4.17	3.83	20.99	0.99	2.44	2.77	8.64	91.36
GA-L-99-104	55.09	0.66	3.03	13.02	13.53	0.66	3.56	2.86	7.59	92.41
GA-L-99-104	54.40	0.74	3.35	13.66	12.96	1.05	3.74	3.18	6.92	93.08
GA-L-99-104	54.17	0.74	3.17	13.98	13.11	0.95	3.96	3.05	6.87	93.13
GA-L-99-101	58.45	1.03	6.49	6.52	14.96	0.40	2.72	4.55	4.88	95.12
GA-L-99-101	52.12	1.05	5.94	7.00	14.17	0.47	2.29	4.58	12.36	87.64
GA-L-99-101	55.24	1.25	5.99	6.22	13.91	0.40	2.87	4.78	9.34	90.66
GA-L-99-99	52.41	1.38	6.18	8.53	12.79	0.71	1.95	5.17	10.88	89.12
GA-L-99-99	53.37	1.64	6.94	8.34	12.22	0.64	1.10	5.05	10.71	89.29
GA-L-99-99	52.78	2.30	7.04	8.38	11.61	0.71	1.85	5.25	10.08	89.92
GA-L-99-97	54.87	1.30	8.42	5.89	10.02	1.65	1.05	6.20	10.60	89.40
GA-L-99-97	44.87	1.31	6.85	6.44	10.44	1.83	1.08	5.32	21.87	78.13
GA-L-99-97	53.54	1.31	7.76	6.50	10.46	1.53	0.86	5.95	12.08	87.92
GA-L-99-95	54.41	0.86	9.23	5.97	8.63	2.47	1.36	7.36	9.71	90.29
GA-L-99-95	53.43	0.86	8.90	5.96	9.26	2.05	1.63	6.89	11.02	88.98
GA-L-99-95	53.63	0.89	9.15	6.08	8.90	2.65	0.71	7.20	10.78	89.22

	Elements in Weight Percent									
SAMPLE ID	**Si**	**Ti**	**Al**	**Fe**	**Mg**	**Ca**	**Na**	**K**	**O**	**TOTAL**
GA-L-99-92	43.54	1.73	5.14	8.00	10.55	6.25	1.12	3.94	19.73	80.27
GA-L-99-92	43.77	1.50	5.81	7.28	9.96	6.51	1.26	4.49	19.40	80.60
GA-L-99-92	44.21	1.63	5.37	8.33	10.82	5.85	1.13	3.92	18.75	81.25
GA-L-99-91	54.46	0.92	4.19	5.01	17.41	0.65	3.84	3.48	10.05	89.95
GA-L-99-91	53.45	1.13	4.60	5.67	16.73	1.12	2.86	3.46	10.97	89.03
GA-L-99-91	49.98	1.04	3.93	5.27	16.04	2.97	3.36	3.29	14.13	85.87
GA-L-99-87	56.99	0.61	2.85	3.33	21.03	0.40	3.80	2.61	8.37	91.63
GA-L-99-87	54.86	0.64	2.49	3.15	20.79	0.42	3.21	2.66	11.78	88.22
GA-L-99-87	58.81	0.60	2.77	3.06	21.60	0.32	3.88	2.61	6.36	93.64
GA-L-99-84	55.49	0.87	3.87	3.62	19.41	1.27	4.06	3.58	7.84	92.16
GA-L-99-84	48.43	0.83	3.27	3.77	19.69	1.13	4.04	3.31	15.53	84.47
GA-L-99-84	56.14	0.89	3.54	4.00	19.56	1.21	3.95	3.44	7.27	92.73
GA-L-99-78	53.10	0.86	4.44	6.47	20.30	0.68	3.10	3.58	7.45	92.55
GA-L-99-78	45.70	0.83	3.91	6.10	19.80	0.72	2.44	3.37	17.13	82.87
GA-L-99-78	51.72	0.86	4.55	6.20	20.36	0.59	3.03	3.52	9.18	90.82
GA-L-99-65	50.11	1.24	7.14	7.53	13.16	0.38	2.55	5.55	12.34	87.66
GA-L-99-65	48.51	1.19	6.58	7.62	12.72	0.45	2.44	5.75	14.74	85.26
GA-L-99-65	54.73	1.15	7.13	7.27	12.18	0.46	1.88	5.30	9.90	90.10
GA-L-99-38	52.62	2.45	5.70	8.63	13.17	1.15	1.67	5.22	9.40	90.60
GA-L-99-38	52.84	1.96	5.34	7.80	14.02	1.10	2.03	4.88	10.04	89.97
GA-L-99-38	50.96	2.98	5.78	8.01	12.11	1.96	1.51	5.16	11.52	88.48
GA-L-99-45	50.01	1.25	6.24	11.61	11.72	1.14	3.04	5.26	9.73	90.27
GA-L-99-45	51.16	1.07	6.46	11.57	12.52	1.22	2.85	5.15	7.98	92.02
GA-L-99-45	51.06	1.11	6.09	11.54	12.58	0.87	2.11	5.33	9.31	90.69
GA-L-99-45	51.52	1.25	4.96	7.14	17.20	0.69	2.15	4.11	10.97	89.03
GA-L-99-47	52.75	1.29	5.57	7.92	17.27	0.72	2.17	4.10	8.21	91.79
GA-L-99-47	52.42	1.24	5.42	7.41	17.14	0.71	1.88	4.00	9.79	90.21
GA-L-99-47	53.57	1.23	5.42	7.53	17.45	0.58	2.45	4.08	7.68	92.32

	Elements in Weight Percent									
SAMPLE ID	**Si**	**Ti**	**Al**	**Fe**	**Mg**	**Ca**	**Na**	**K**	**O**	**TOTAL**
GA-L-99-50	53.48	0.52	3.76	12.82	13.91	0.29	4.88	2.32	8.01	91.99
GA-L-99-50	53.41	0.64	4.02	13.07	13.40	0.33	4.86	2.36	7.91	92.09
GA-L-99-50	53.74	0.57	4.21	13.27	13.42	0.32	4.50	2.43	7.52	92.48
GA-L-99-53	53.39	0.49	2.58	6.91	19.43	0.29	4.23	3.44	9.24	90.76
GA-L-99-53	38.77	0.28	1.56	6.50	18.05	0.22	3.98	3.08	27.55	72.45
GA-L-99-53	54.19	0.43	2.66	6.61	19.58	0.43	3.60	3.54	8.95	91.05
GA-L-99-56	52.63	2.39	6.13	6.23	16.19	0.56	5.28	3.32	7.26	92.74
GA-L-99-56	54.05	1.01	4.69	4.68	19.70	0.43	5.30	2.37	7.76	92.24
GA-L-99-56	54.86	0.80	3.98	4.53	20.79	0.24	3.99	2.01	8.80	91.20
GA-L-99-58	50.36	2.52	6.34	7.67	14.11	1.41	2.01	4.55	11.02	88.98
GA-L-99-58	49.92	2.83	7.05	7.11	13.56	1.74	2.35	4.50	10.95	89.05
GA-L-99-58	42.98	2.84	6.54	7.19	13.63	1.64	2.44	4.52	18.22	81.78
GA-L-99-62	52.99	0.95	4.95	6.76	17.72	0.33	3.61	4.15	8.55	91.46
GA-L-99-62	53.10	0.99	4.80	6.43	17.84	0.34	3.00	4.17	9.32	90.68
GA-L-99-62	52.72	1.02	5.18	6.36	17.73	0.31	3.01	4.20	9.47	90.53
GA-L-99-37	22.92	0.43	3.88	1.83	3.88	22.63	0.82	2.81	40.79	59.21
GA-L-99-37	24.22	0.34	4.44	2.02	3.76	21.32	1.18	3.18	39.55	60.45
GA-L-99-37	19.58	0.32	3.83	1.94	3.57	23.73	1.09	2.79	43.14	56.86
GA-L-99-35	51.03	0.93	5.47	4.54	18.97	1.87	2.75	3.68	10.77	89.23
GA-L-99-35	50.93	0.95	5.55	4.21	19.29	1.97	2.79	3.70	10.61	89.39
GA-L-99-35	52.96	0.90	5.34	4.80	19.33	0.93	2.99	3.83	8.91	91.09
GA-L-99-29	43.58	0.87	5.15	4.98	17.67	2.31	2.26	3.90	19.28	80.72
GA-L-99-29	43.32	0.88	5.23	4.82	17.59	2.24	1.89	3.84	20.19	79.81
GA-L-99-29	43.51	0.88	5.02	5.22	17.60	2.00	1.87	3.97	19.95	80.05
GA-L-99-25	31.94	0.44	9.53	15.33	5.83	6.46	2.55	3.60	24.32	75.68
GA-L-99-25	29.24	0.35	6.02	15.80	6.25	6.37	1.83	2.61	31.53	68.47
GA-L-99-25	34.13	0.26	9.02	14.64	4.26	5.18	1.80	5.35	25.36	74.64

Appendix B: FTIR Infrared Spectra Scans

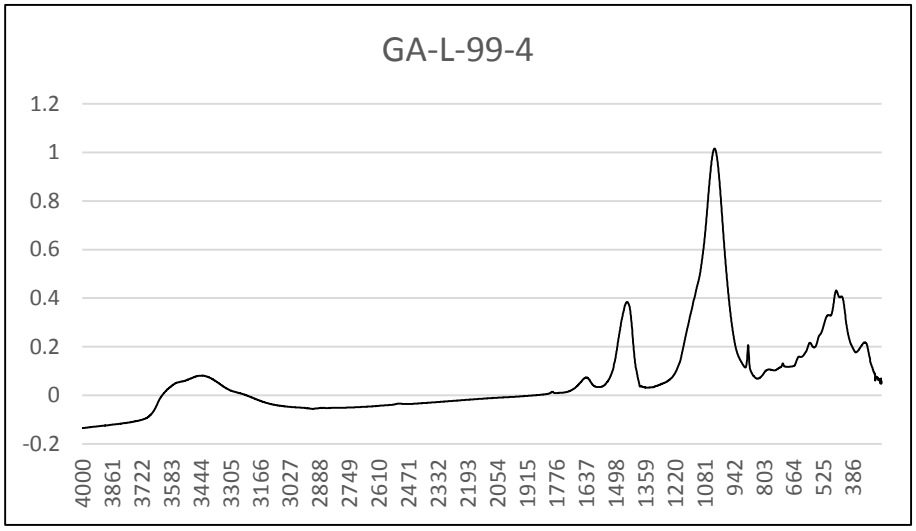

GA-L-99-4 Infrared Spectra

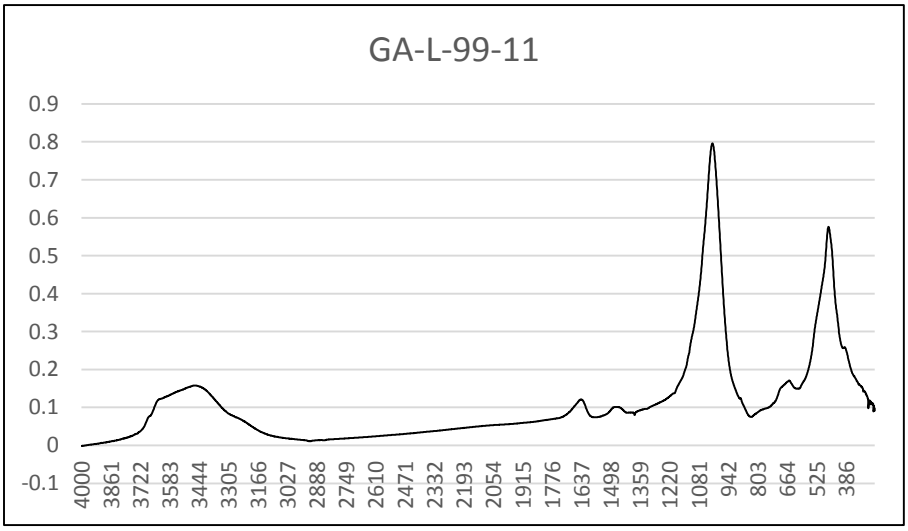

GA-L-99-11 FTIR Infrared Spectra

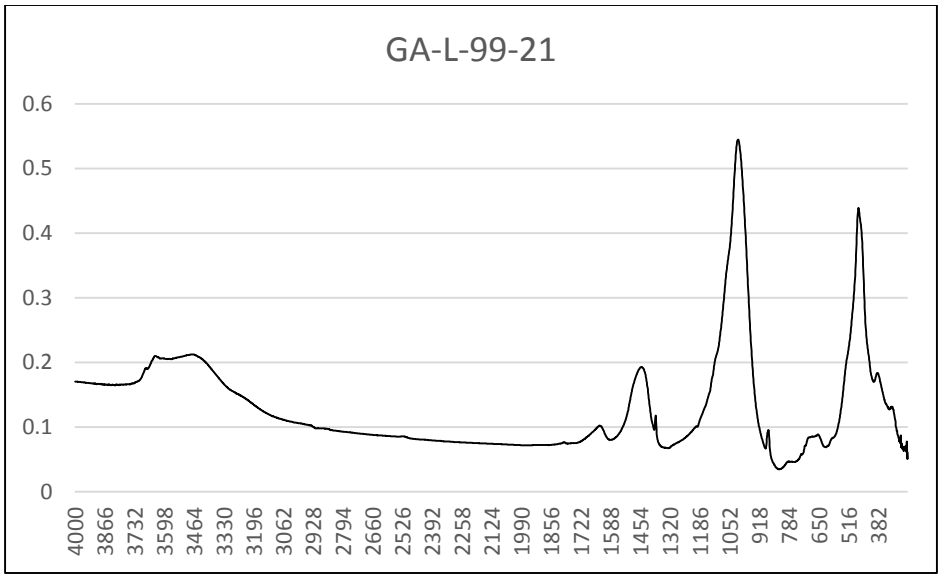

GA-L-99-21 FTIR Infrared Spectra

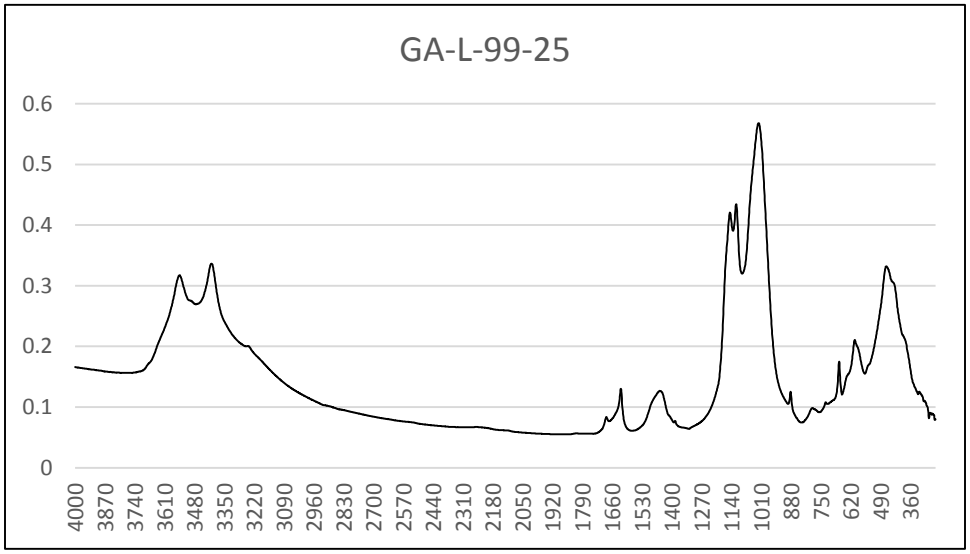

GA-L-99-25 FTIR Infrared Spectra

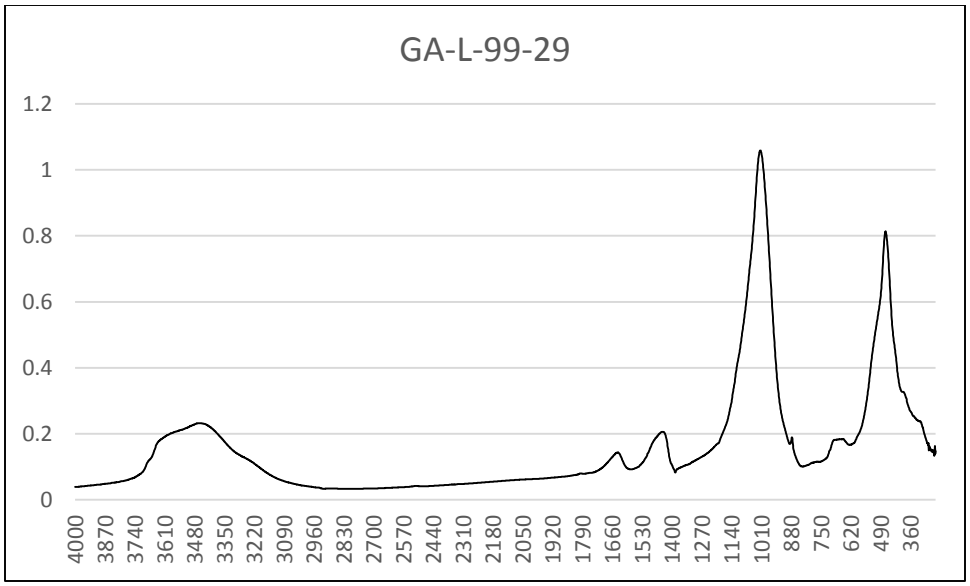

GA-L-99-29 FTIR Infrared Spectra

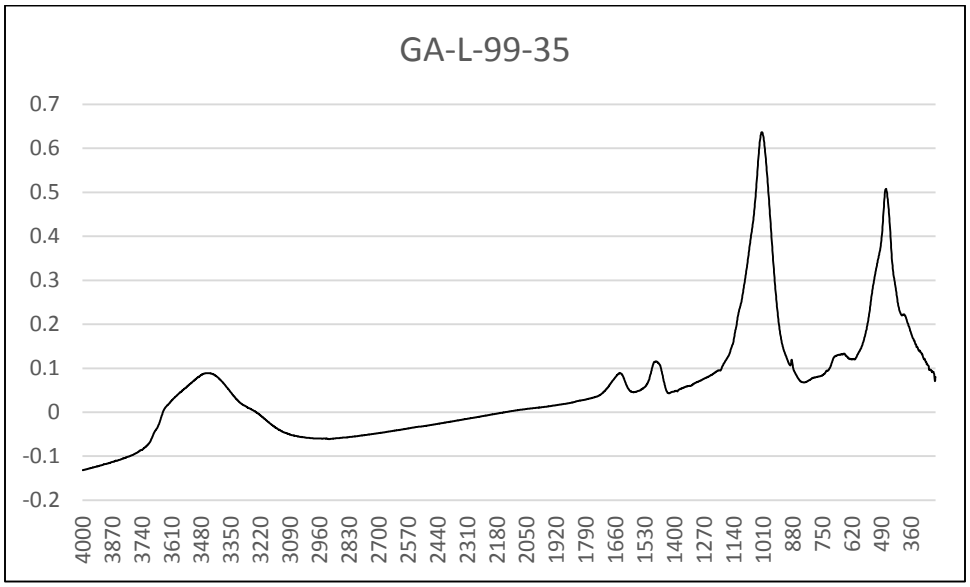

GA-L-99-35 FTIR Infrared Spectra

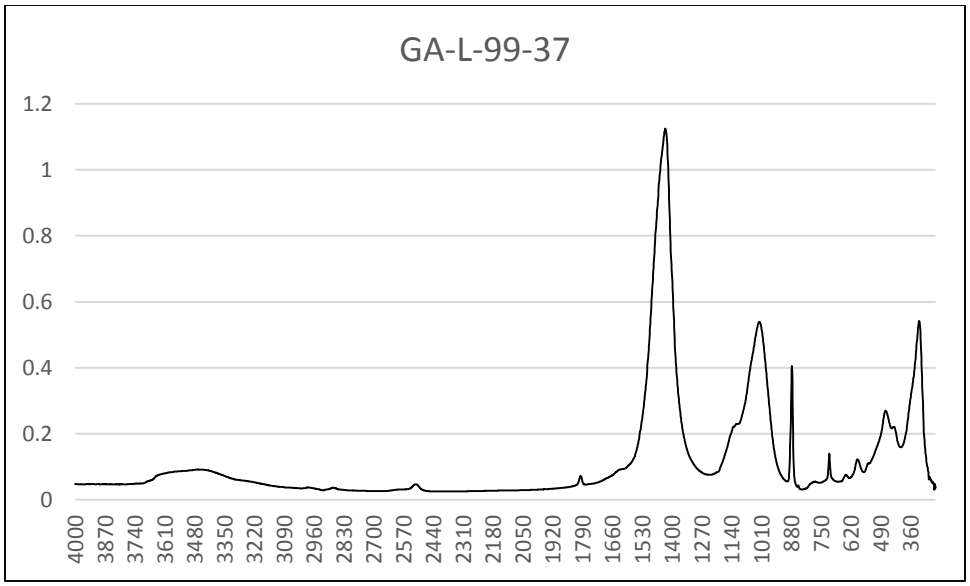

GA-L-99-37 FTIR Infrared Spectra

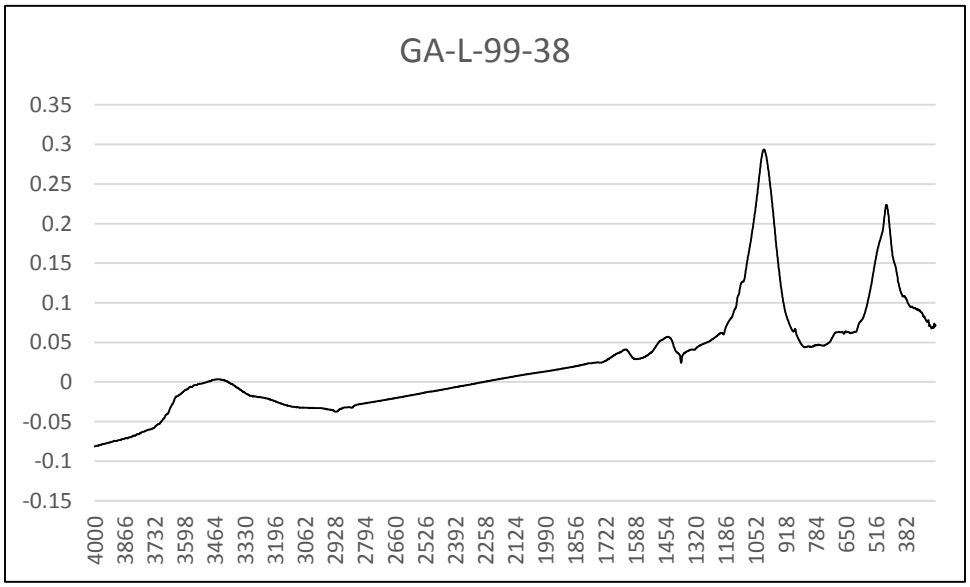

GA-L-99-38 FTIR Infrared Spectra

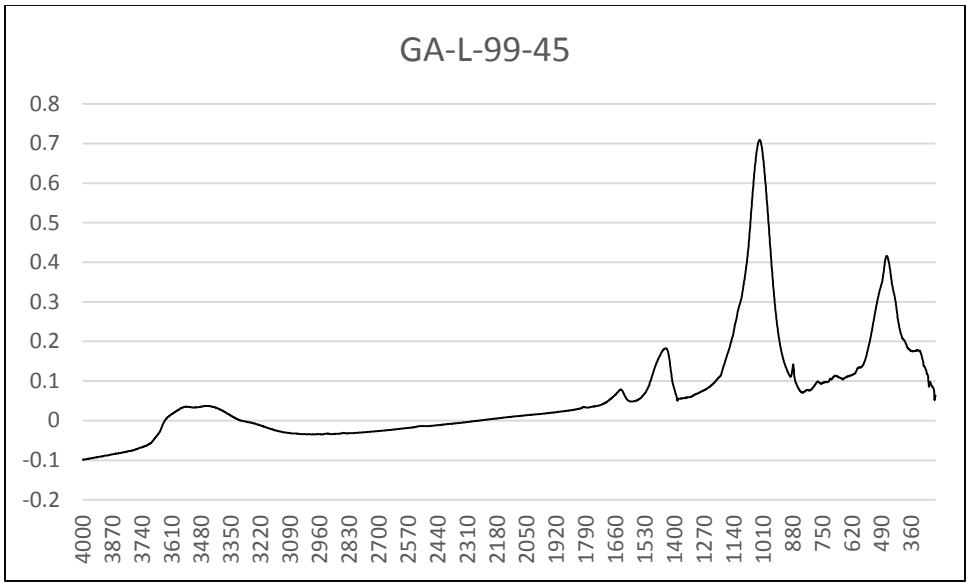

GA-L-99-45 FTIR Infrared Spectra

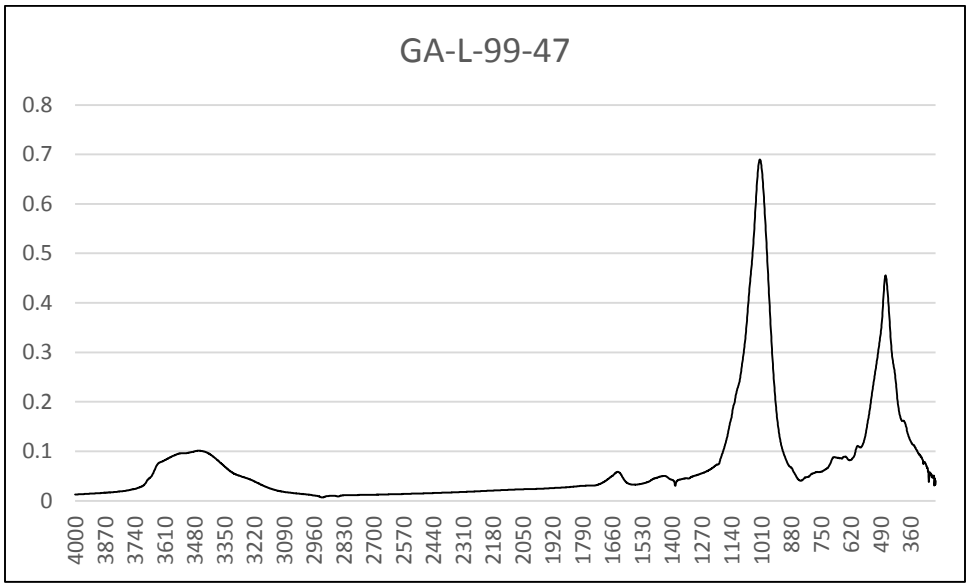

GA-L-99-47 FTIR Infrared Spectra

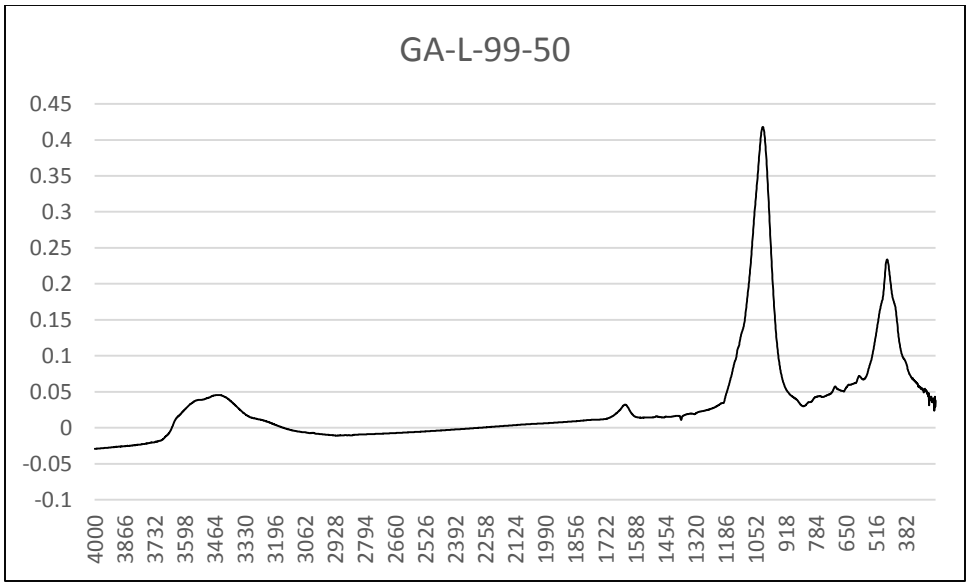

GA-L-99-50 FTIR Infrared Spectra

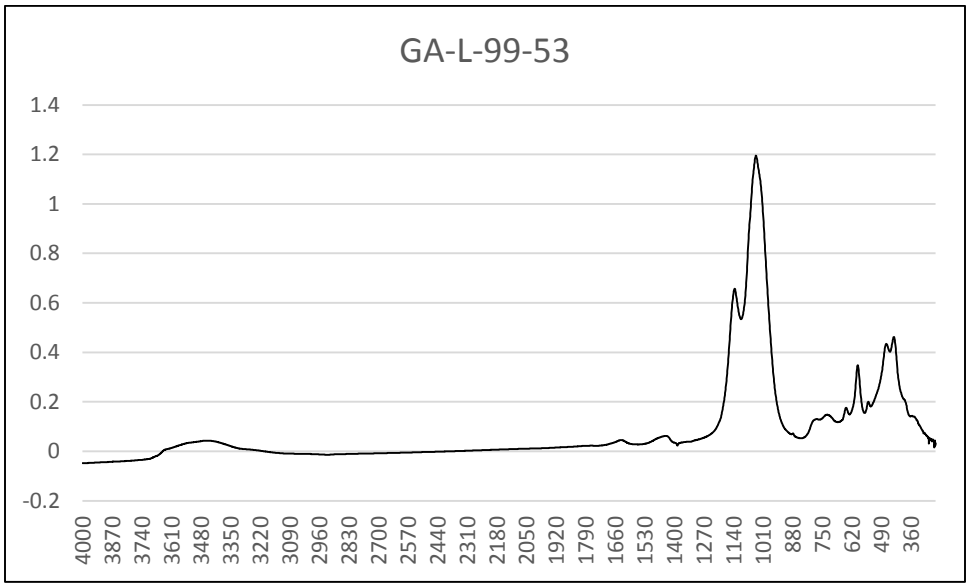

GA-L-99-53 FTIR Infrared Spectra

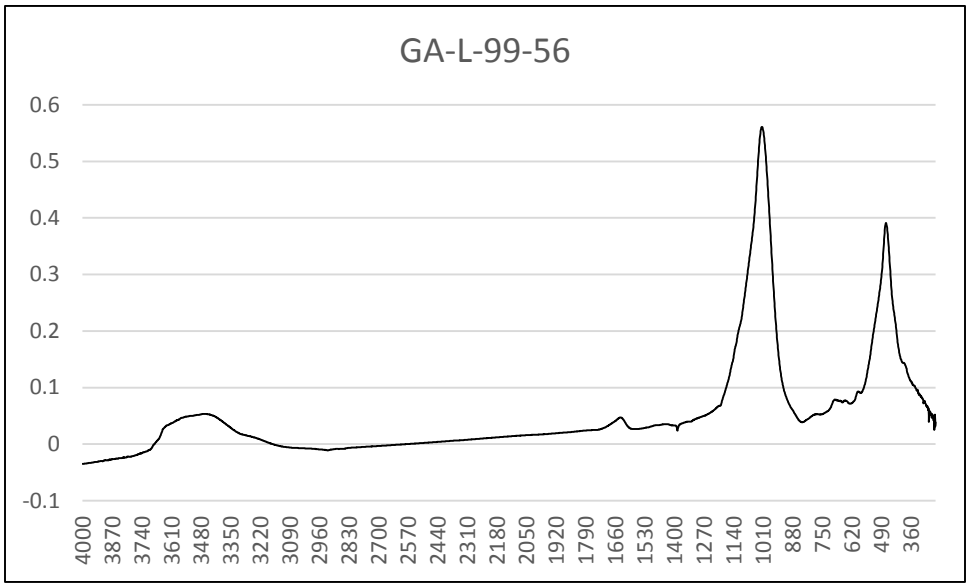

GA-L-99-56 FTIR Infrared Spectra

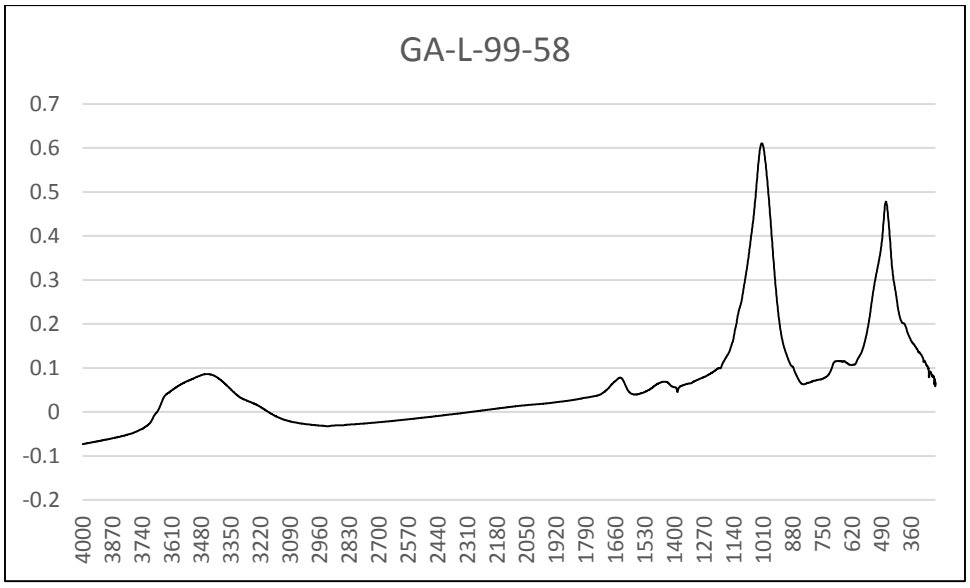

GA-L-99-58 FTIR Infrared Spectra

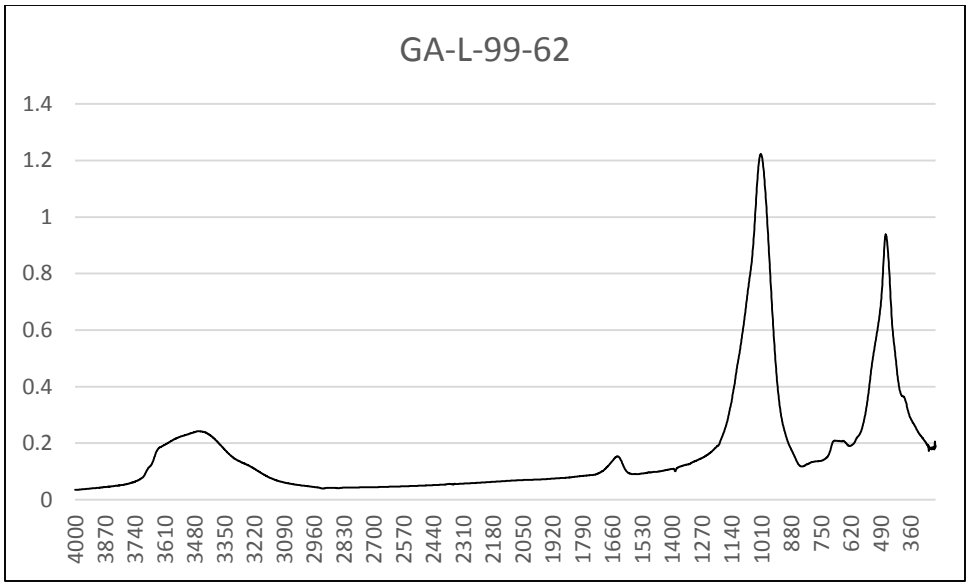

GA-L-99-62 FTIR Infrared Spectra

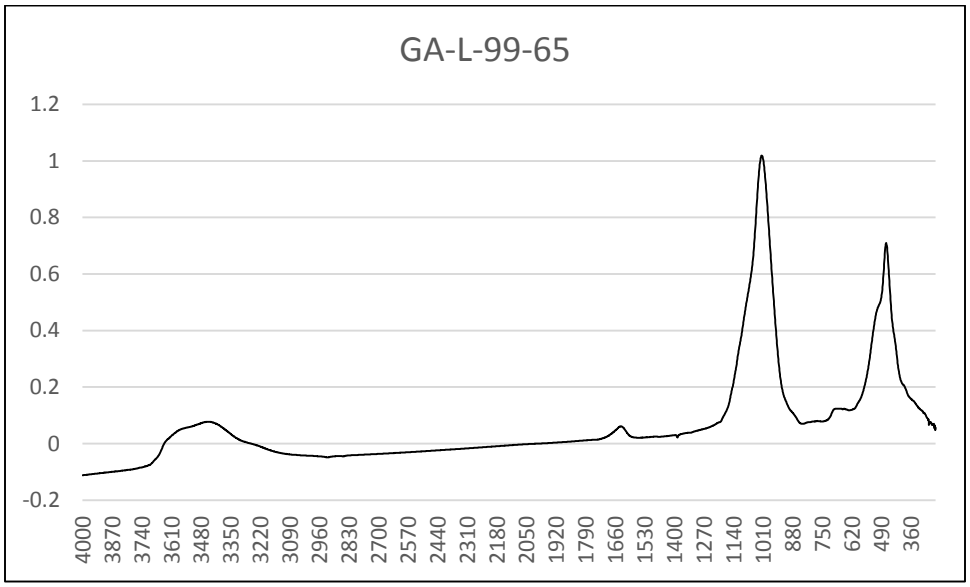

GA-L-99-65 FTIR Infrared Spectra

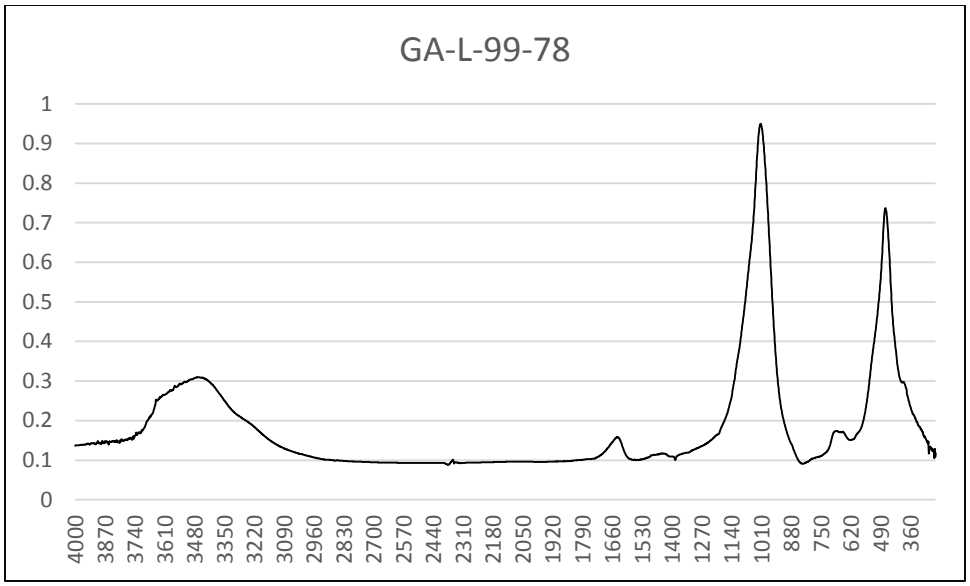

GA-L-99-78 FTIR Infrared Spectra

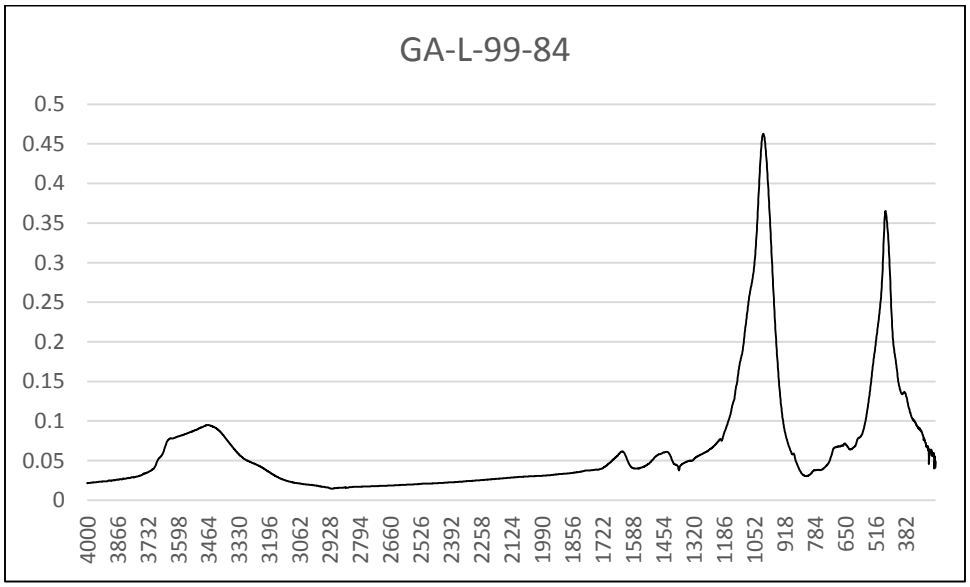

GA-L-99-84 FTIR Infrared Spectra

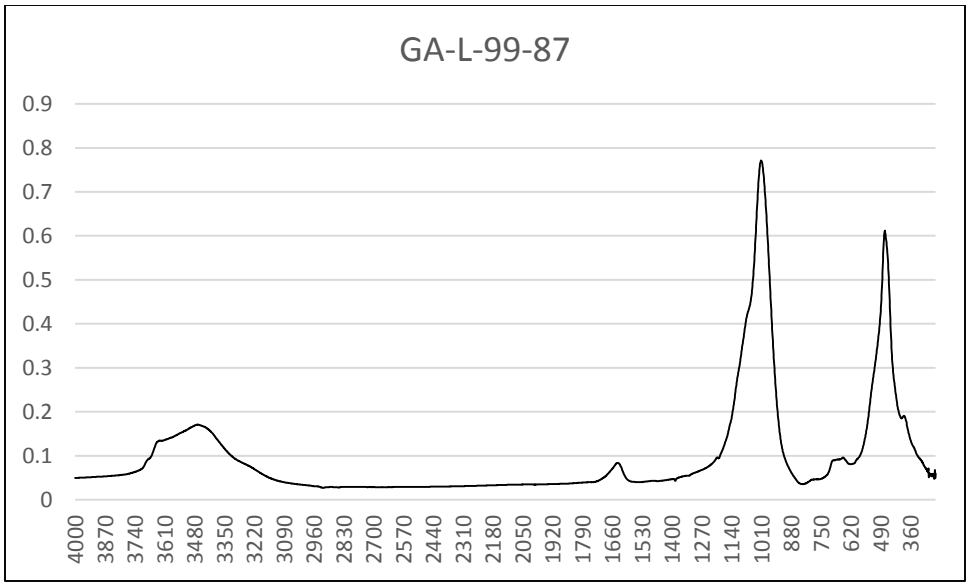

GA-L-99-87 FTIR Infrared Spectra

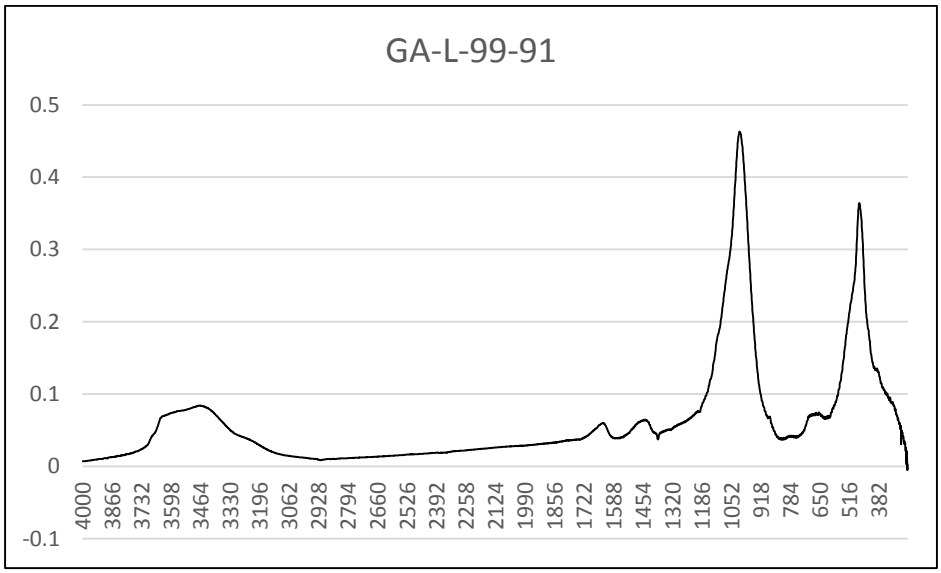

GA-L-99-91 FTIR Infrared Spectra

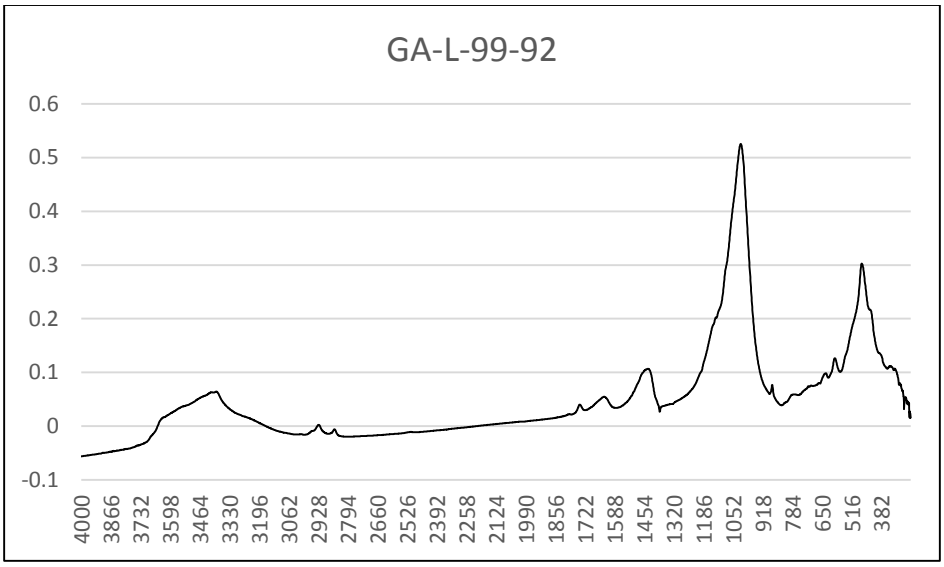

GA-L-99-92 FTIR Infrared Spectra

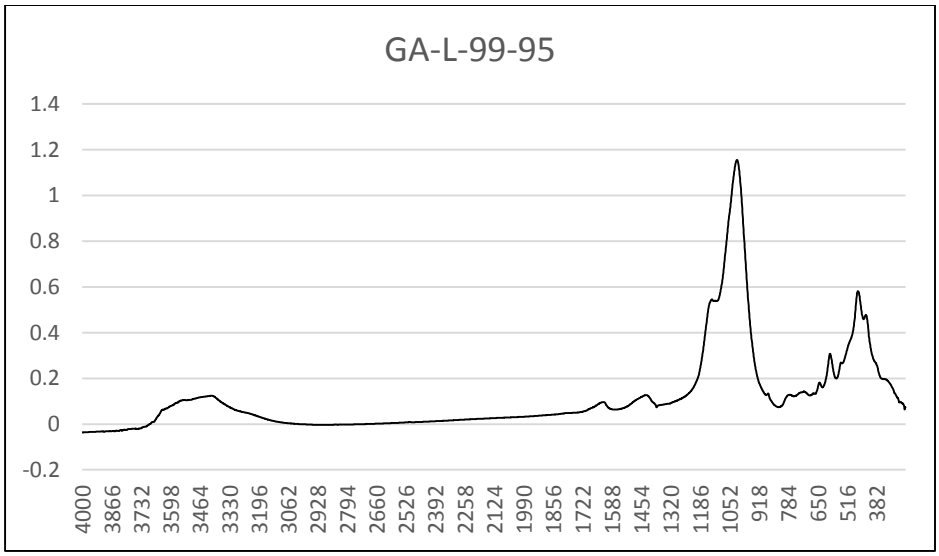

GA-L-99-95 FTIR Infrared Spectra

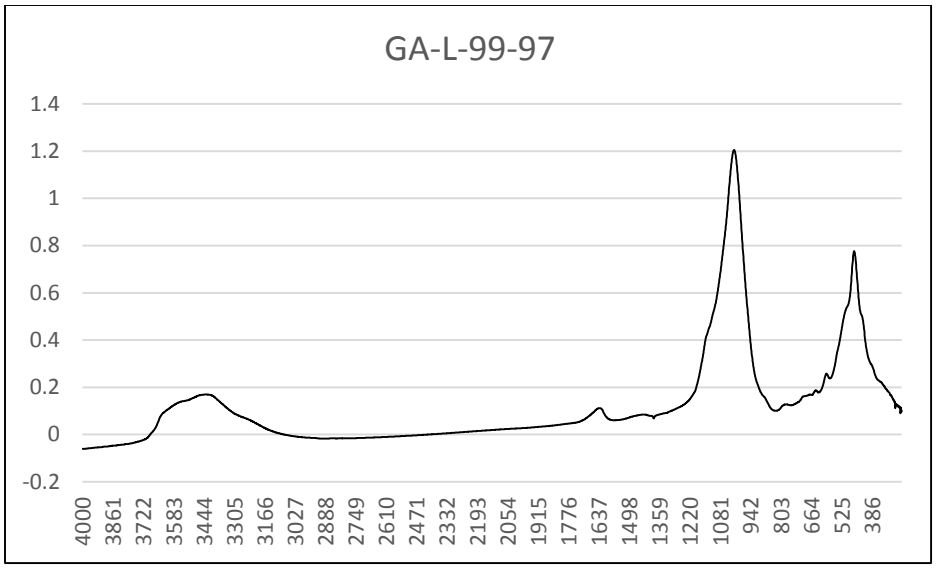

GA-L-99-97 FTIR Infrared Spectra

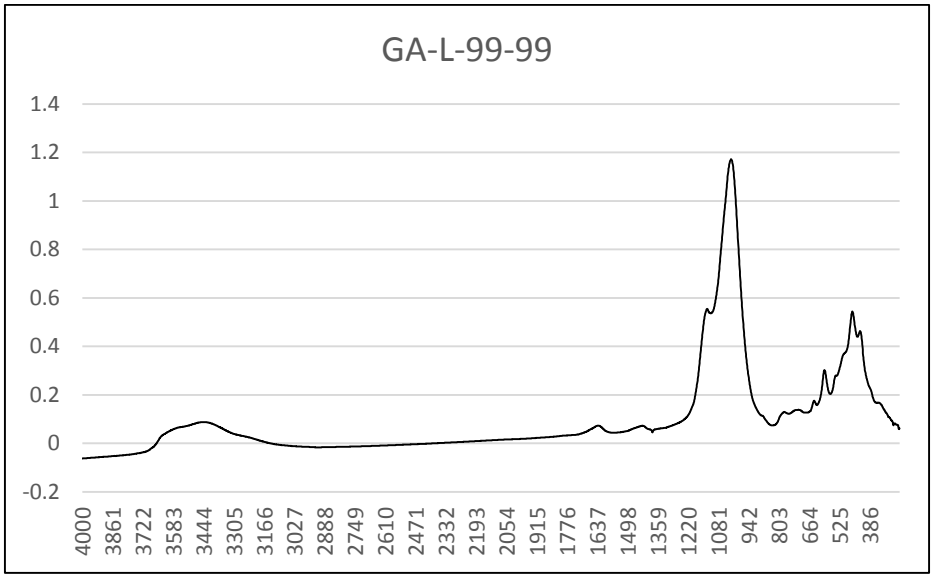

GA-L-99-99 FTIR Infrared Spectra

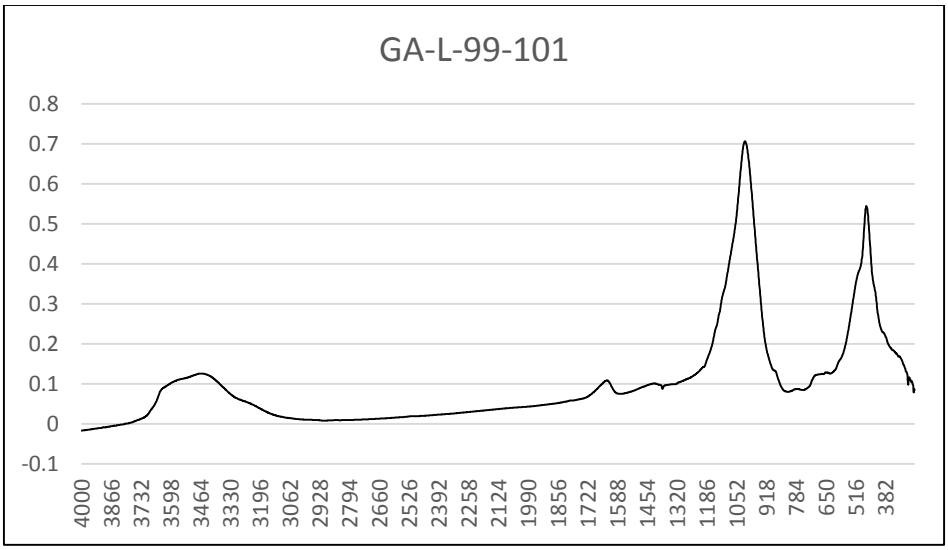

GA-L-99-101 FTIR Infrared Spectra

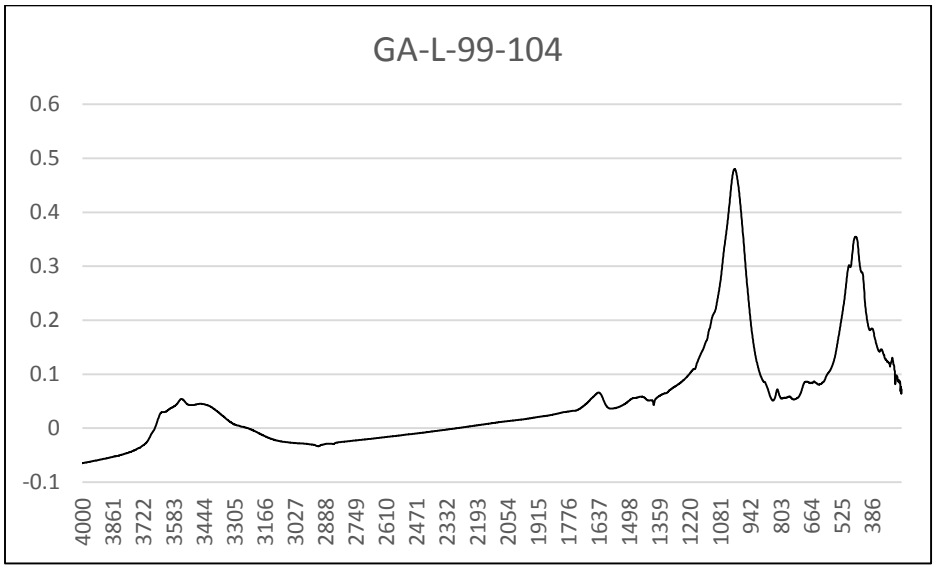

GA-L-99-104 FTIR Infrared Spectra

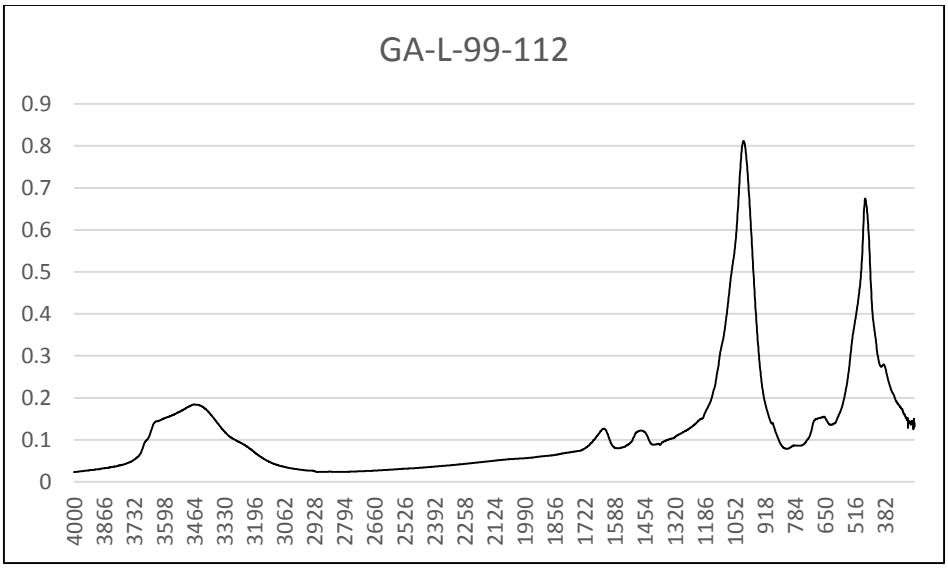

GA-L-99-112 FTIR Infrared Spectra

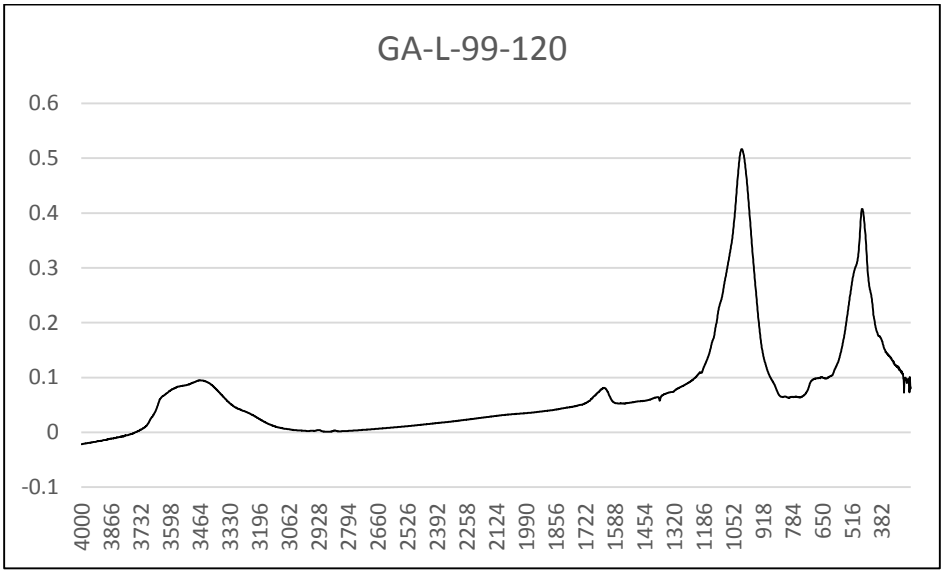

GA-L-99-120 FTIR Infrared Spectra

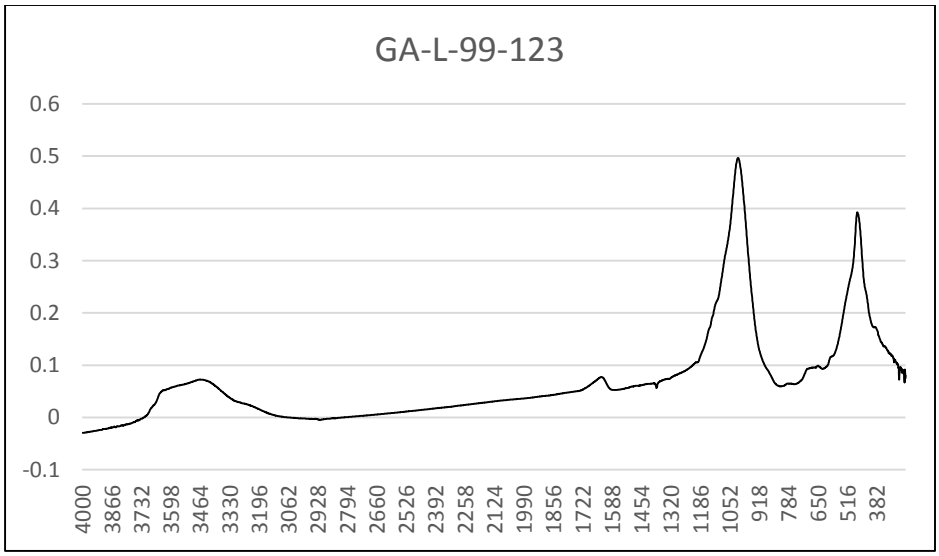

GA-L-99-123 FTIR Infrared Spectra

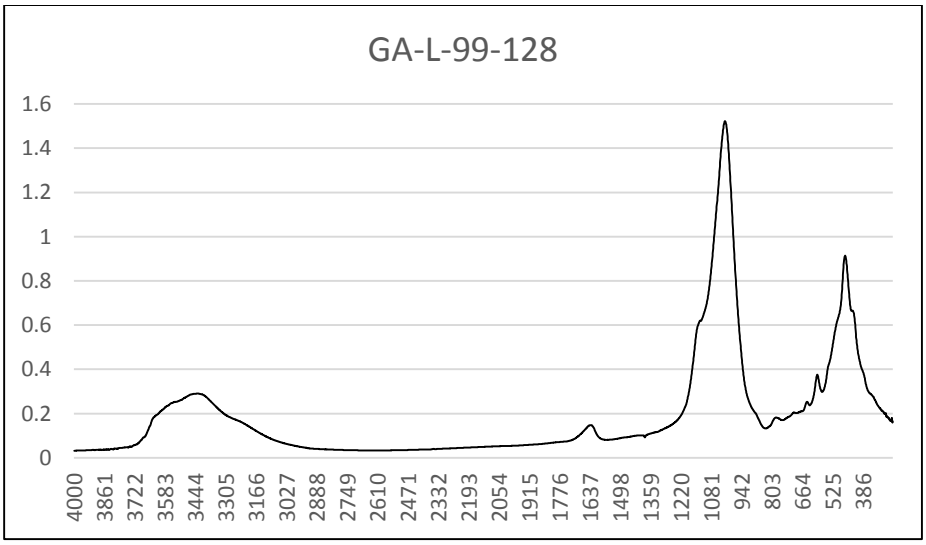

GA-L-99-128 FTIR Infrared Spectra

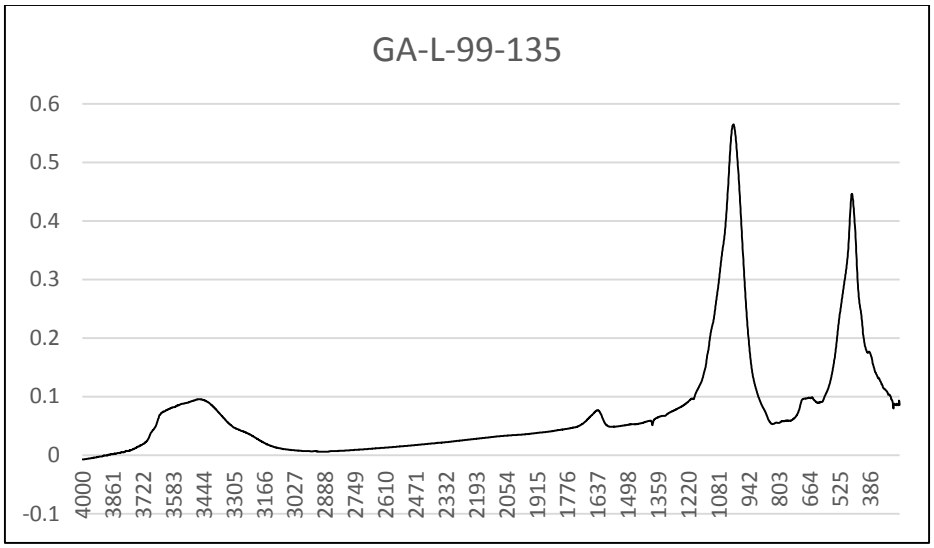

GA-L-99-135 FTIR Infrared Spectra

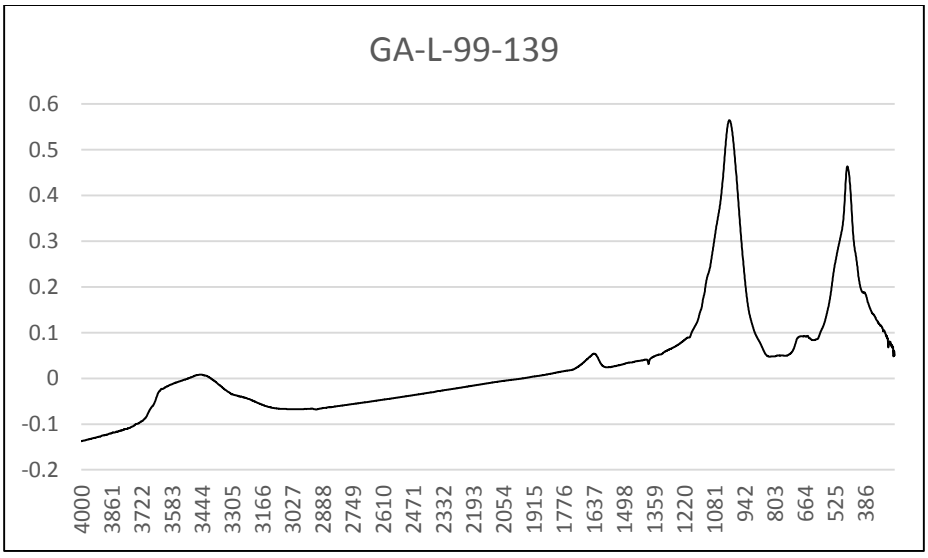

GA-L-99-139 FTIR Infrared Spectra

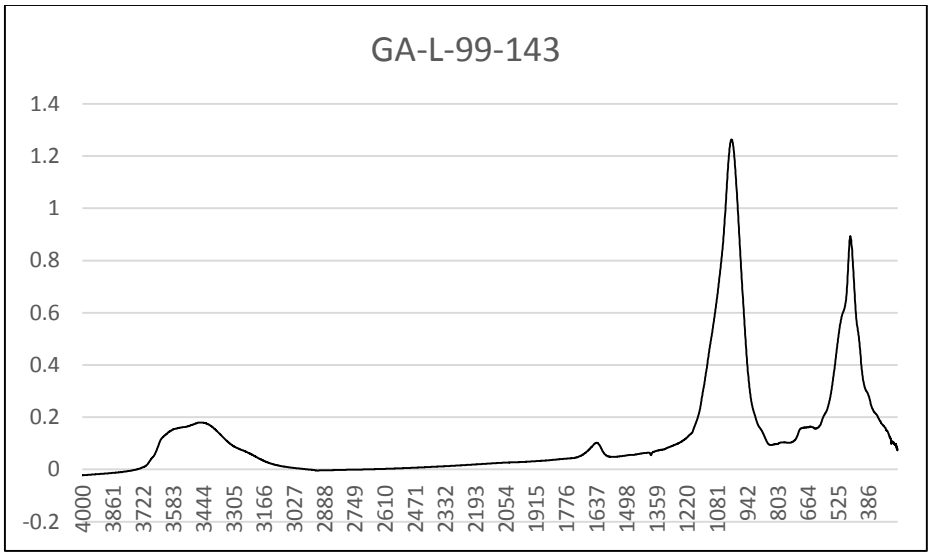

GA-L-99-143 FTIR Infrared Spectra

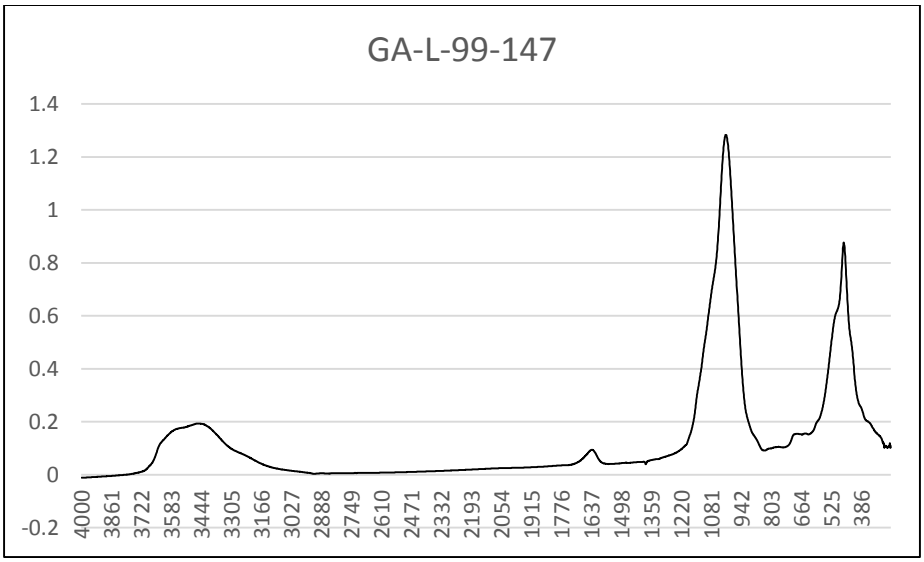

GA-L-99-147 FTIR Infrared Spectra

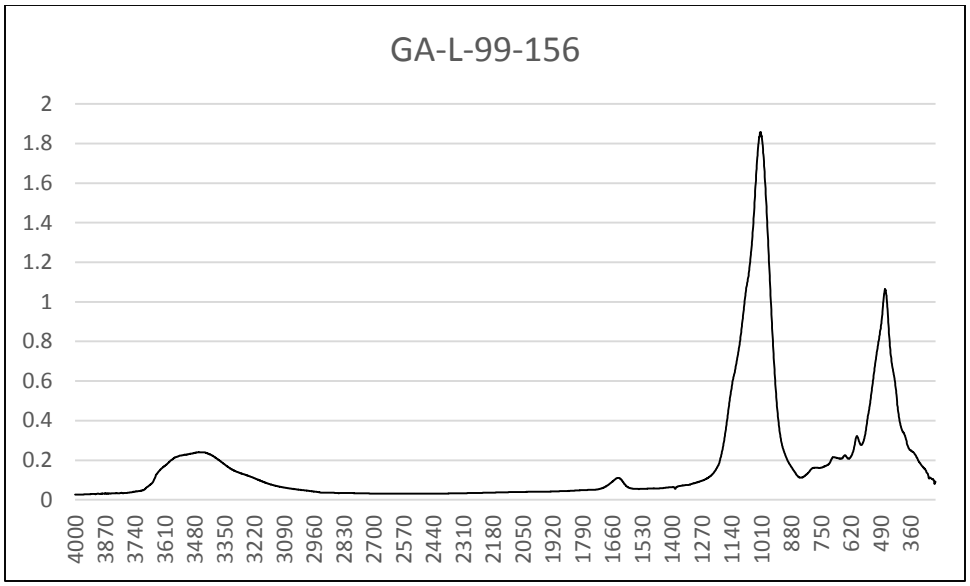

GA-L-99-156 FTIR Infrared Spectra

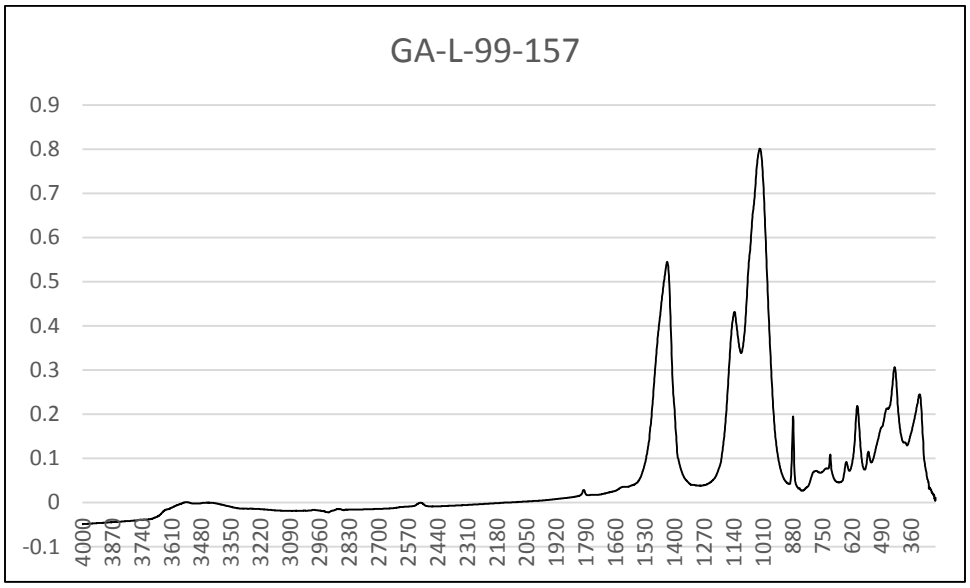

GA-L-99-157 FTIR Infrared Spectra

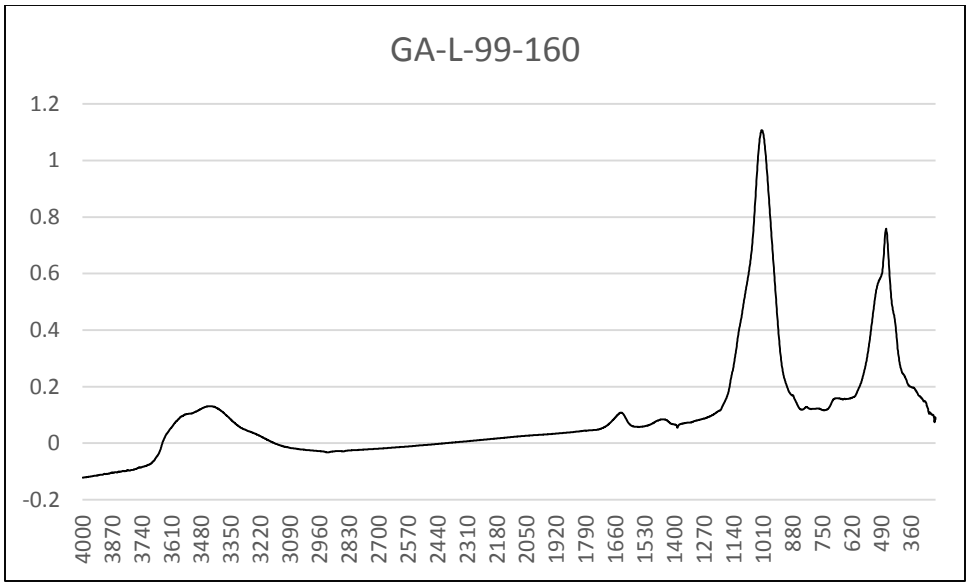

GA-L-99-160 FTIR Infrared Spectra

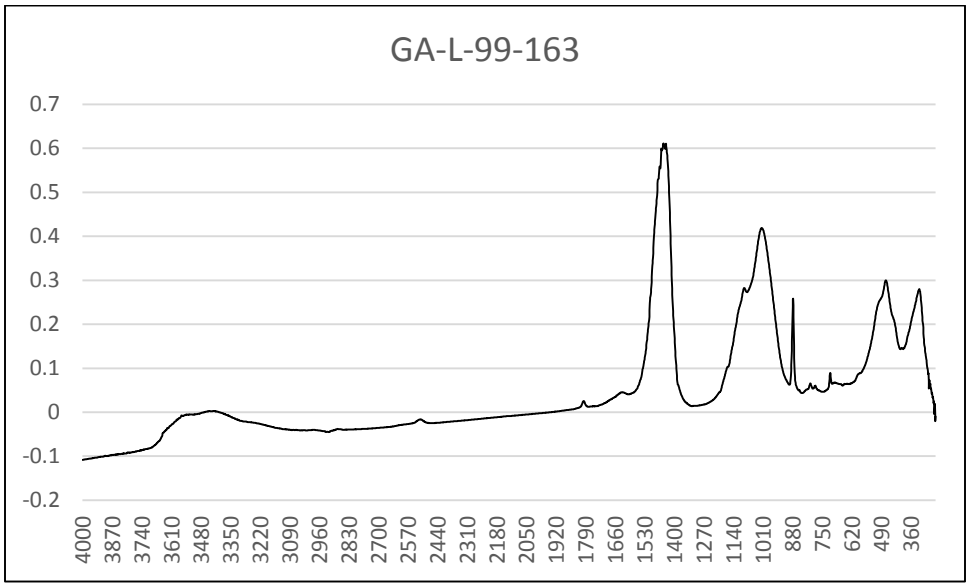

GA-L-99-163 FTIR Infrared Spectra

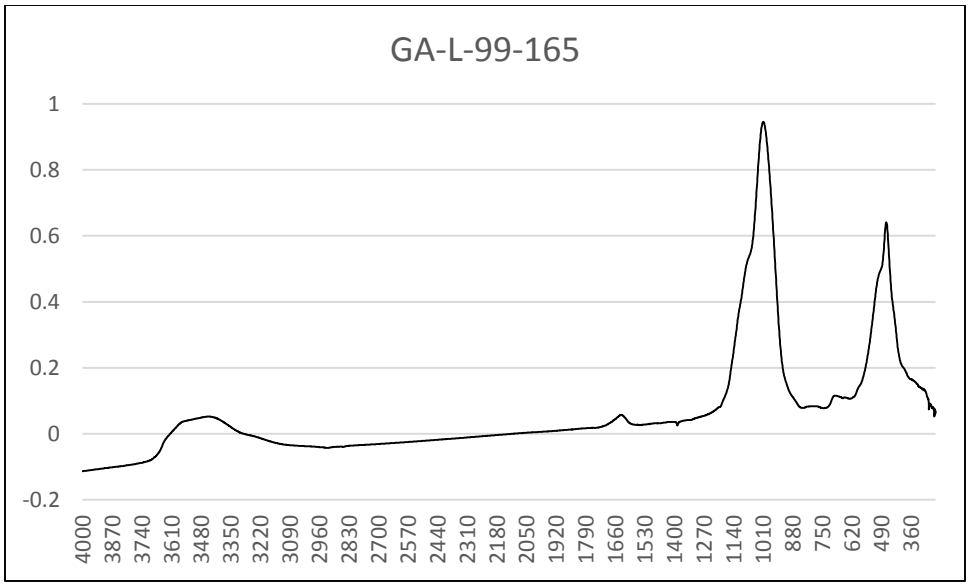

GA-L-99-165 FTIR Infrared Spectra

Appendix C: XRD Diffractograms

A

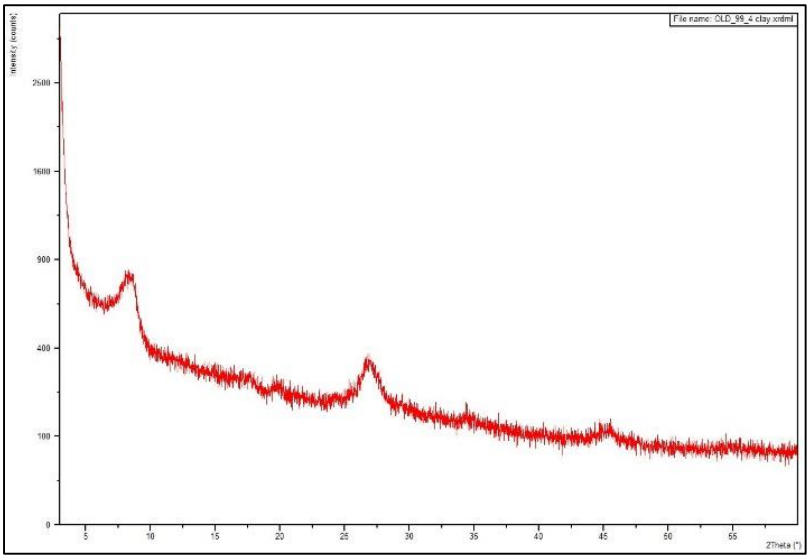

B

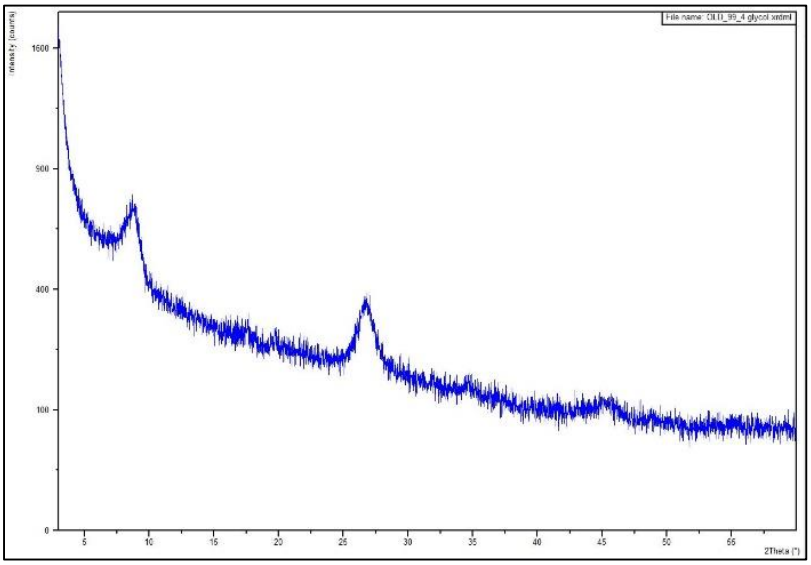

GA-L-99-4 XRD Diffractograms, air-dried (A) and glycolated (B)

A

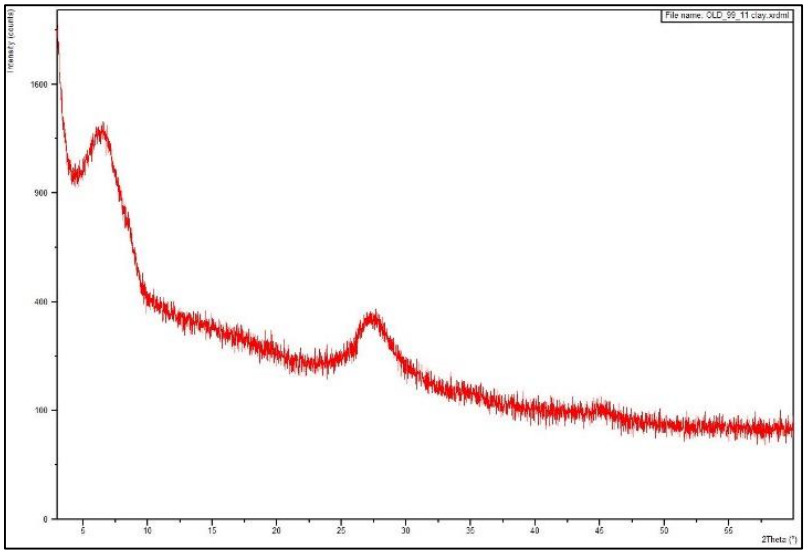

B

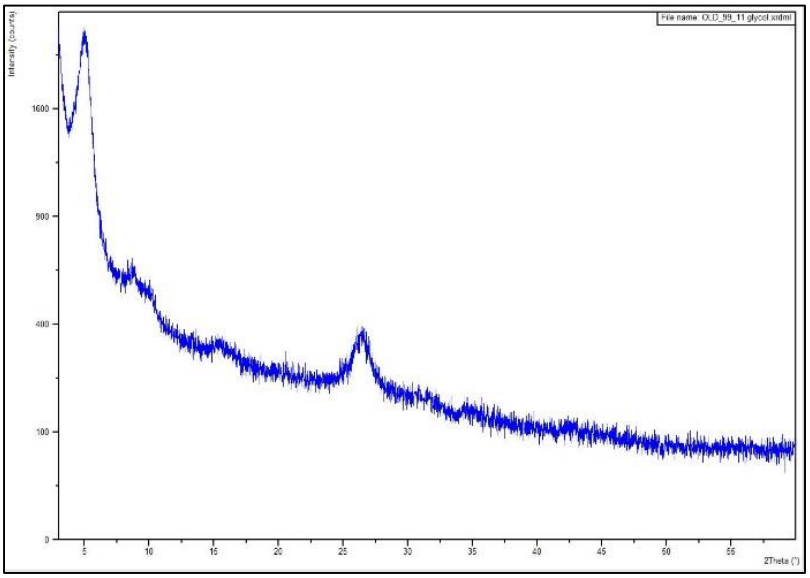

GA-L-99-11 XRD Diffractograms; air-dried (A) and glycolated (B)

A

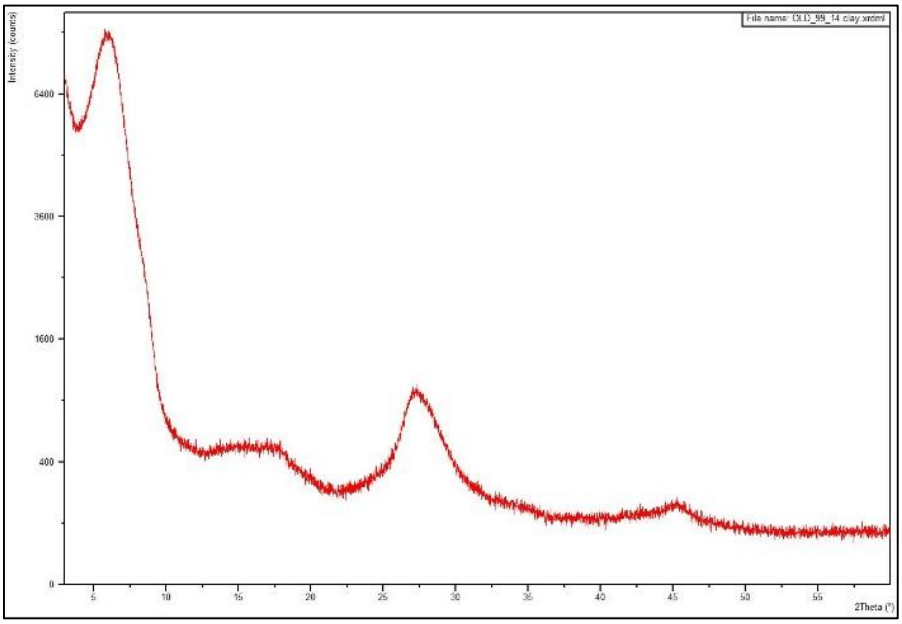

B

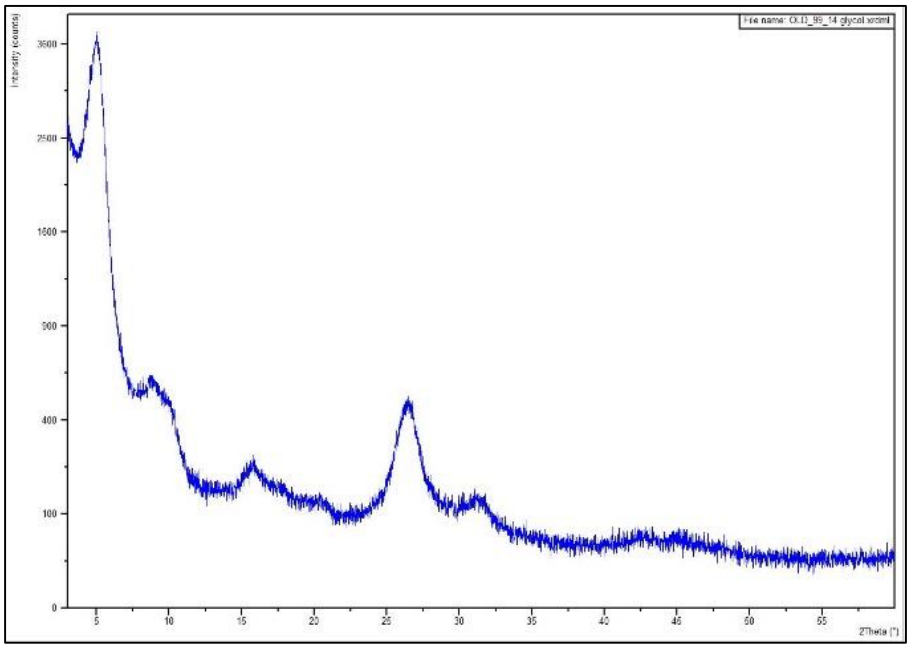

GA-L-99-14 XRD Diffractograms; air-dried (A) and glycolated (B)

A

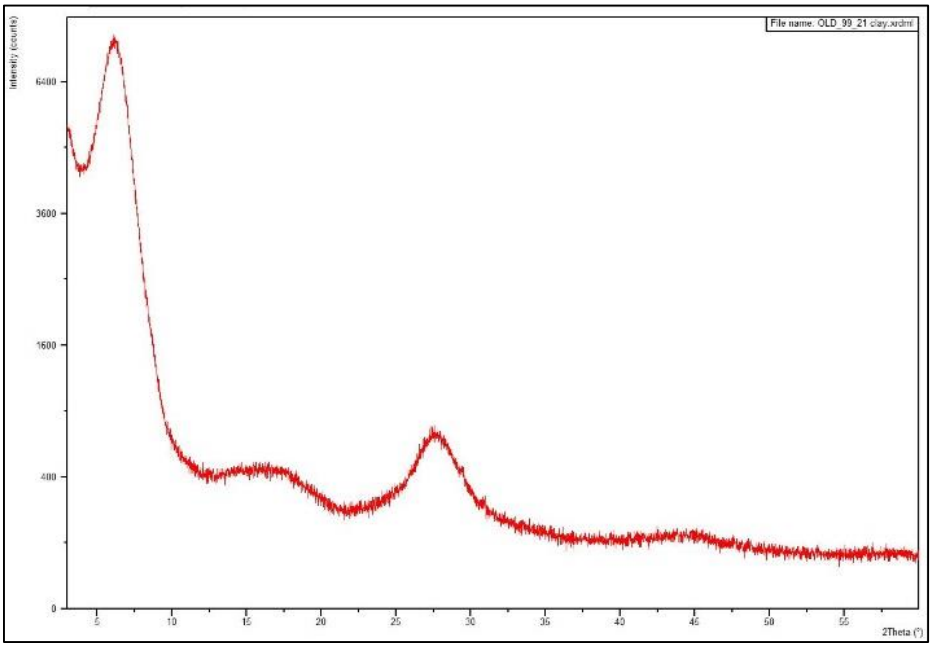

B

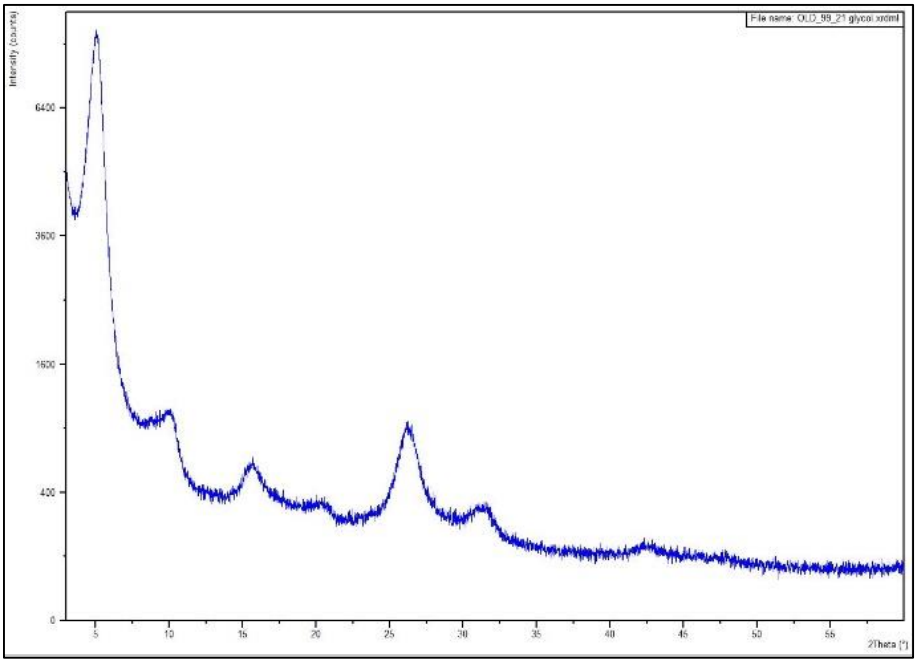

GA-L-99-21 XRD Diffractograms; air-dried (A) and glycolated (B)

A

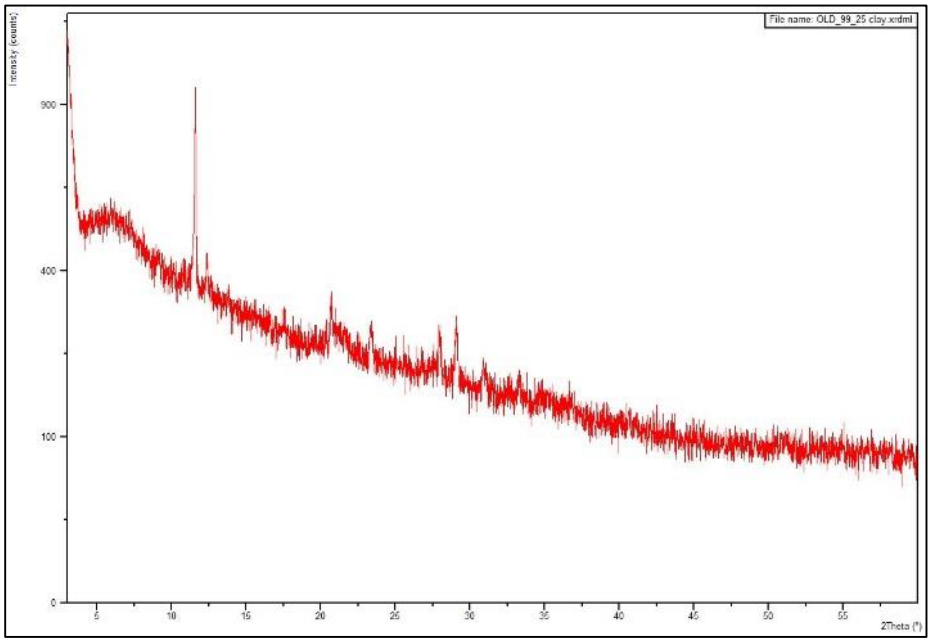

B

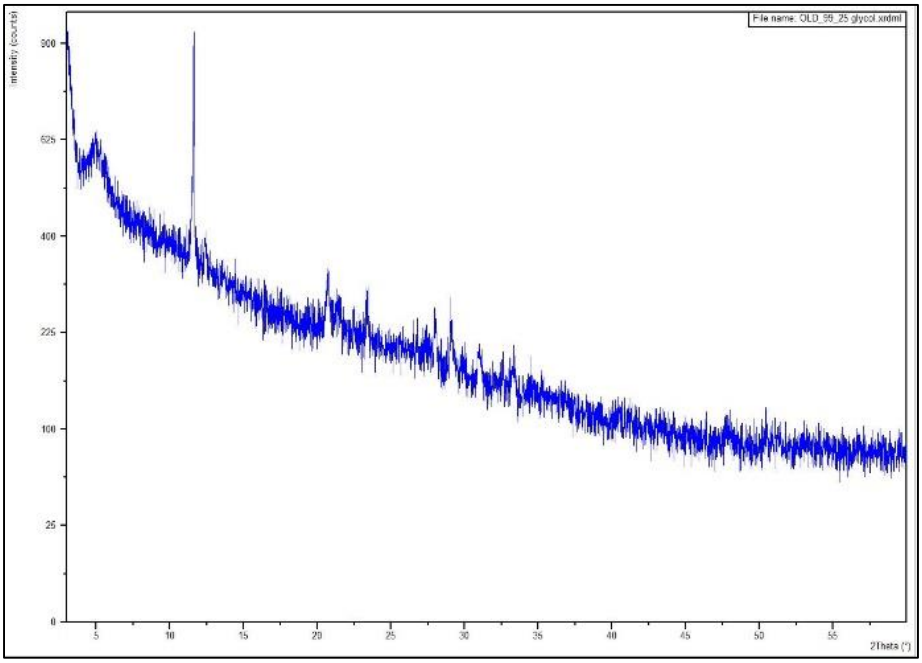

GA-L-99-25 XRD Diffractograms; air-dried (A) and glycolated (B)

A

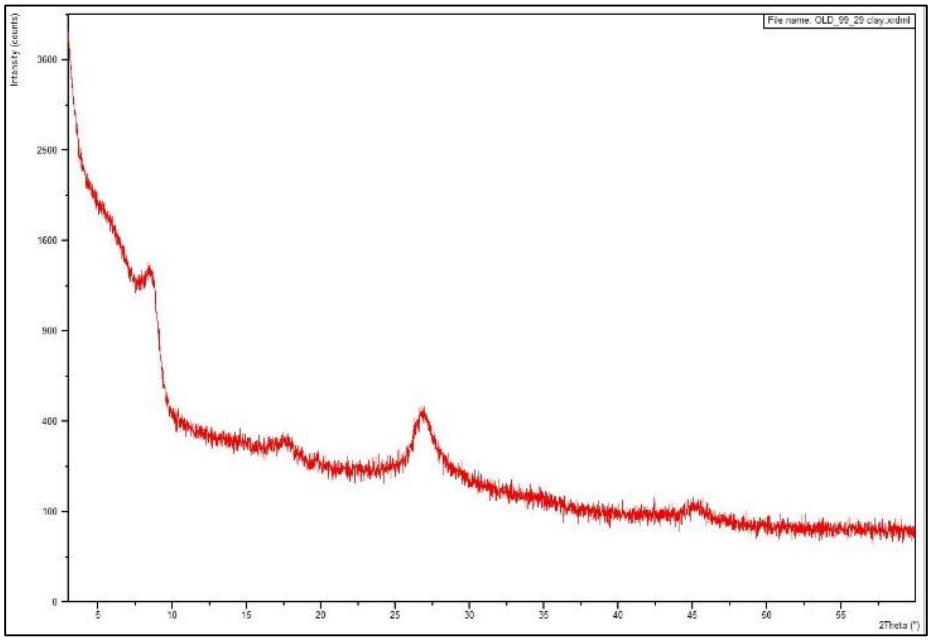

B

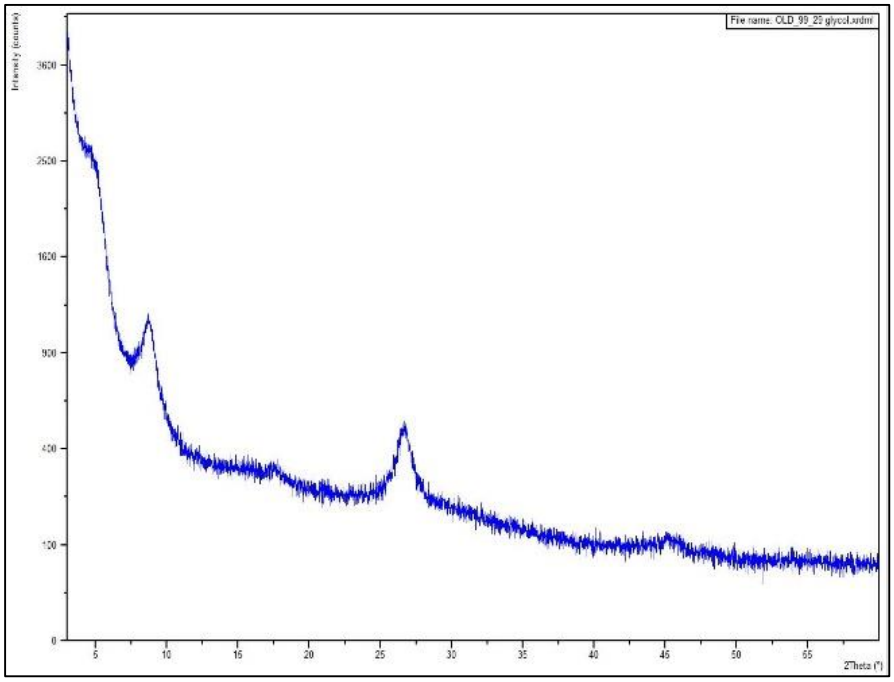

GA-L-99-29 XRD Diffractograms; air-dried (A) and glycolated (B)

A

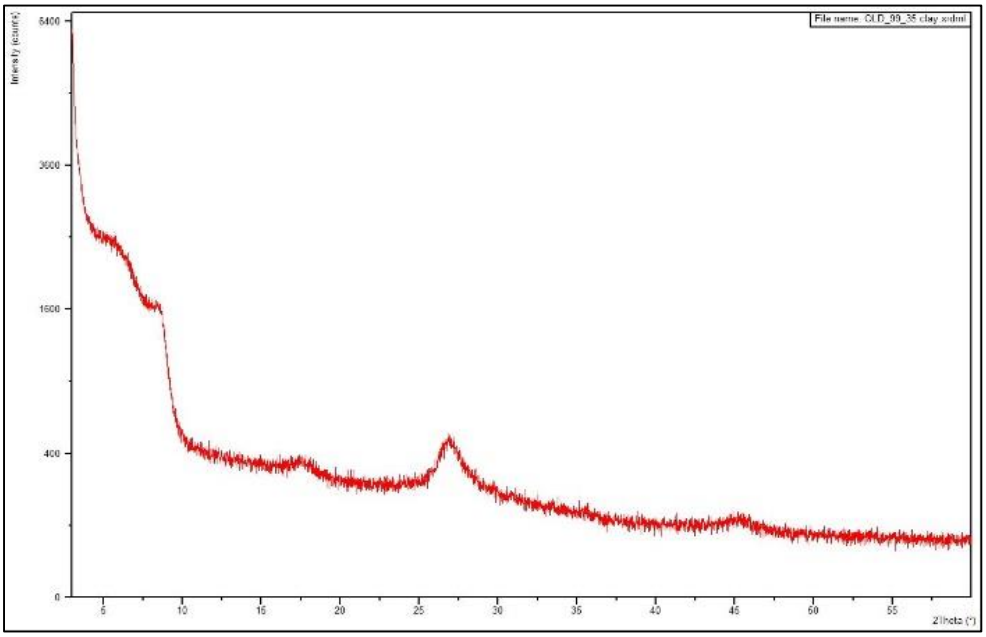

B

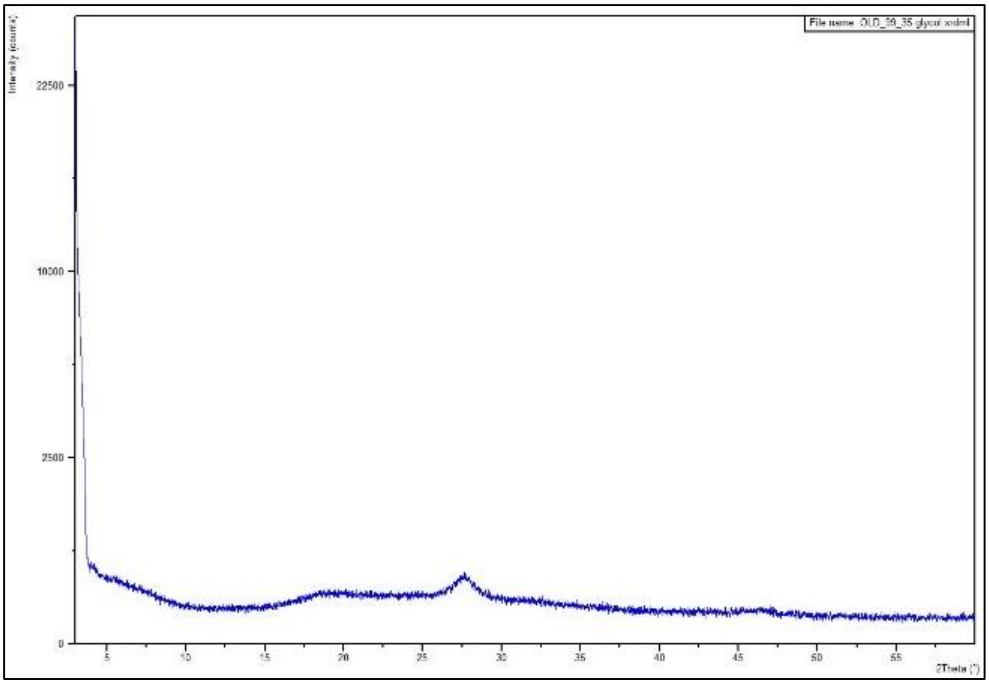

GA-L-99-35 XRD Diffractograms; air-dried (A) and glycolated (B)

A

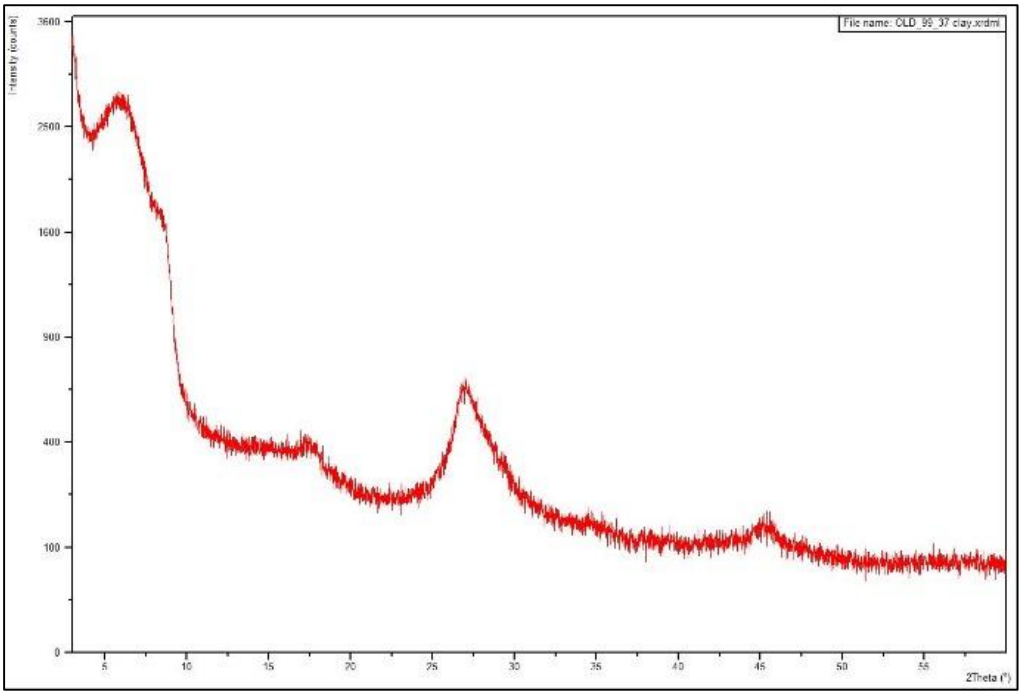

B

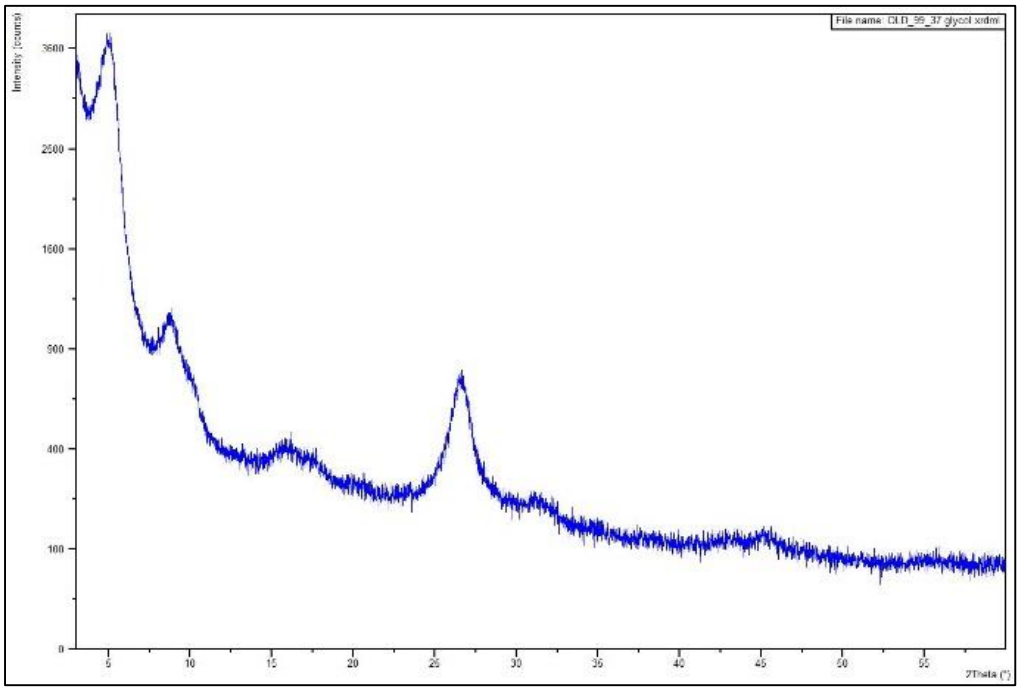

GA-L-99-37 XRD Diffractograms; air-dried (A) and glycolated (B)

A

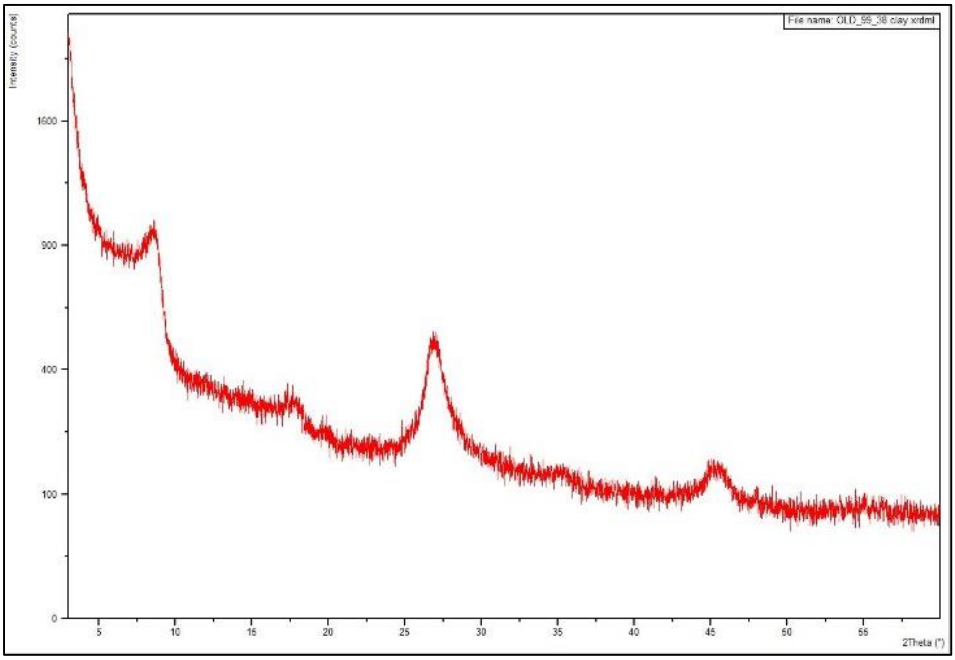
File name: OLD_99_38 clay.xrdml
Intensity (counts)
1600
900
400
100
0
5
10
15
20
25
30
35
40
45
50
55
2Theta (°)

B

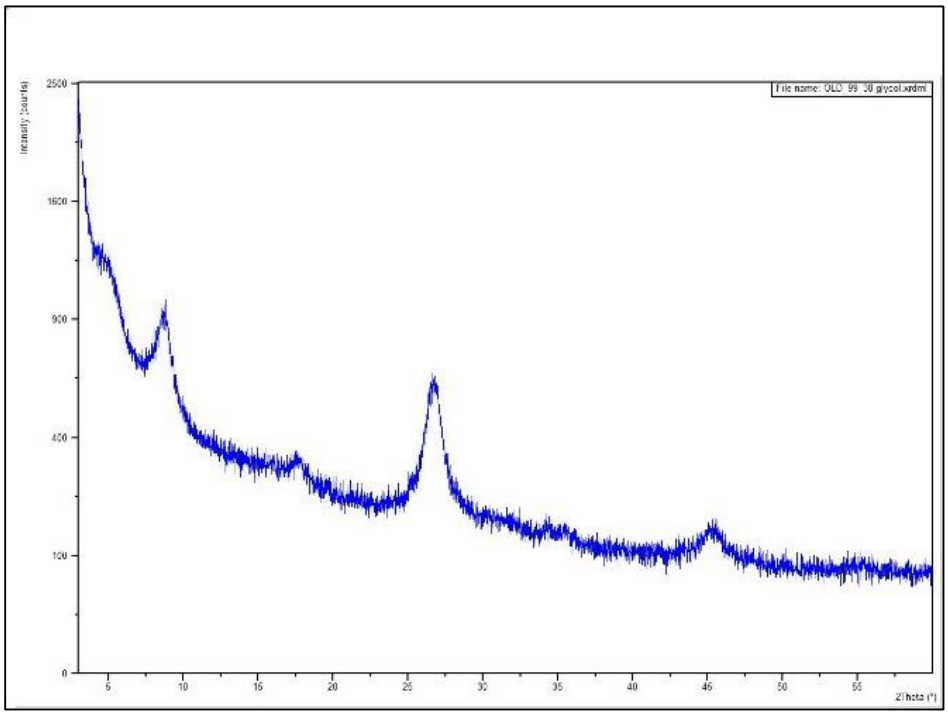
File name: OLD_99_38 glycol.xrdml
Intensity (counts)
2500
1600
900
400
100
0
5
10
15
20
25
30
35
40
45
50
55
2Theta (°)

GA-L-99-38 XRD Diffractograms; air-dried (A) and glycolated (B)

A

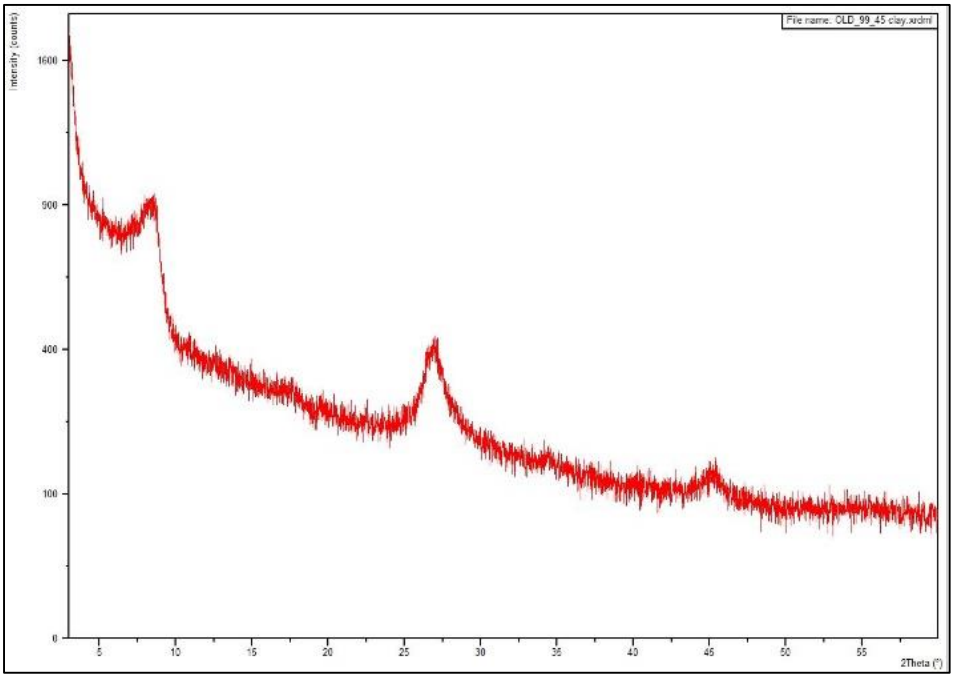

B

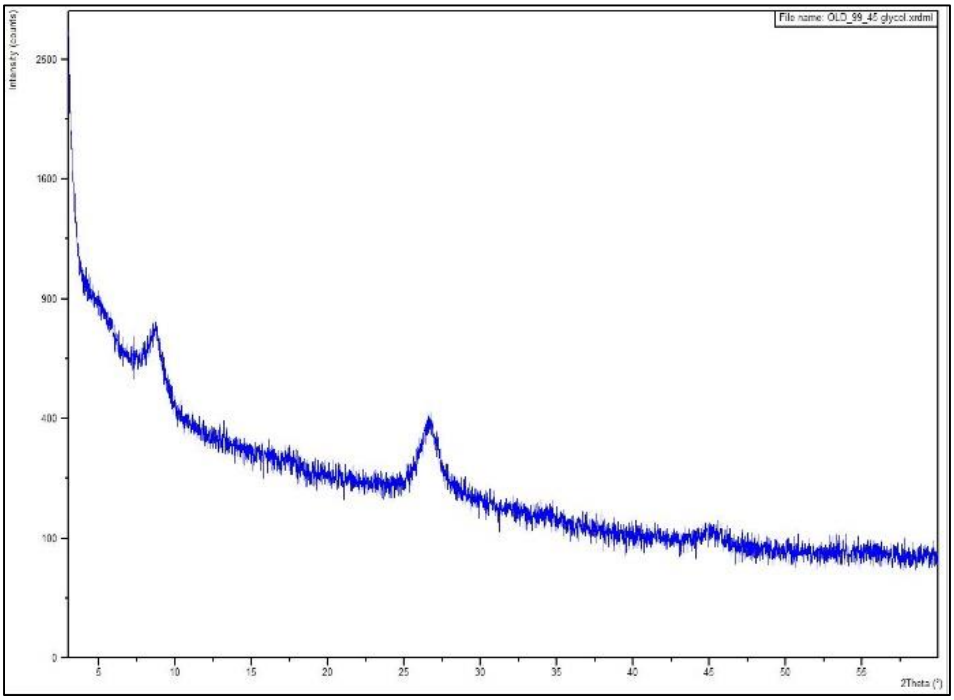

GA-L-99-45 XRD Diffractograms; air-dried (A) and glycolated (B)

A

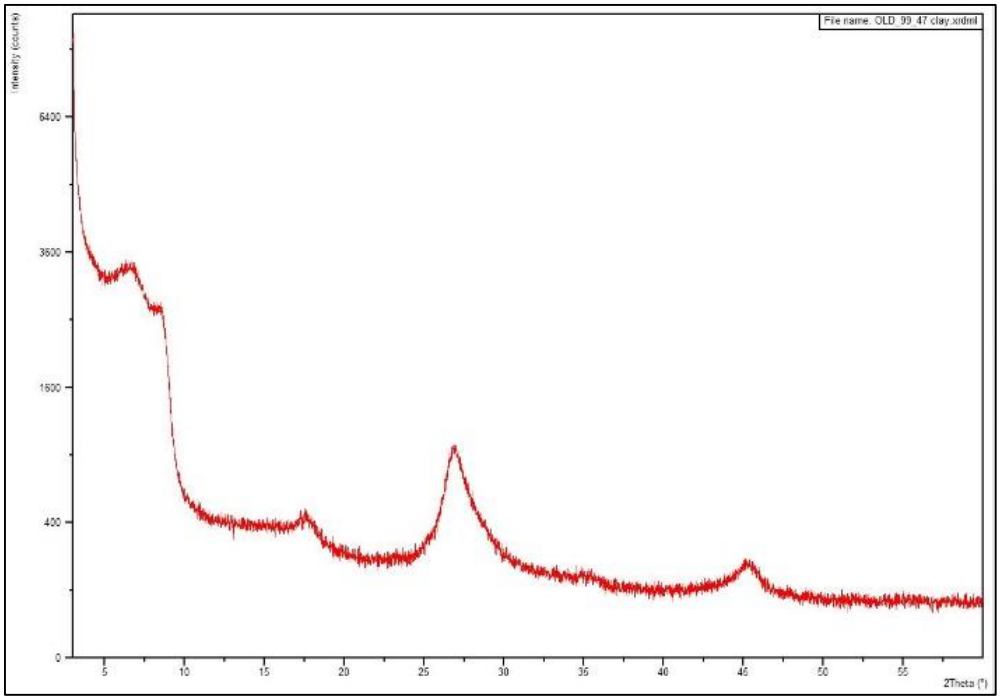

B

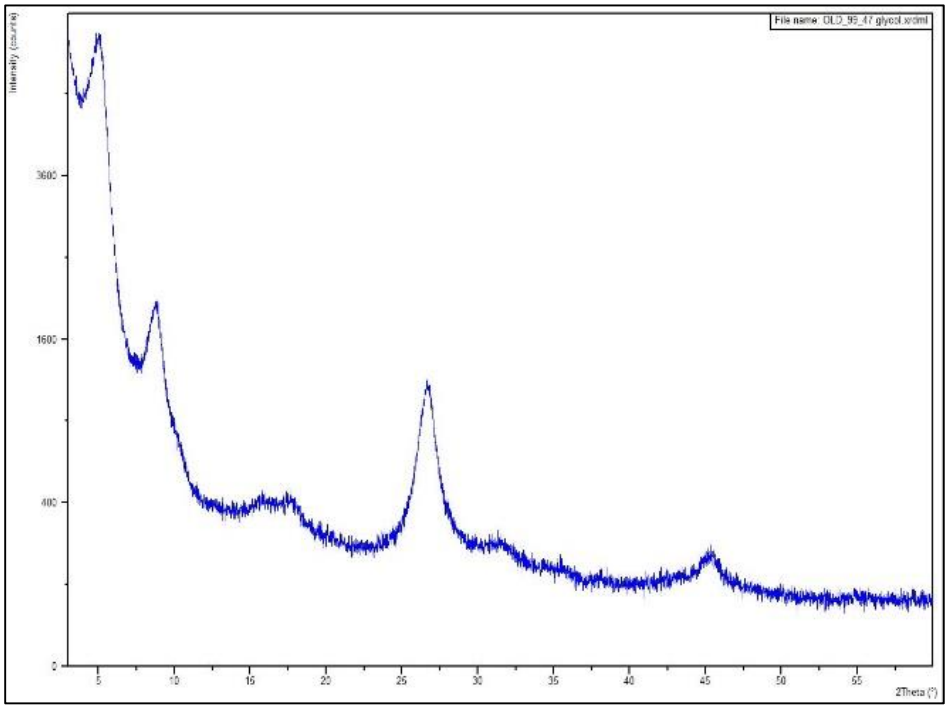

GA-L-99-47 XRD Diffractograms; air-dried (A) and glycolated (B)

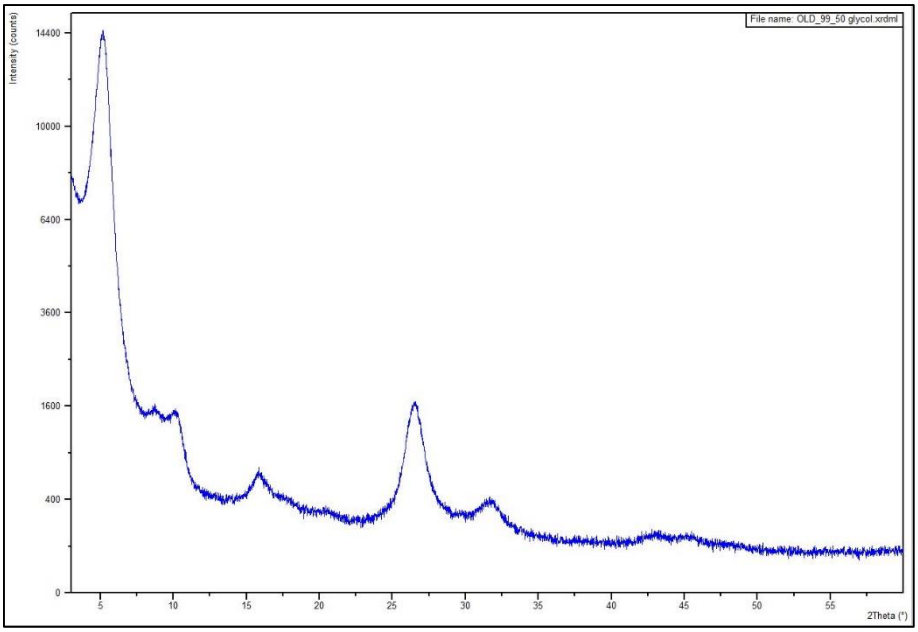

GA-L-99-50 XRD Diffractogram; glycolated

A

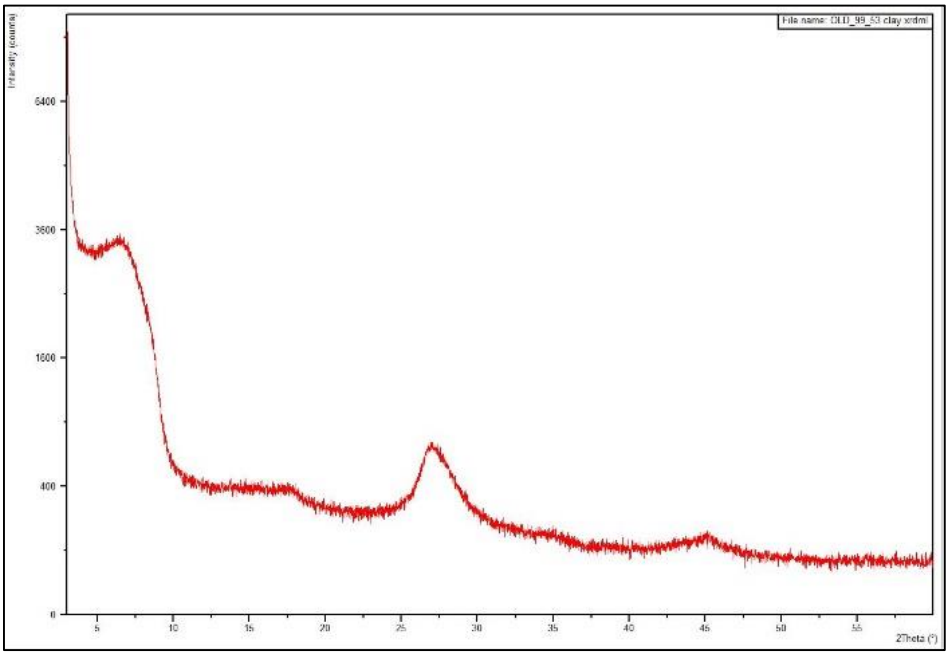
File name: OLD_99_53 clay.xrdml
Intensity (counts)
6400
3600
1600
400
0
5
10
15
20
25
30
35
40
45
50
55
2Theta (°)

B

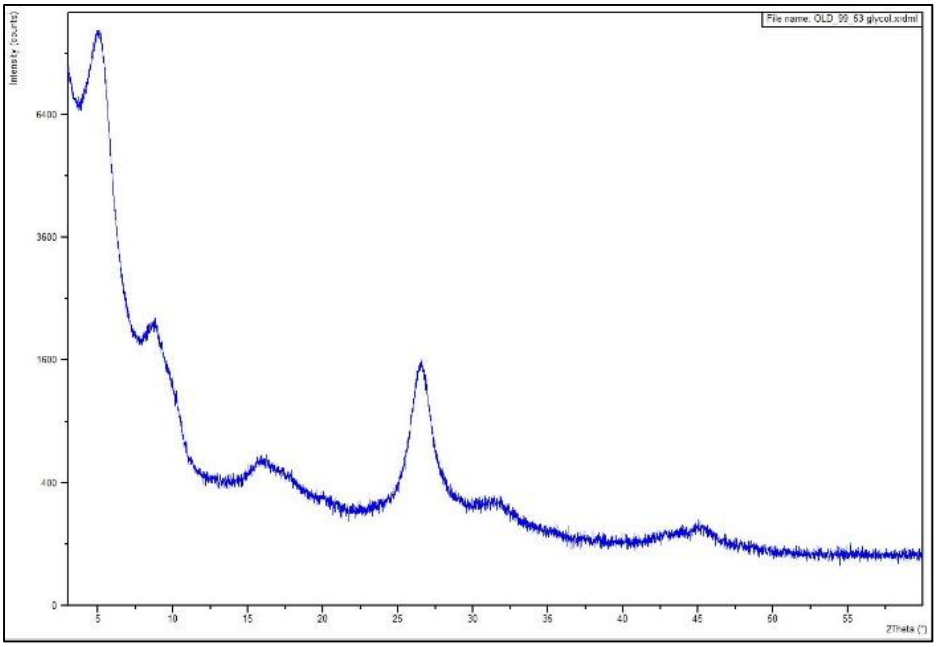
File name: OLD_99_53 glycol.xrdml
Intensity (counts)
6400
3600
1600
400
0
5
10
15
20
25
30
35
40
45
50
55
2Theta (°)

GA-L-99-53 XRD Diffractograms; air-dried (A) and glycolated (B)

A

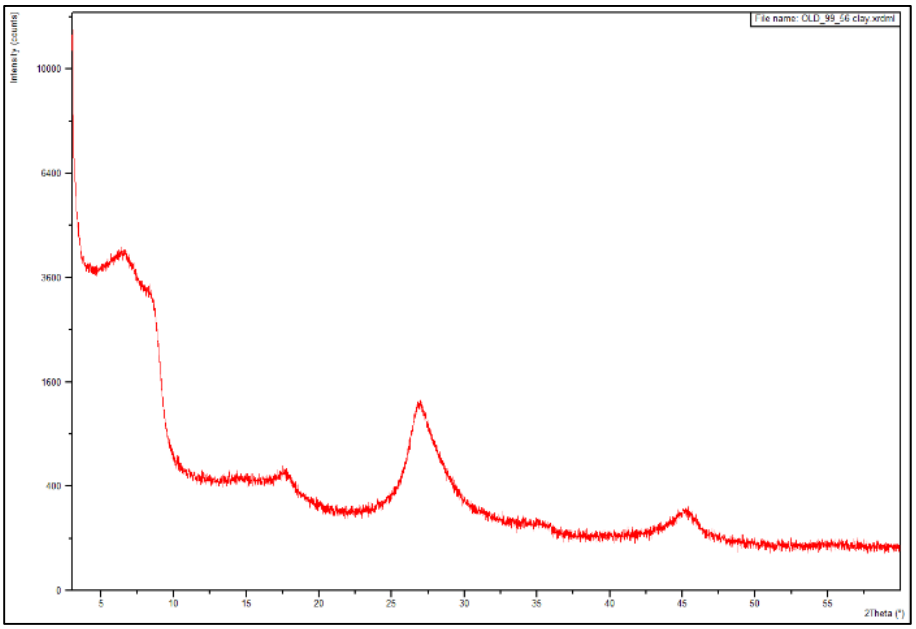

B

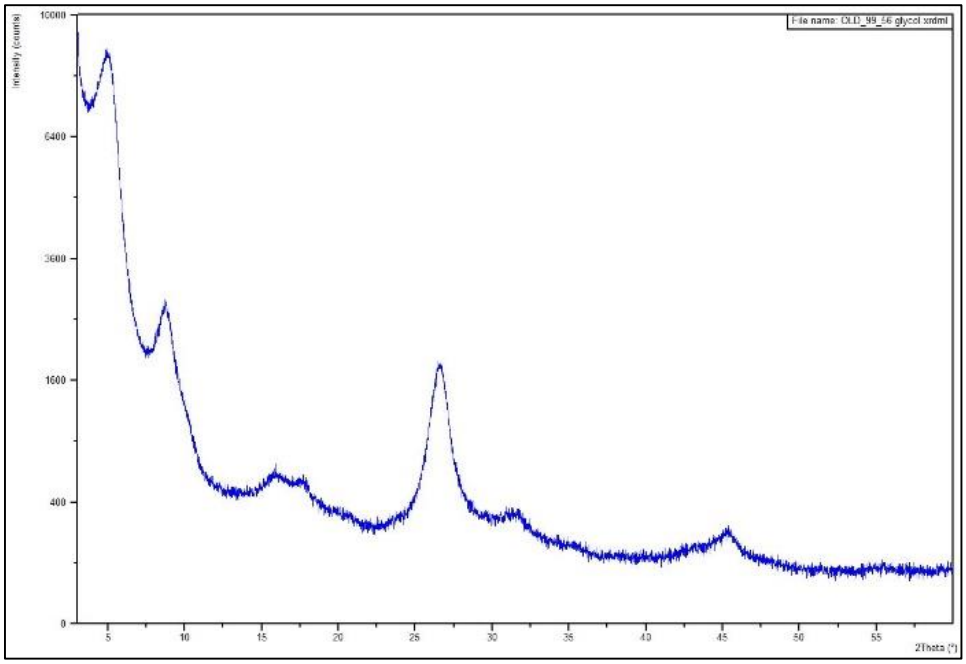

GA-L-99-56 XRD Diffractograms; air-dried (A) and glycolated (B)

A

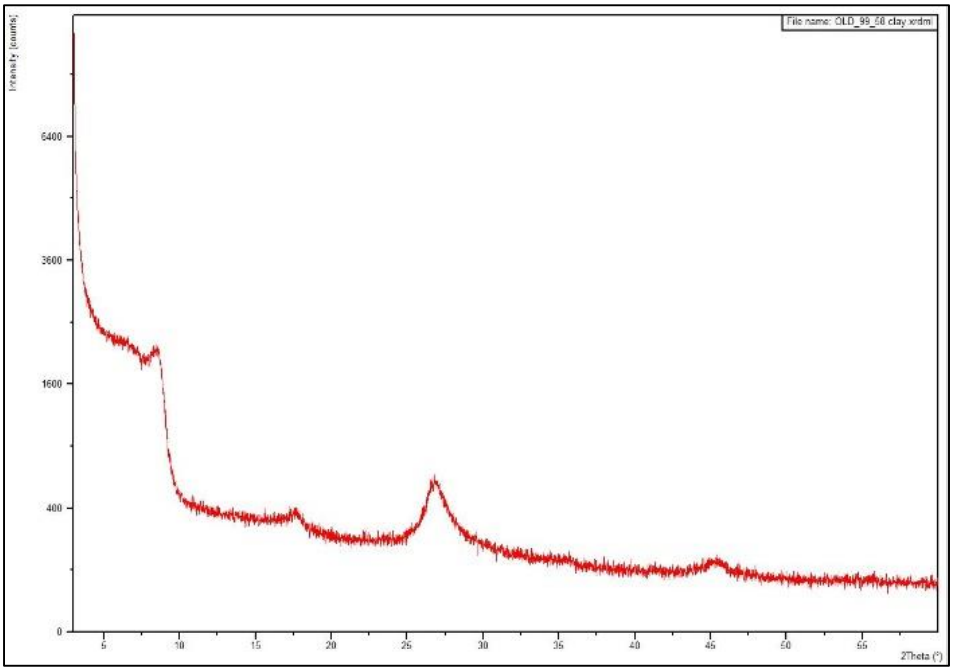

B

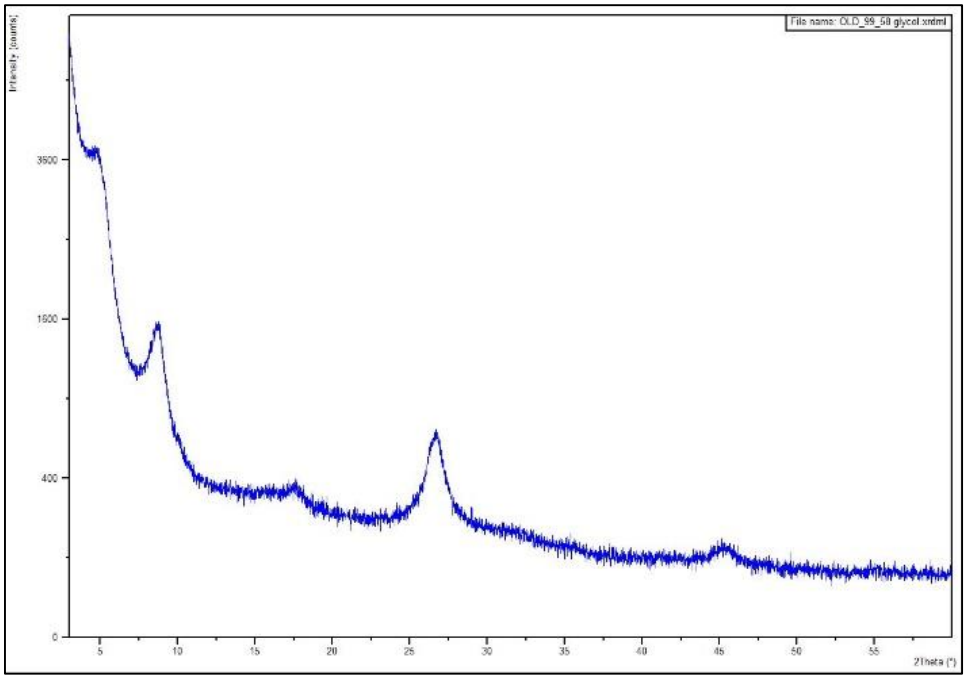

GA-L-99-58 XRD Diffractograms; air-dried (A) and glycolated (B)

A

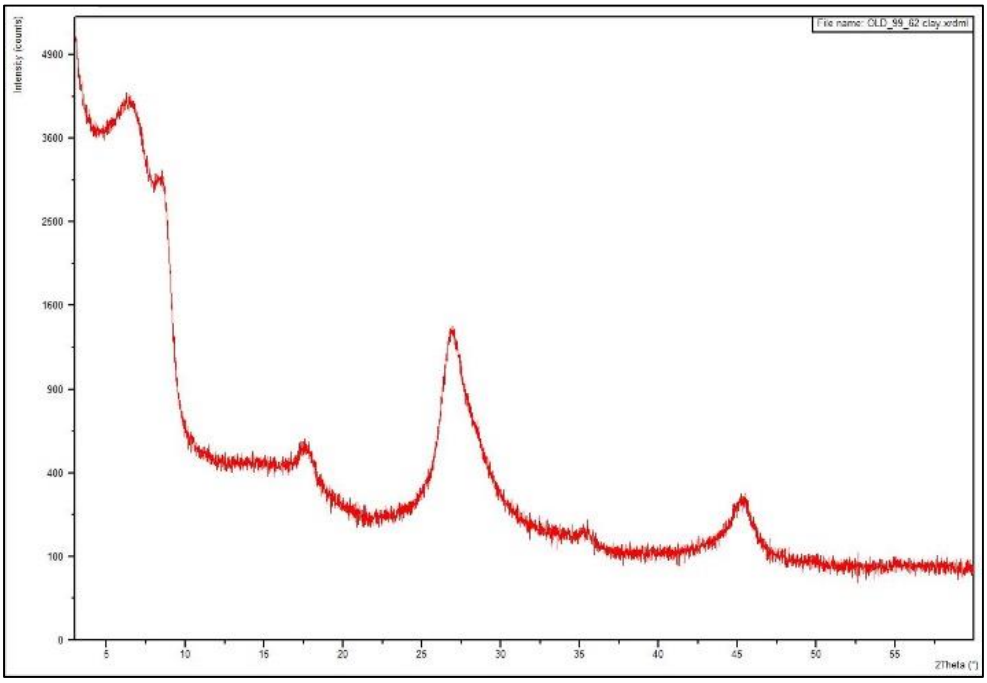

B

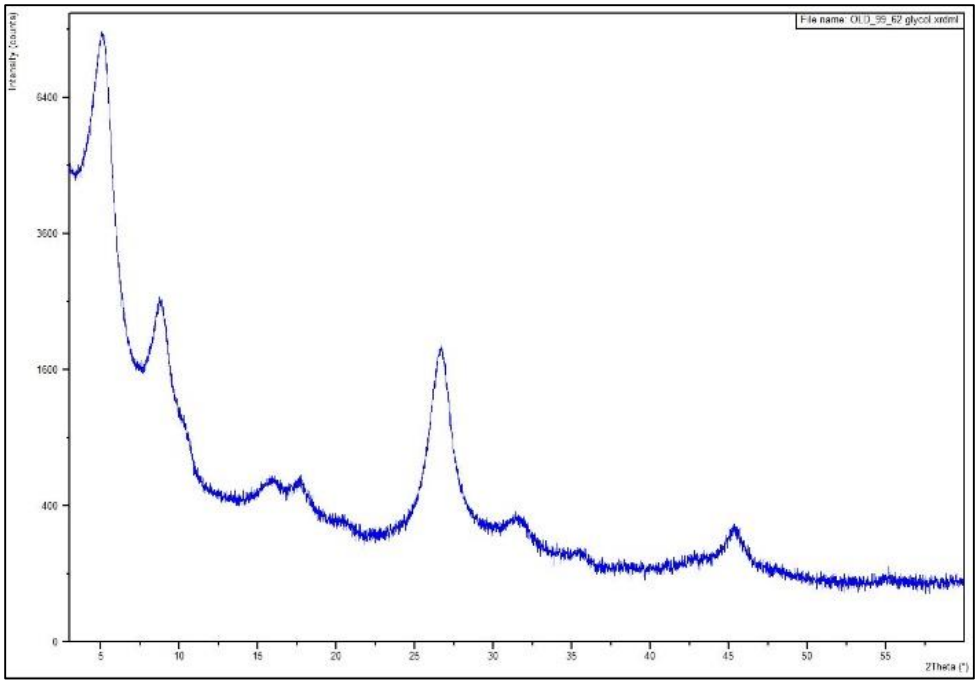

GA-L-99-62 XRD Diffractograms; air-dried (A) and glycolated (B)

A

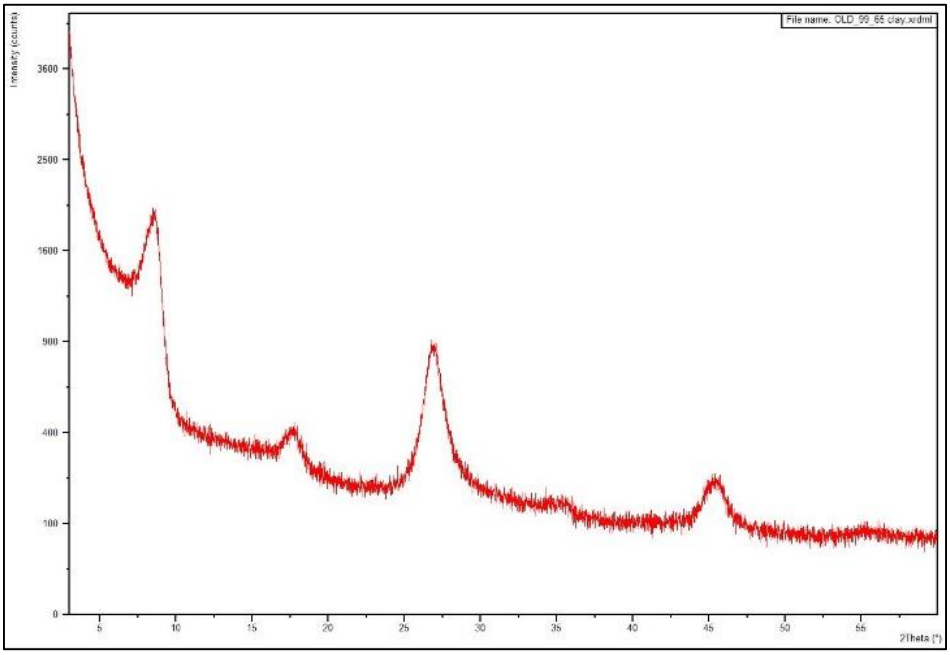

B

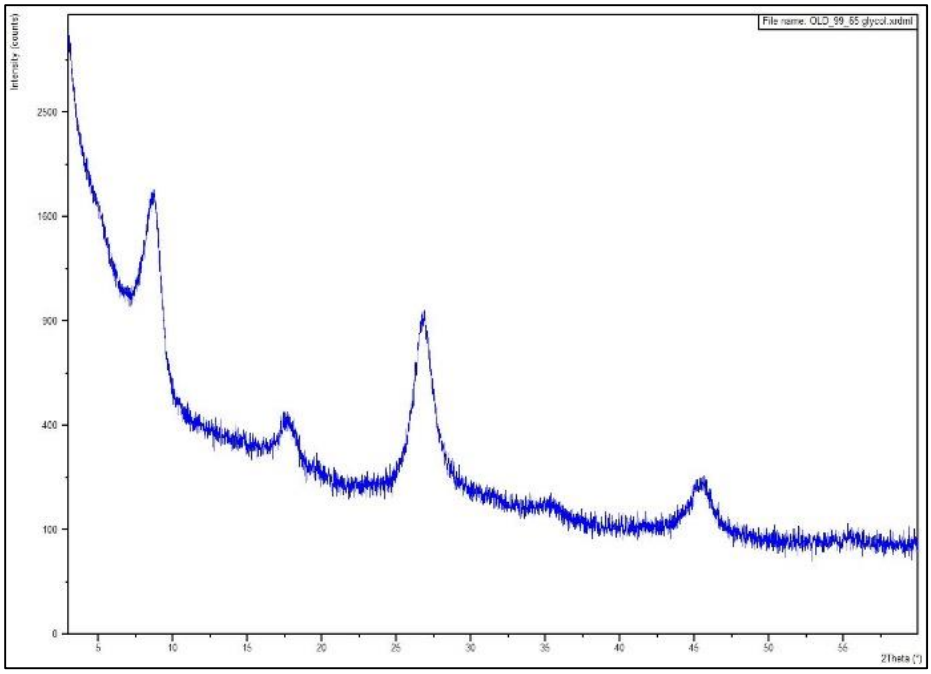

GA-L-99-65 XRD Diffractograms; air-dried (A) and glycolated (B)

A

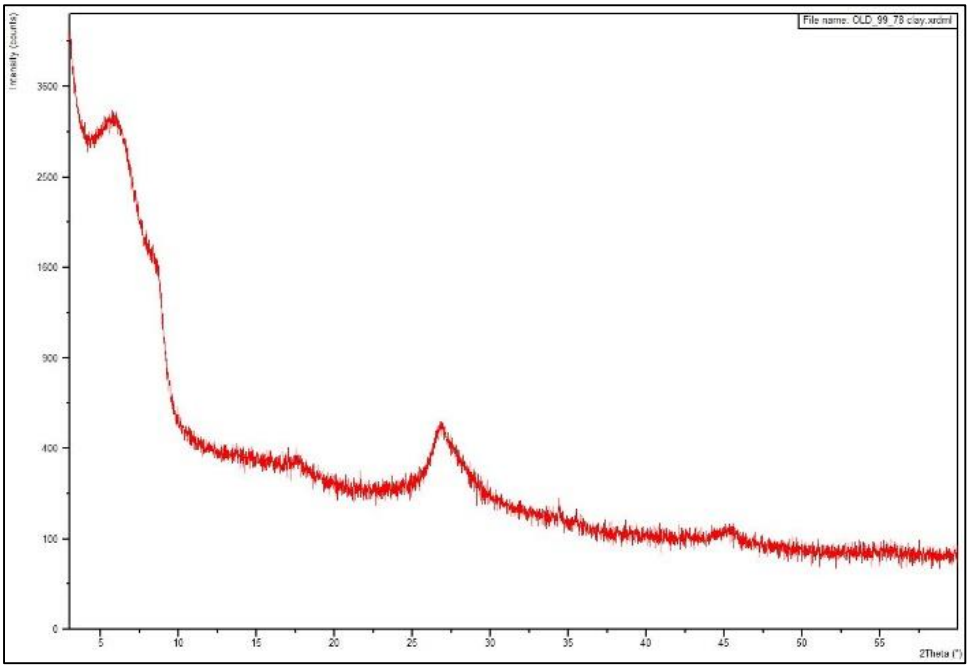

B

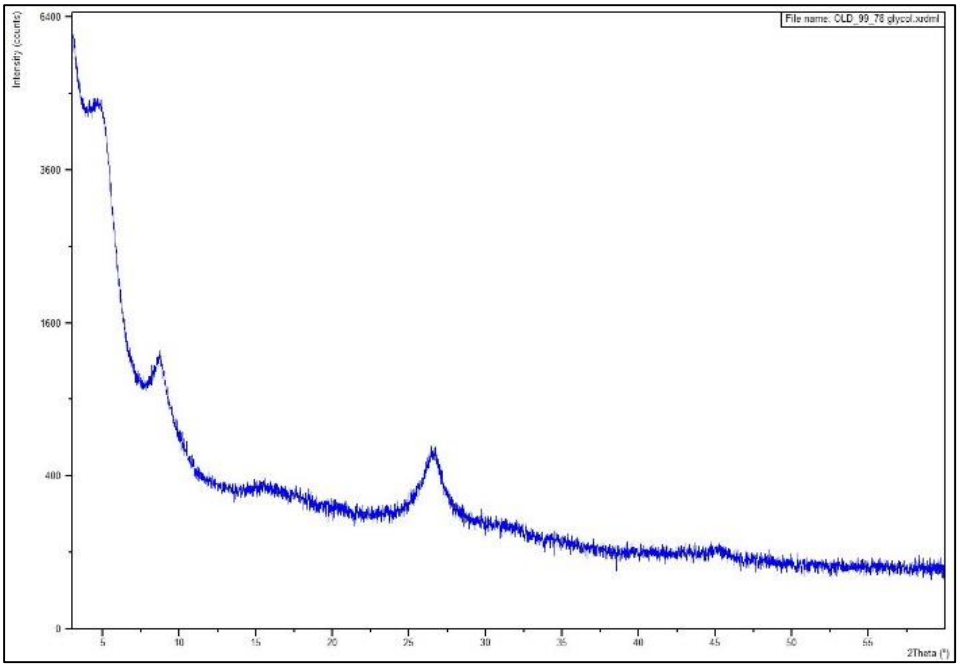

GA-L-99-78 XRD Diffractograms; air-dried (A) and glycolated (B)

A

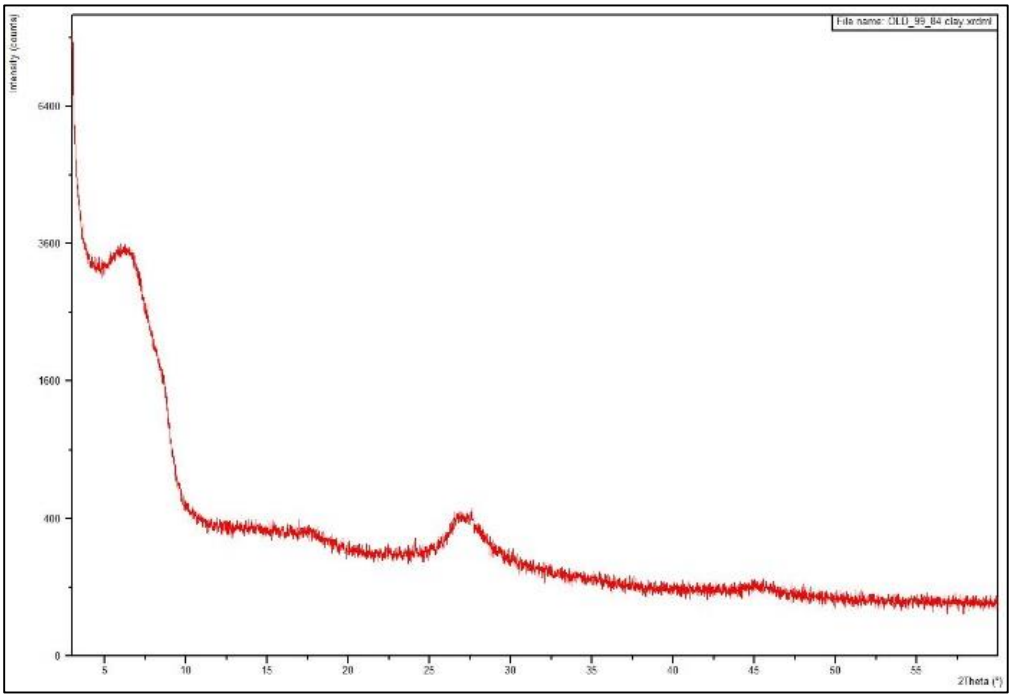

B

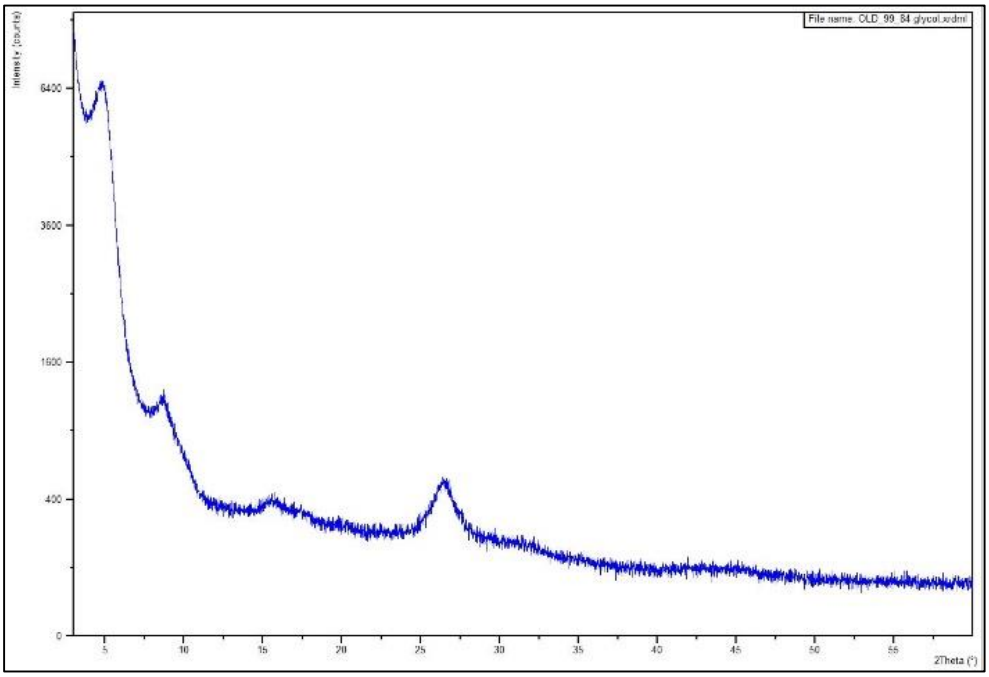

GA-L-99-84 XRD Diffractograms; air-dried (A) and glycolated (B)

A

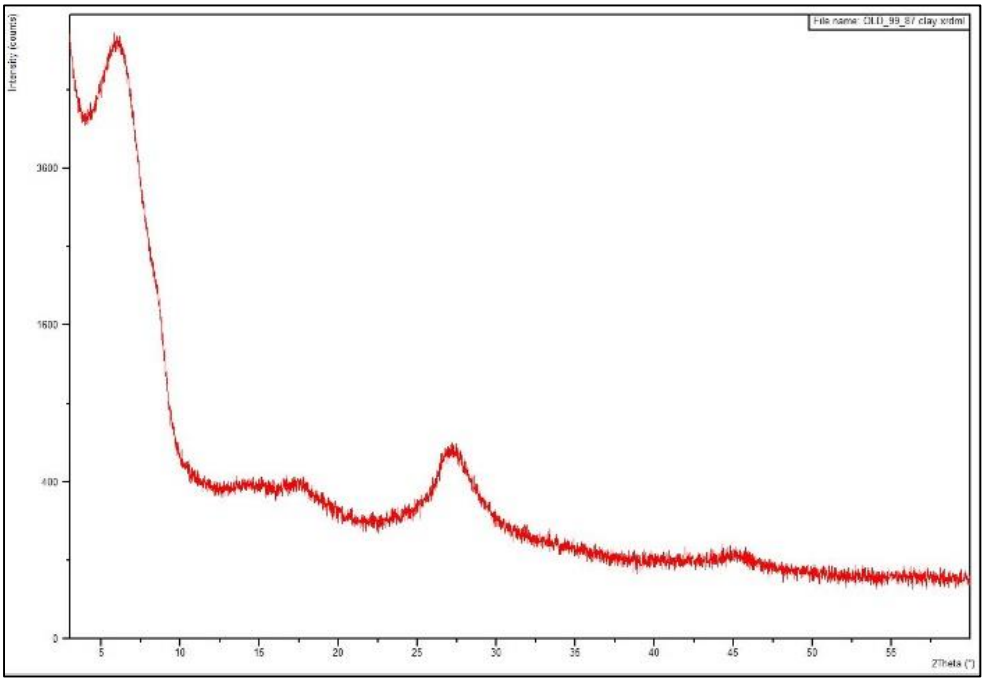

B

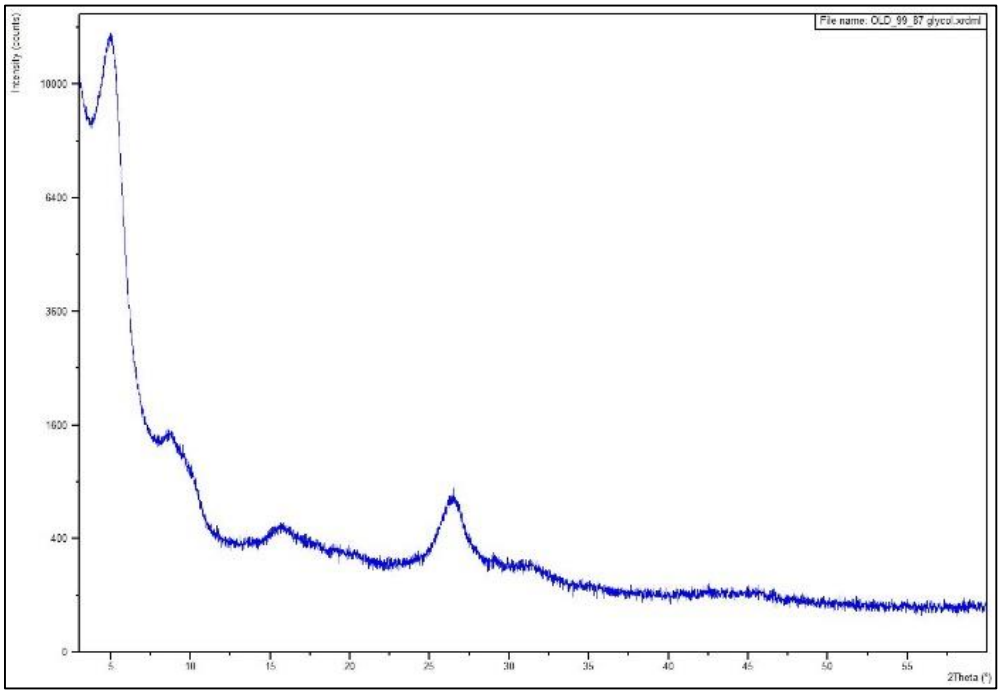

GA-L-99-87 XRD Diffractograms; air-dried (A) and glycolated (B)

A

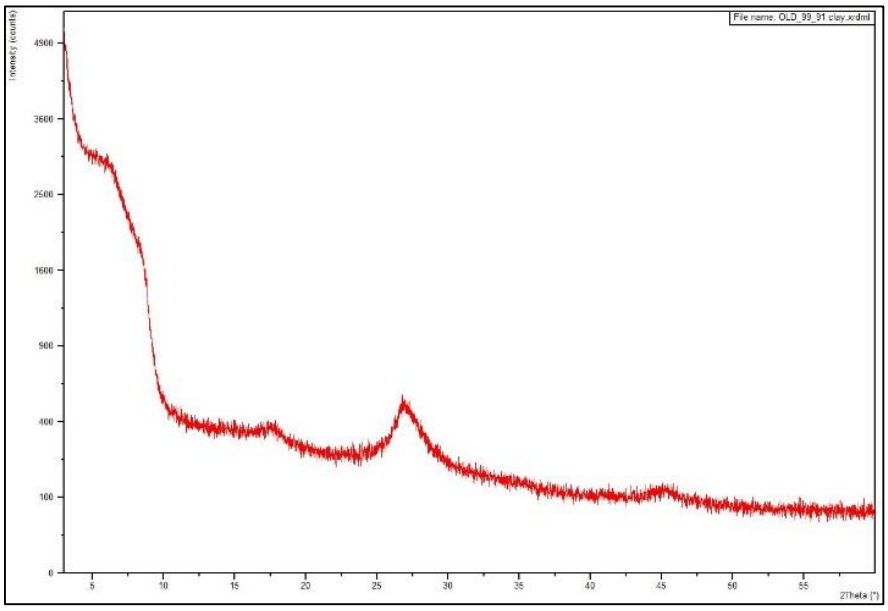

B

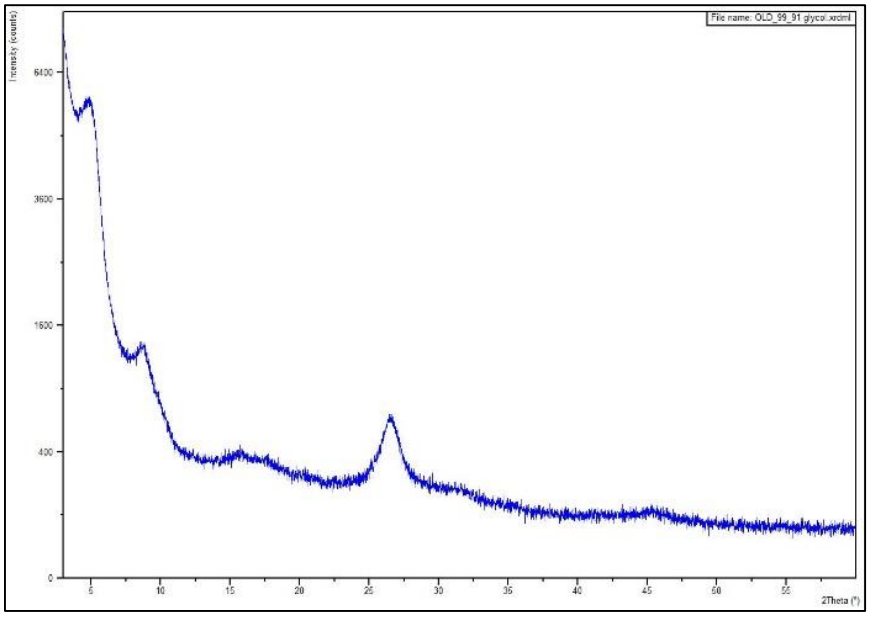

GA-L-99-91 XRD Diffractograms; air-dried (A) and glycolated (B)

A

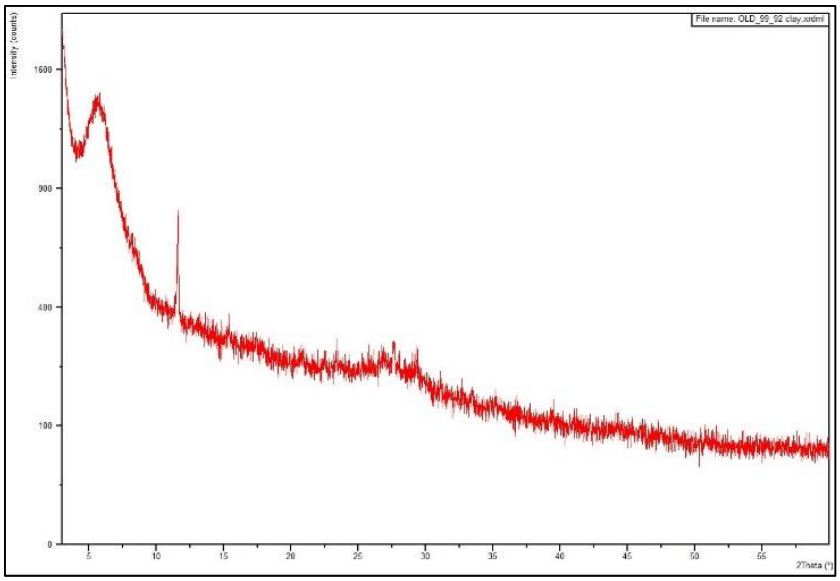

B

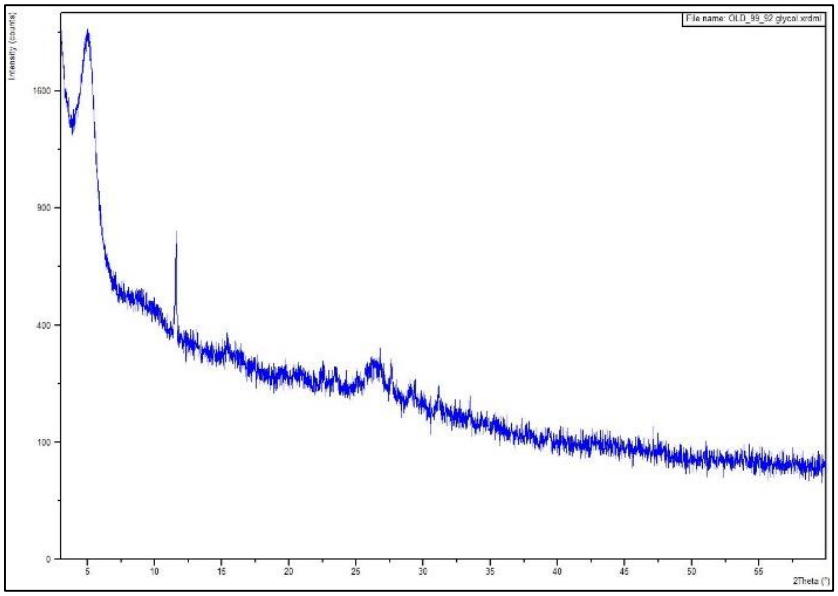

GA-L-99-92 XRD Diffractograms; air-dried (A) and glycolated (B)

A

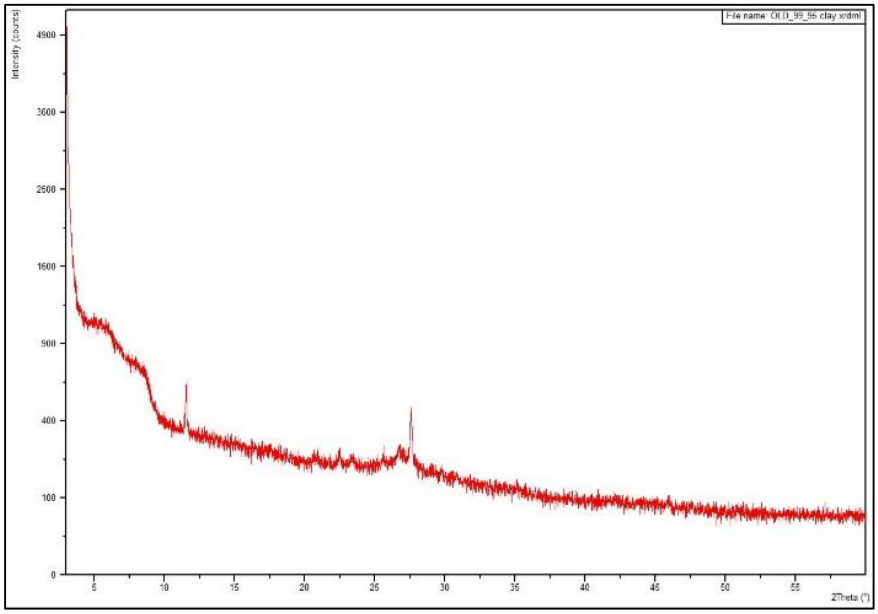

B

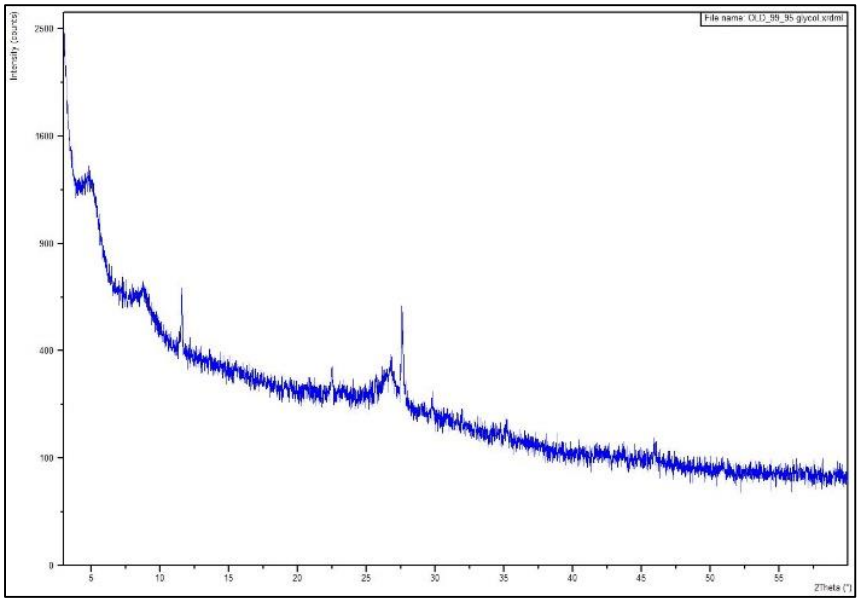

GA-L-99-95 XRD Diffractograms; air-dried (A) and glycolated (B)

A

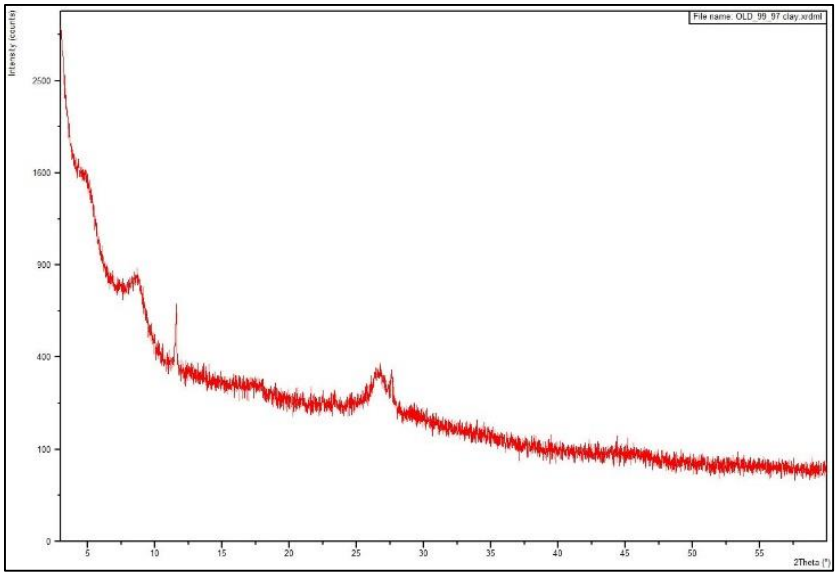

B

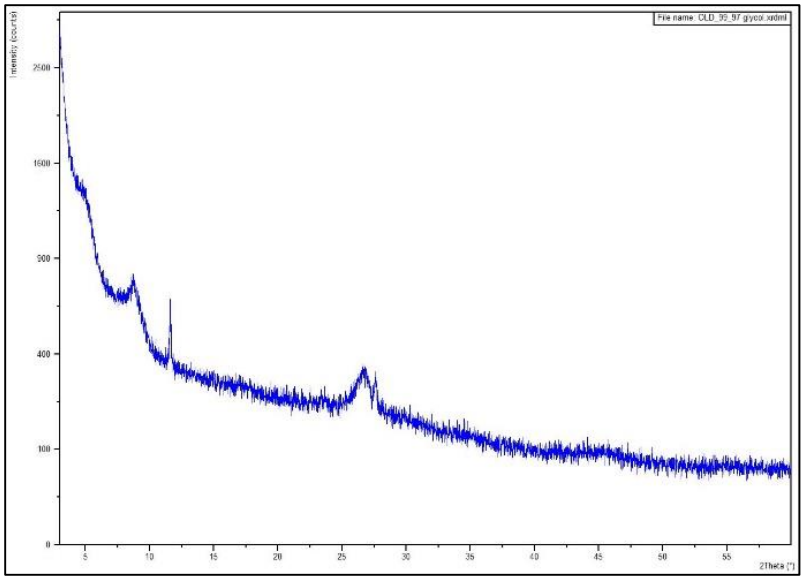

GA-L-99-97 XRD Diffractograms; air-dried (A) and glycolated (B)

A

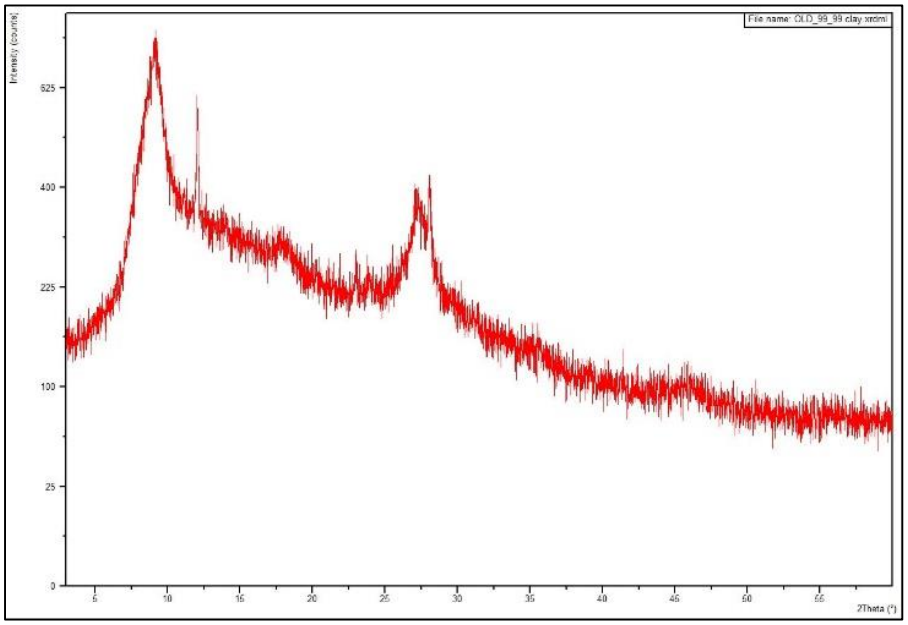

B

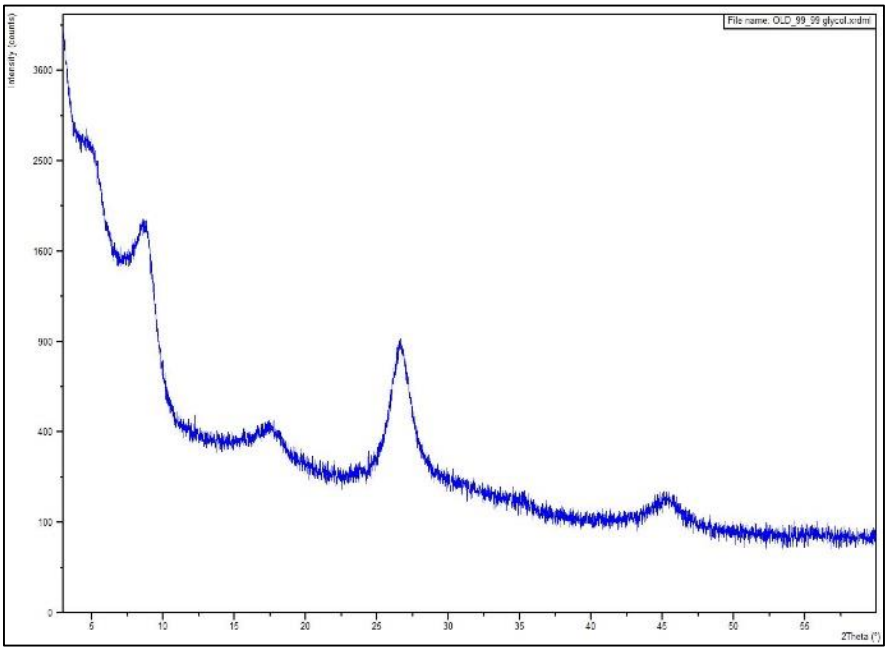

GA-L-99-99 XRD Diffractograms; air-dried (A) and glycolated (B)

A

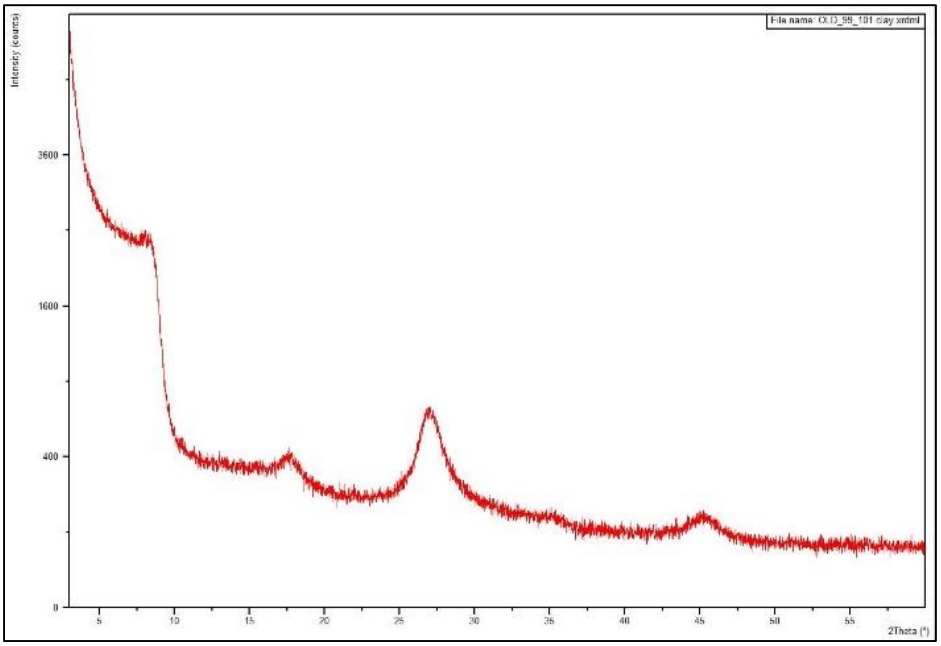

B

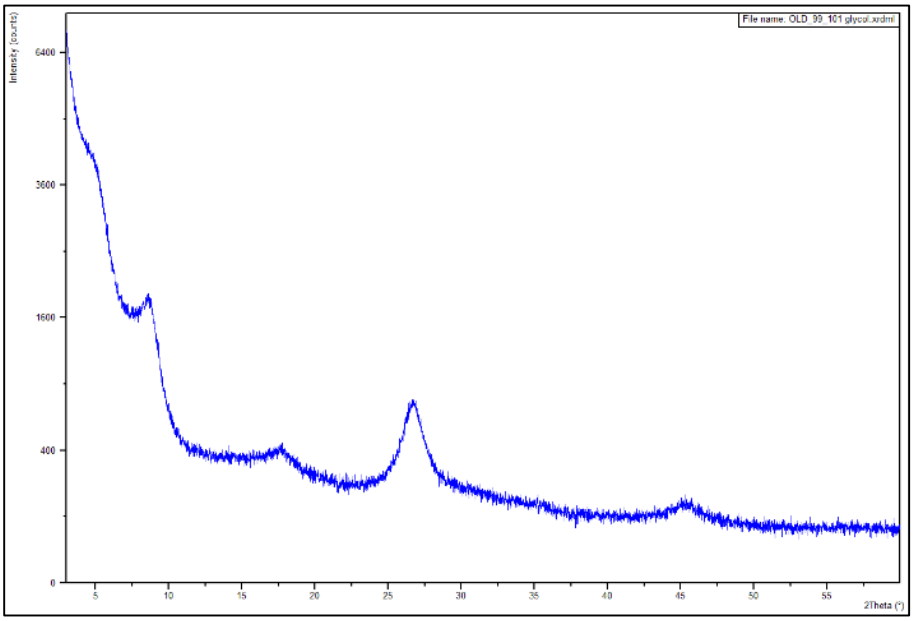

GA-L-99-101 XRD Diffractograms; air-dried (A) and glycolated (B)

A

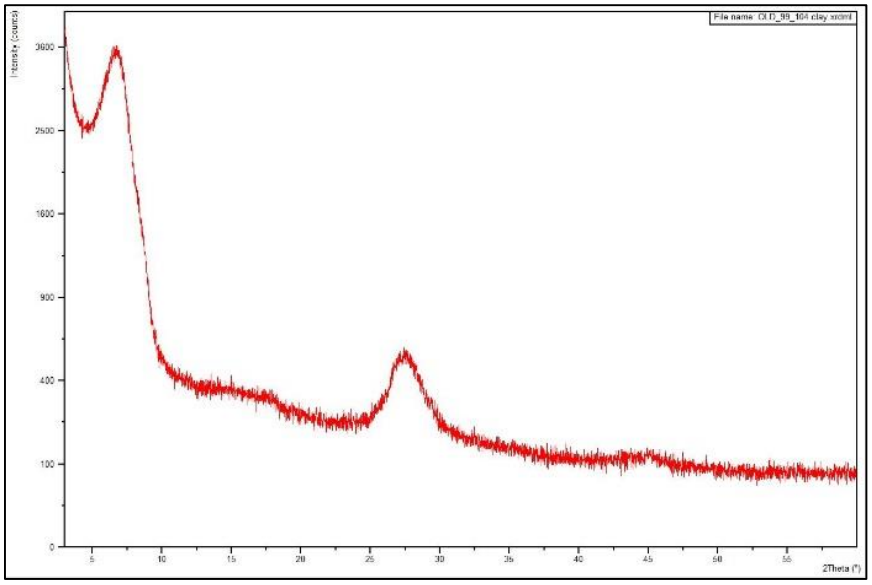

B

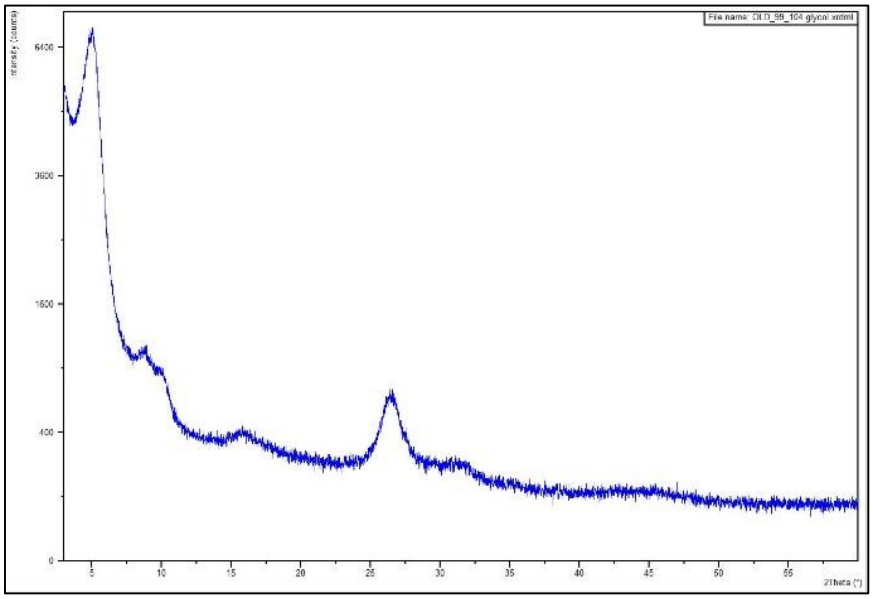

GA-L-99-104 XRD Diffractograms; air-dried (A) and glycolated (B)

A

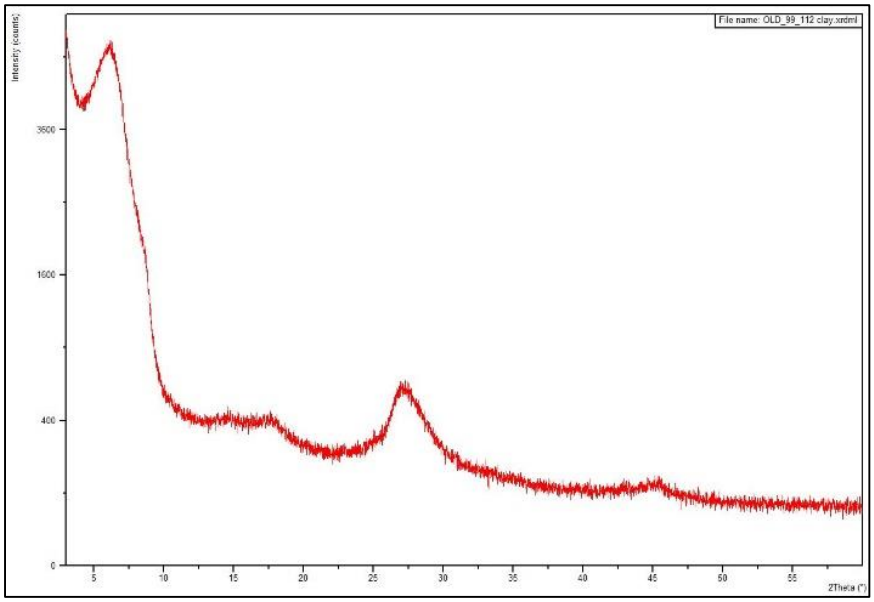

B

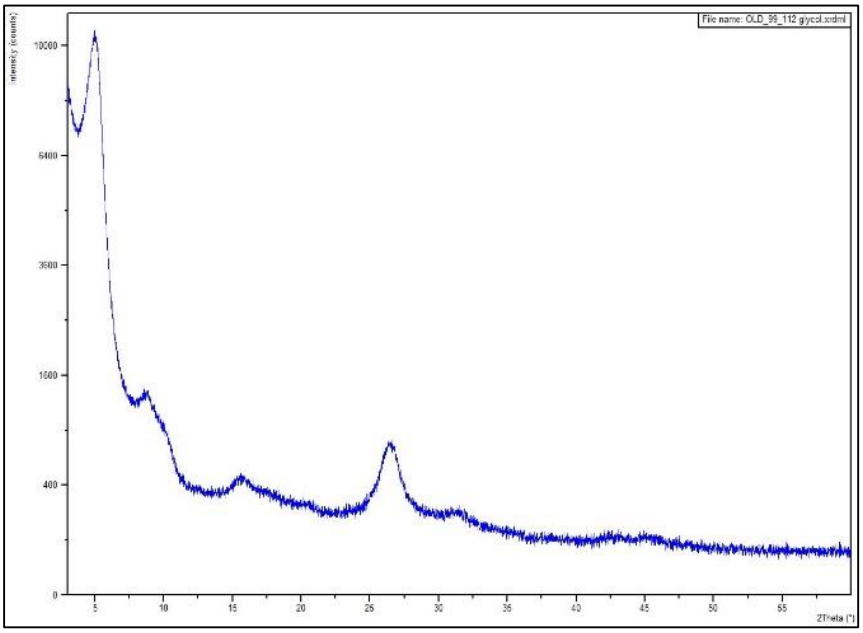

GA-L-99-112 XRD Diffractograms; air-dried (A) and glycolated (B)

A

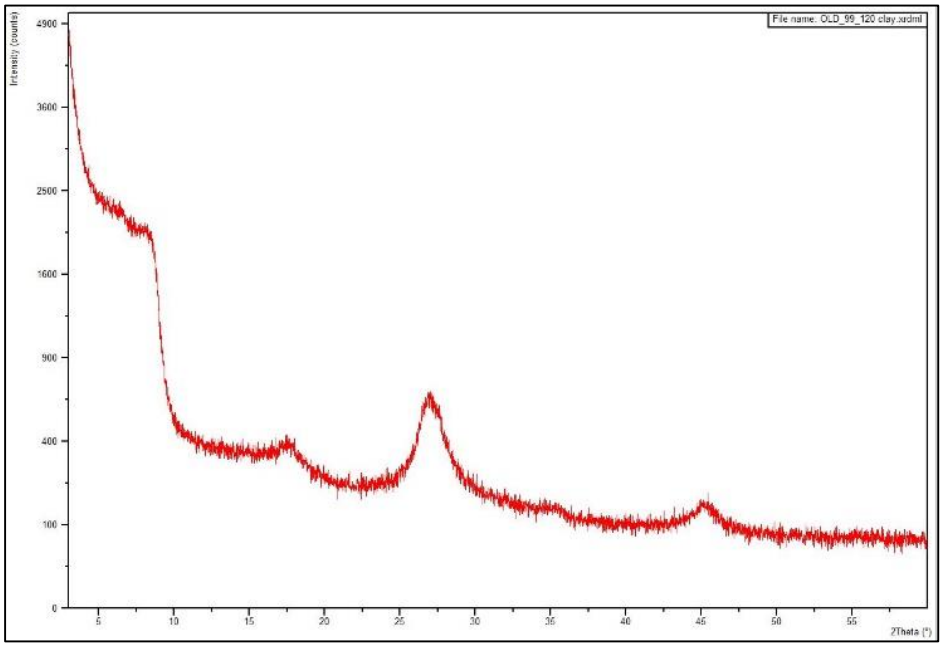

B

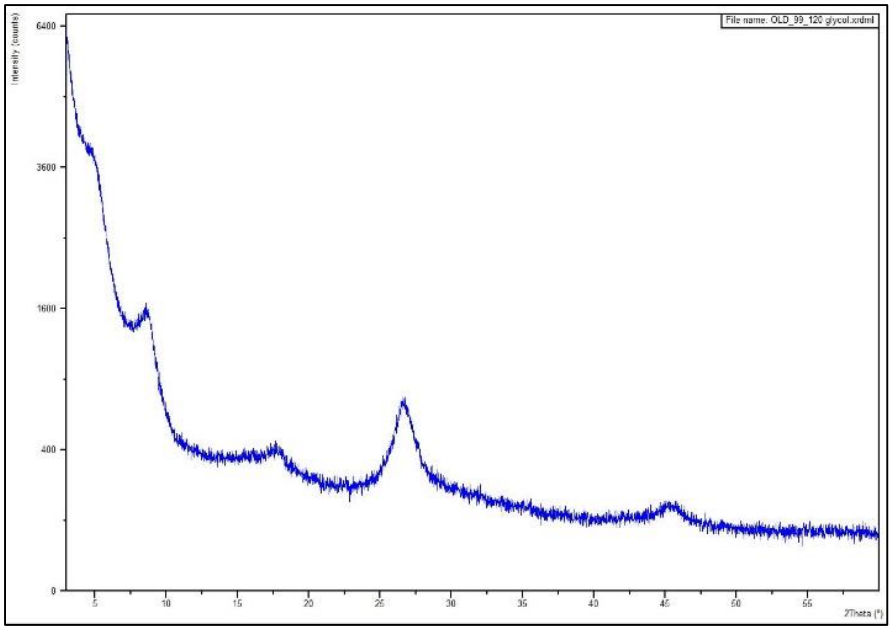

GA-L-99-120 XRD Diffractograms; air-dried (A) and glycolated (B)

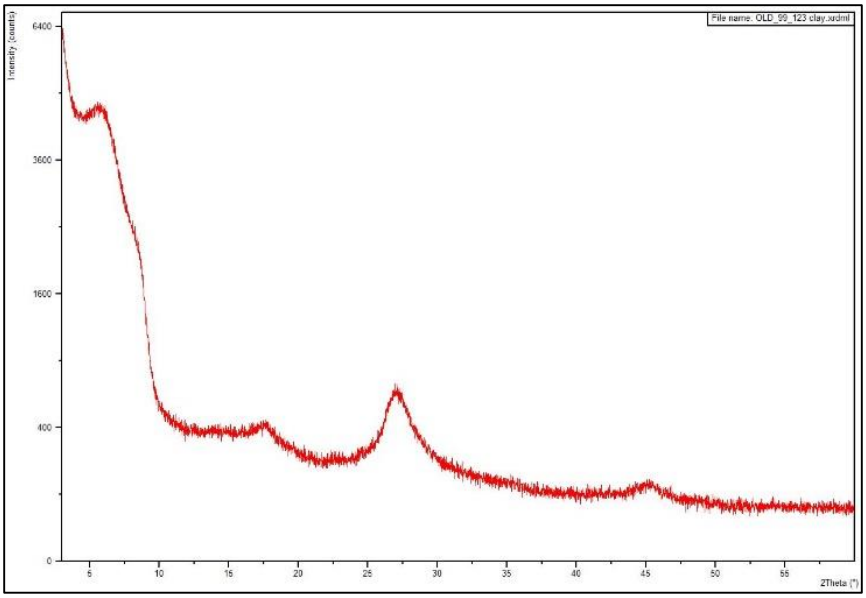

B

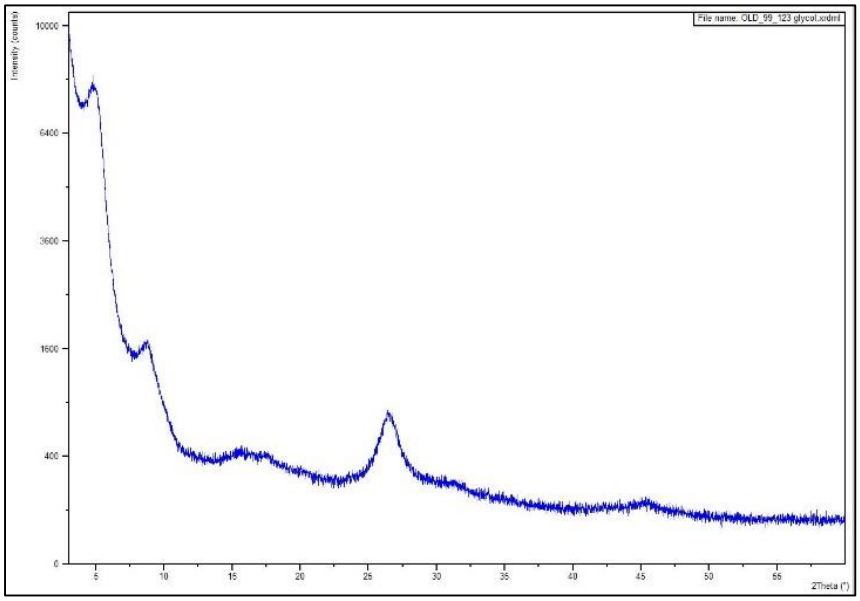

GA-L-99-123 XRD Diffractograms; air-dried (A) and glycolated (B)

A

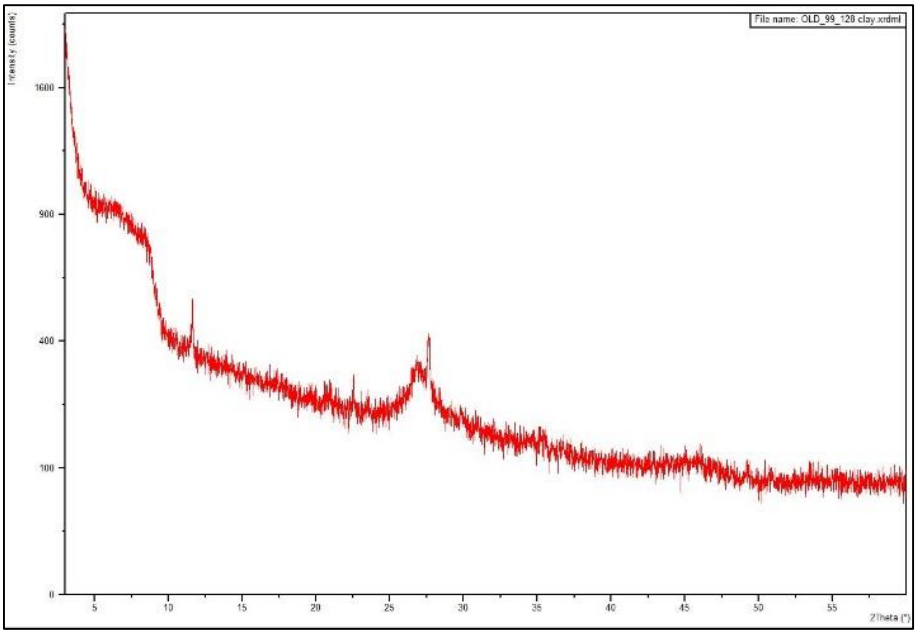

B

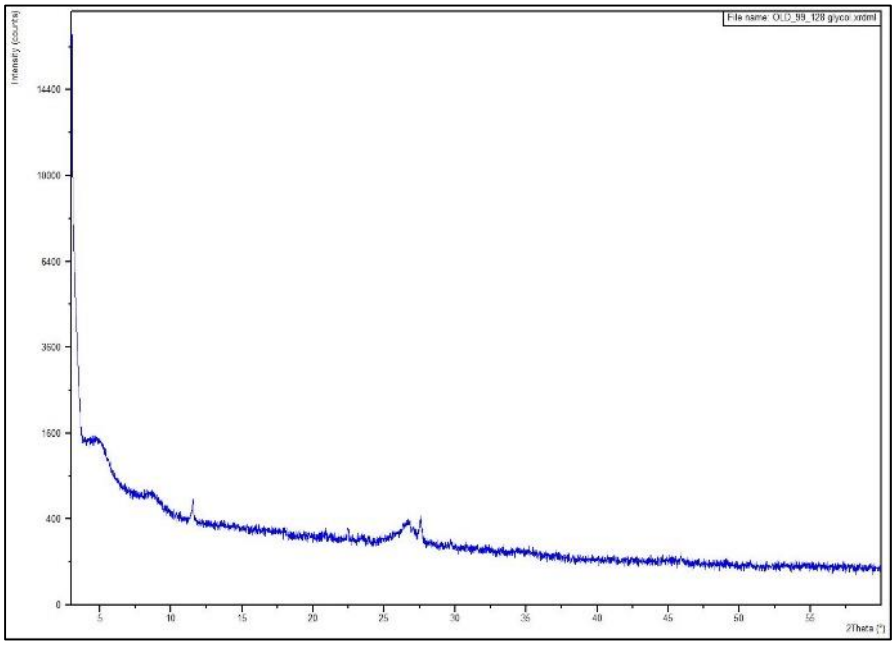

GA-L-99-128 XRD Diffractograms; air-dried (A) and glycolated (B)

A

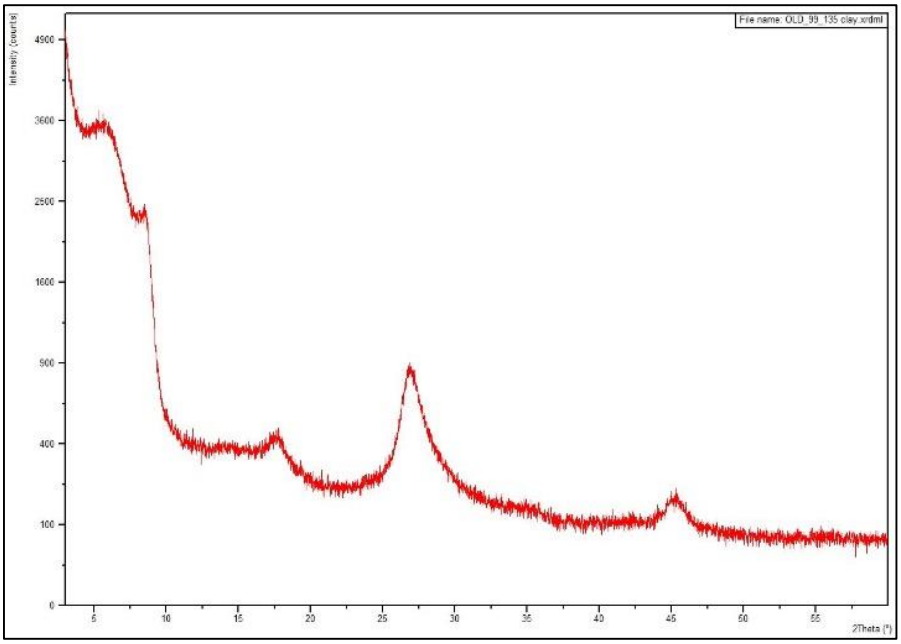

B

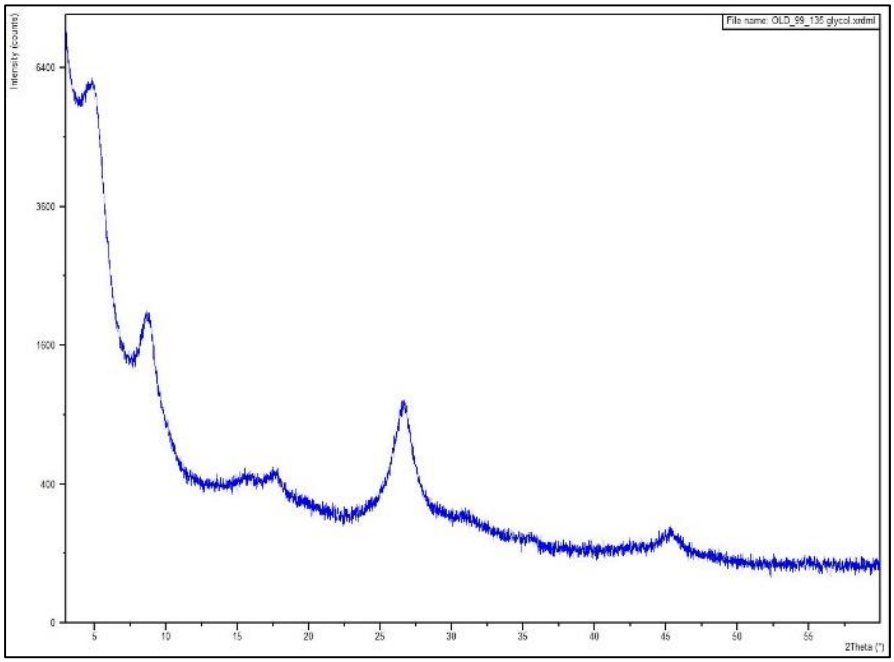

GA-L-99-135 XRD Diffractograms; air-dried (A) and glycolated (B)

A

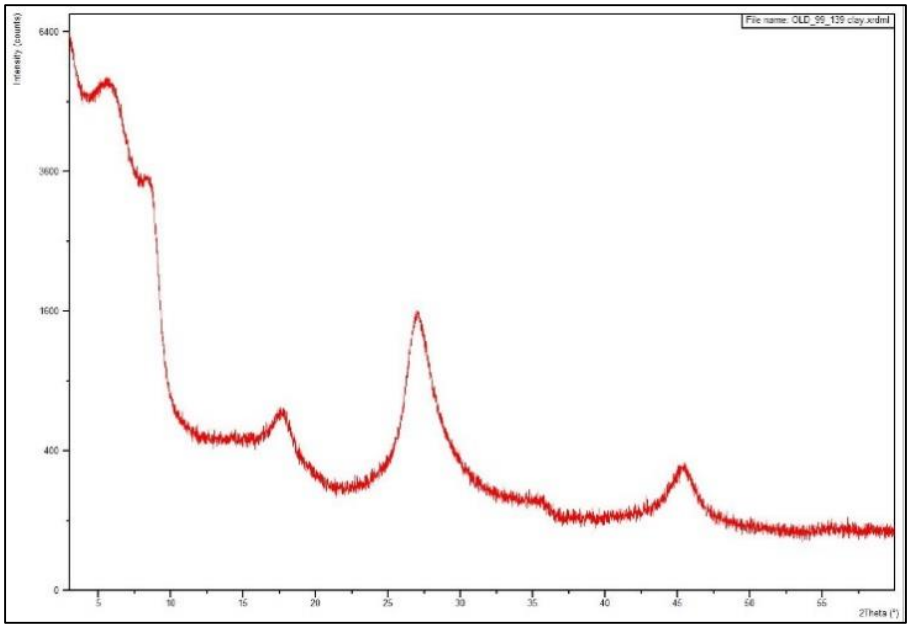

B

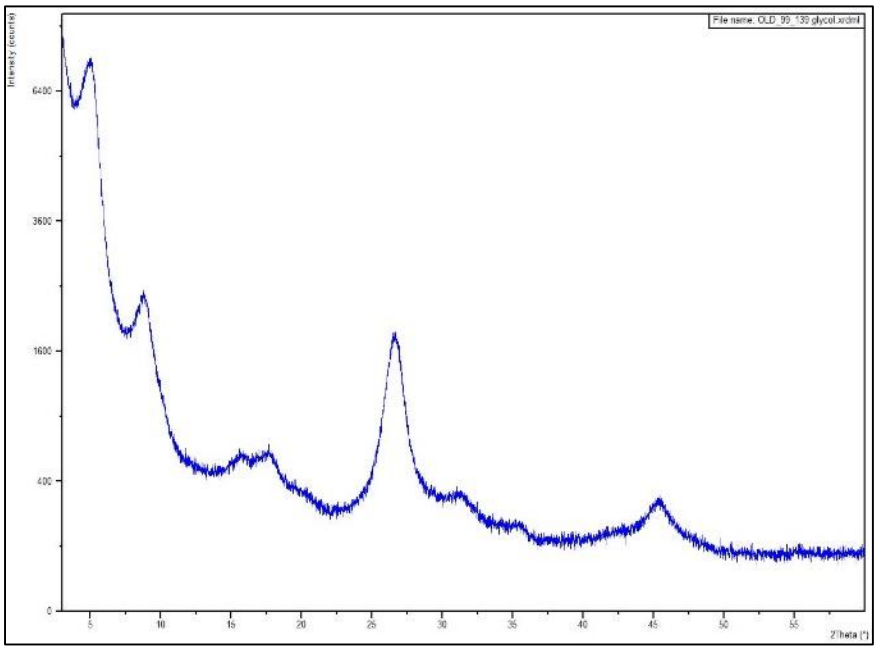

GA-L-99-139 XRD Diffractograms; air-dried (A) and glycolated (B)

A

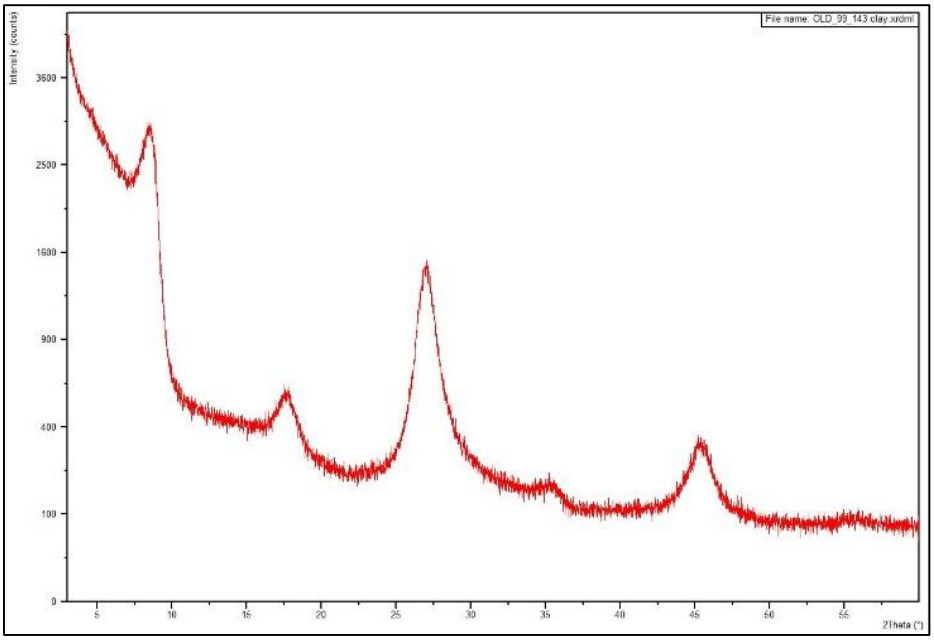

B

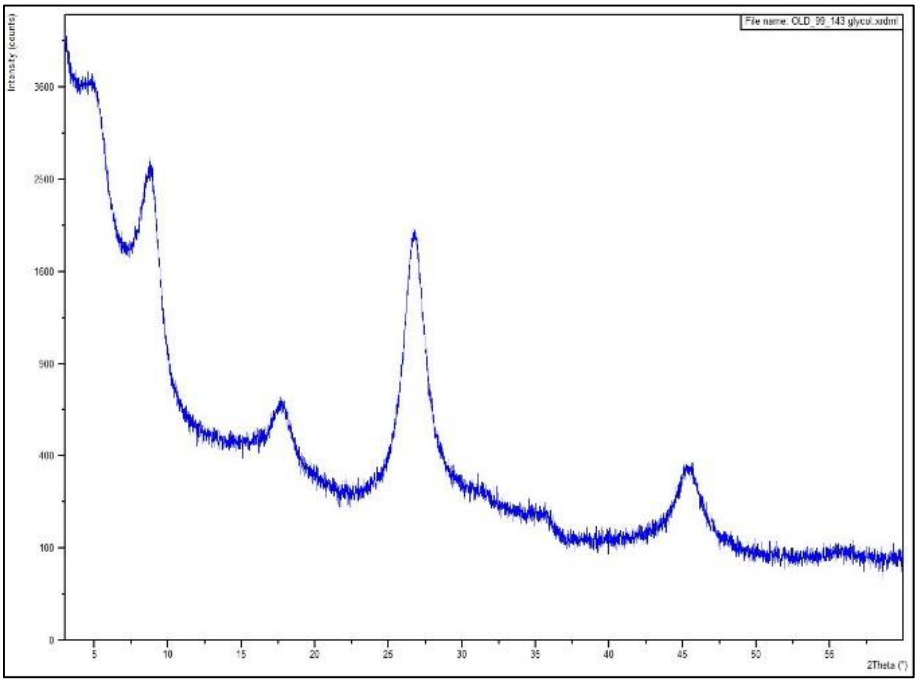

GA-L-99-143 XRD Diffractograms; air-dried (A) and glycolated (B)

A

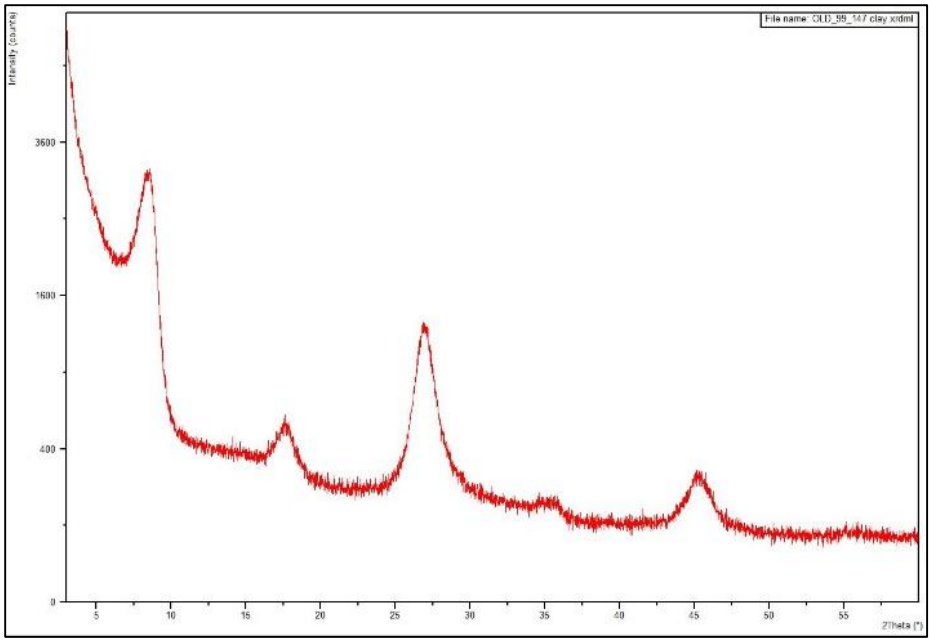

B

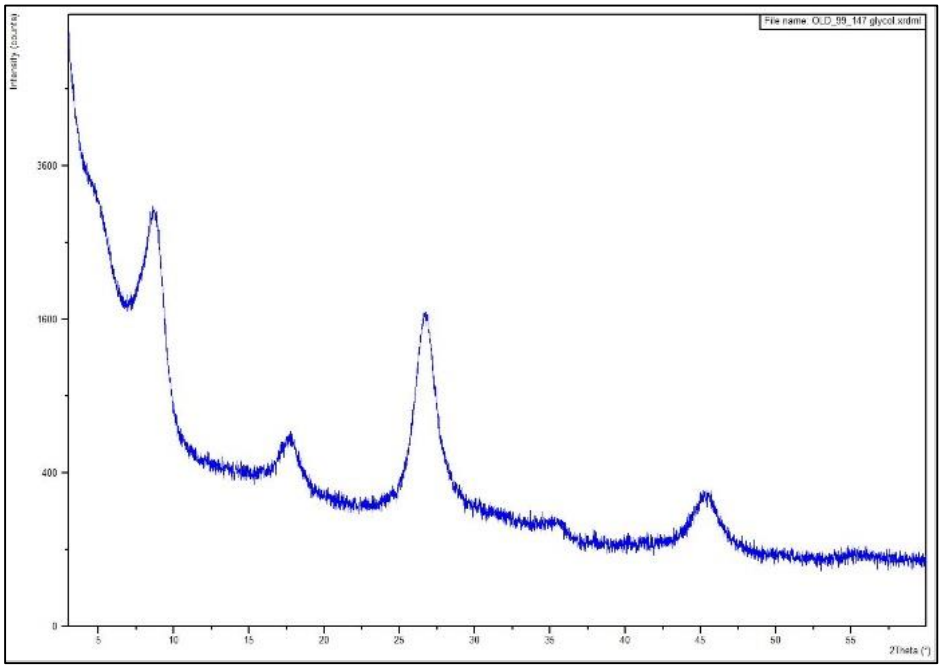

GA-L-99-147 XRD Diffractograms; air-dried (A) and glycolated (B)

A

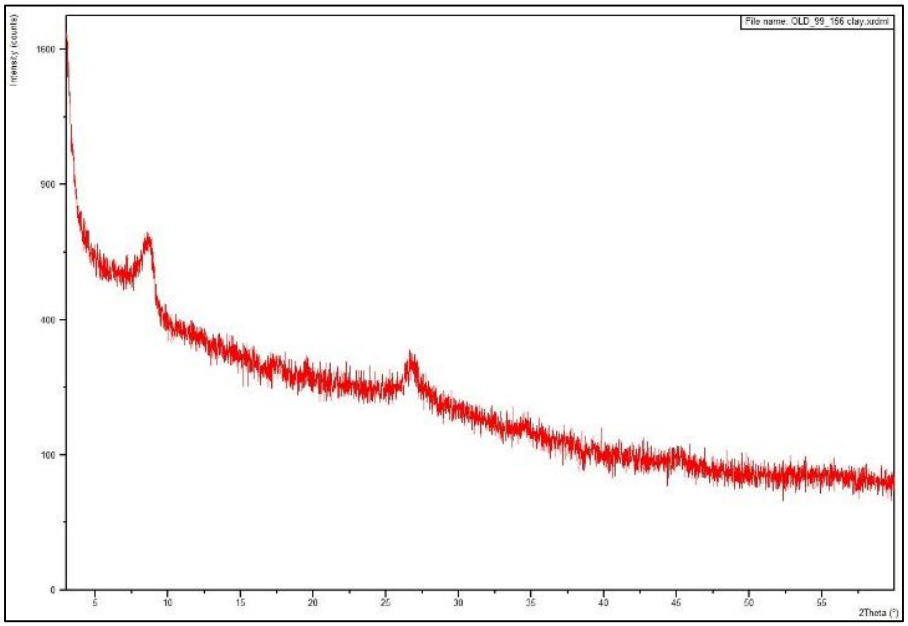

B

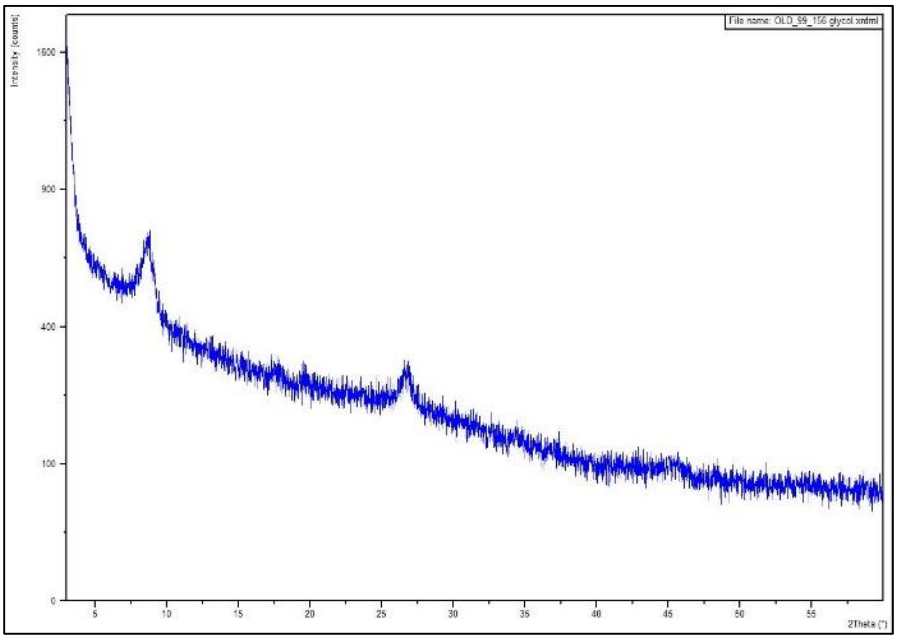

GA-L-99-156 XRD Diffractograms; air-dried (A) and glycolated (B)

A

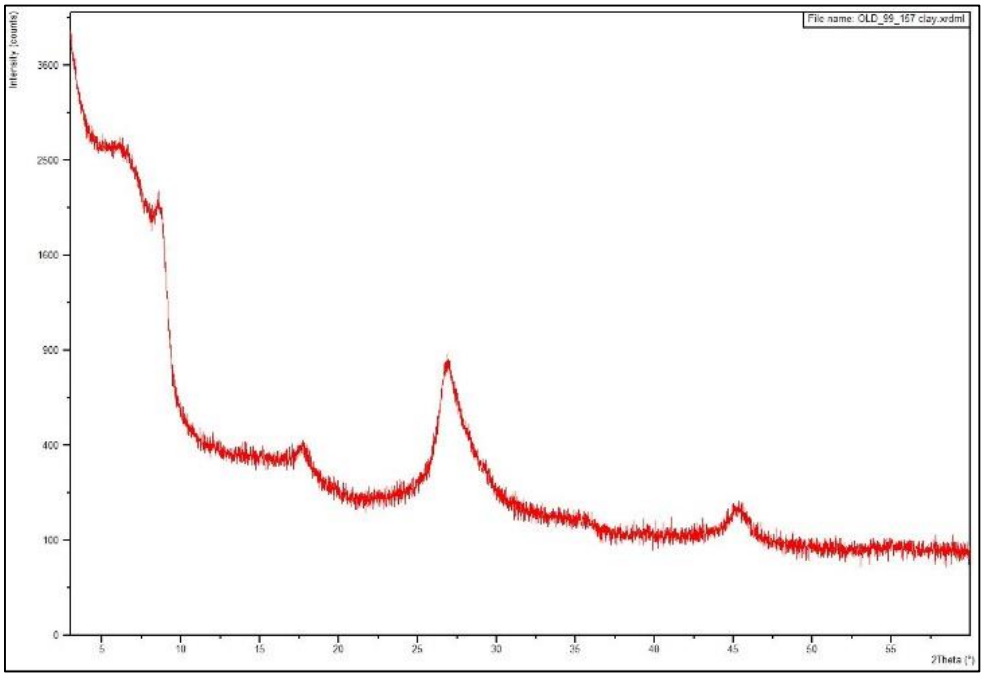

B

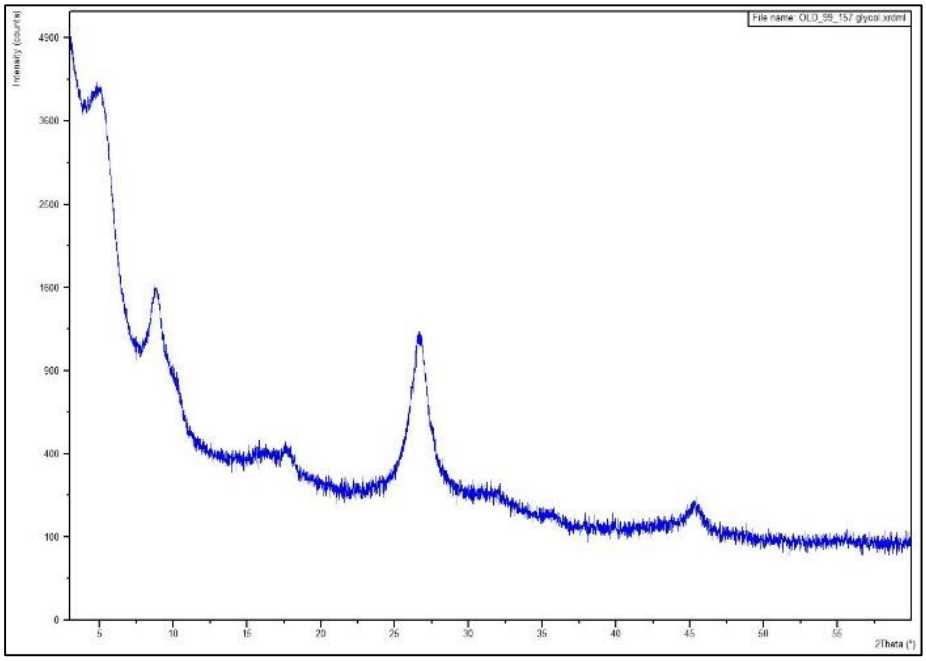

GA-L-99-157 XRD Diffractograms; air-dried (A) and glycolated (B)

A

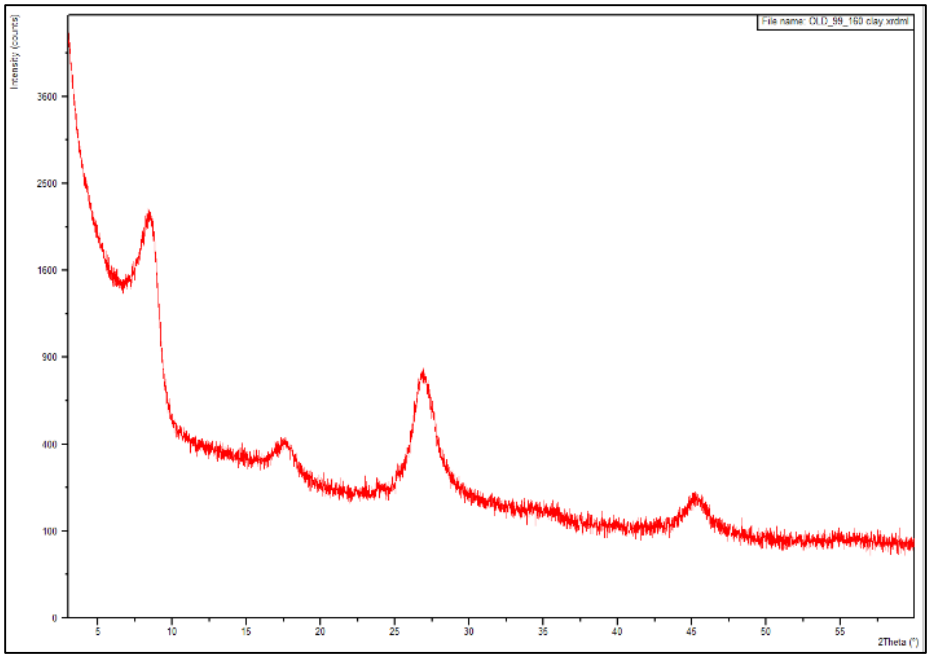

B

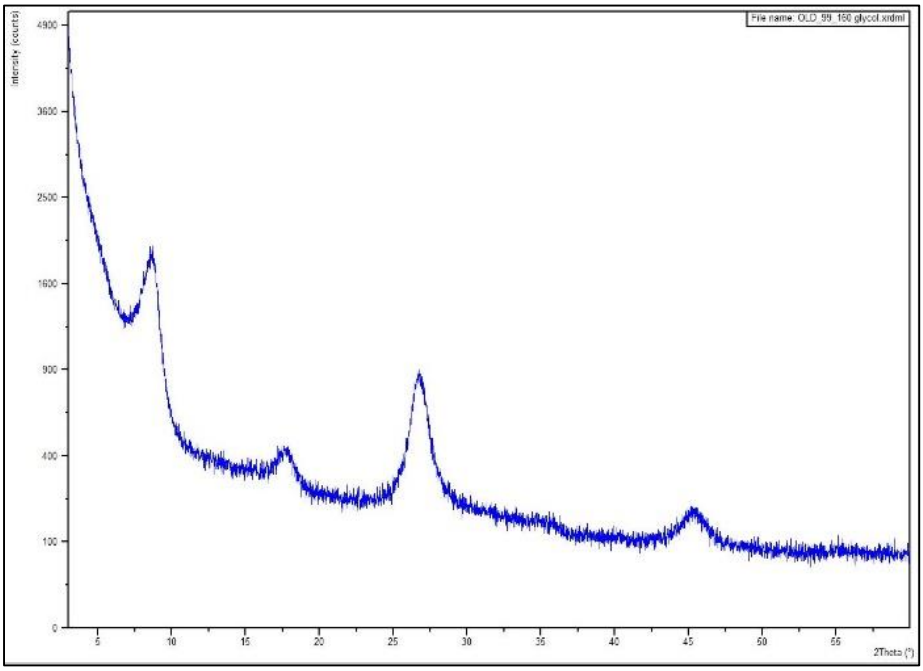

GA-L-99-160 XRD Diffractograms; air-dried (A) and glycolated (B)

A

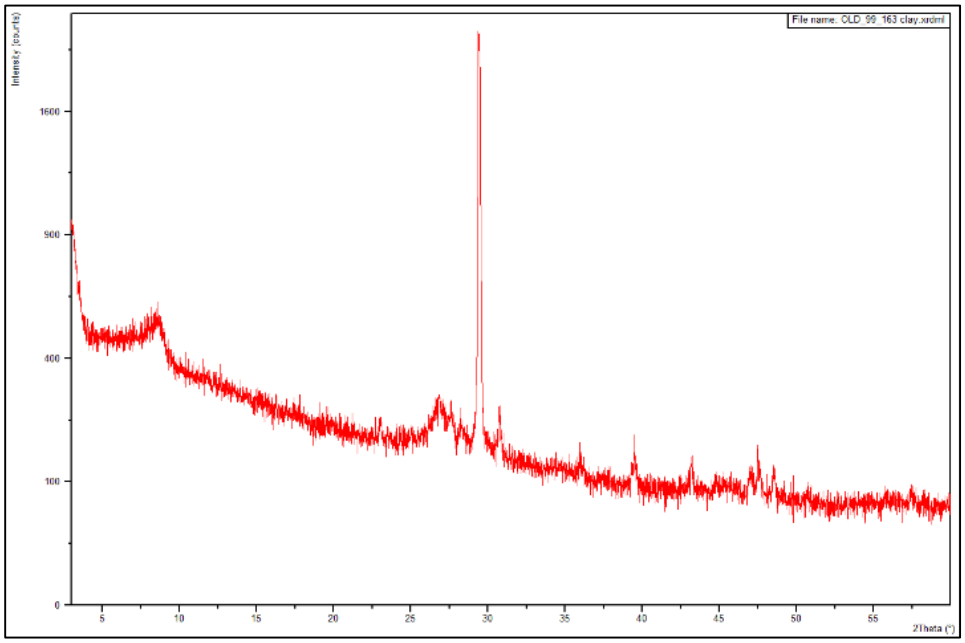

B

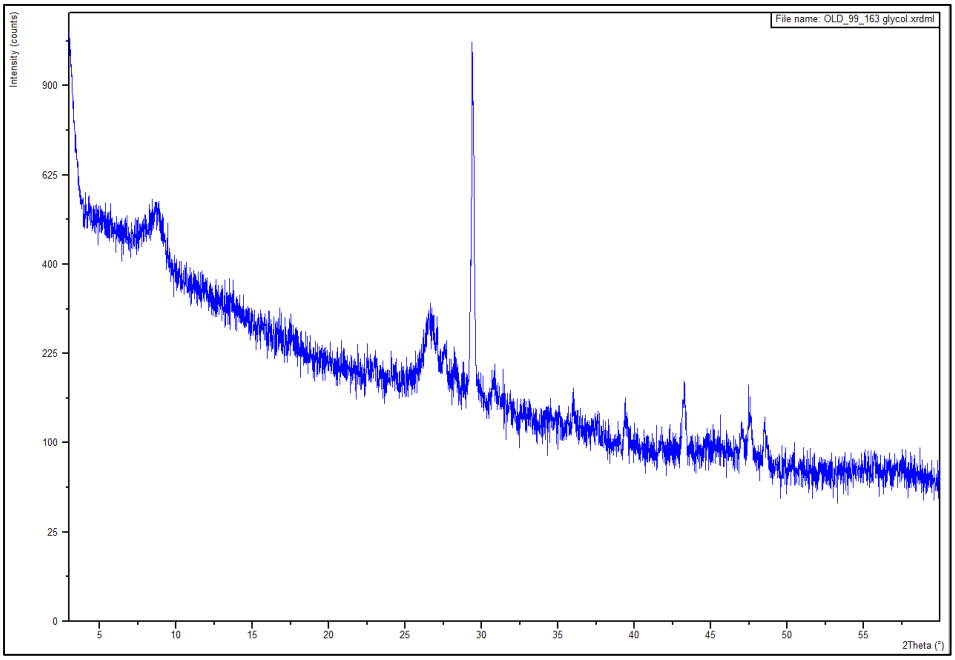

GA-L-99-163 XRD Diffractograms; air-dried (A) and glycolated (B)

A

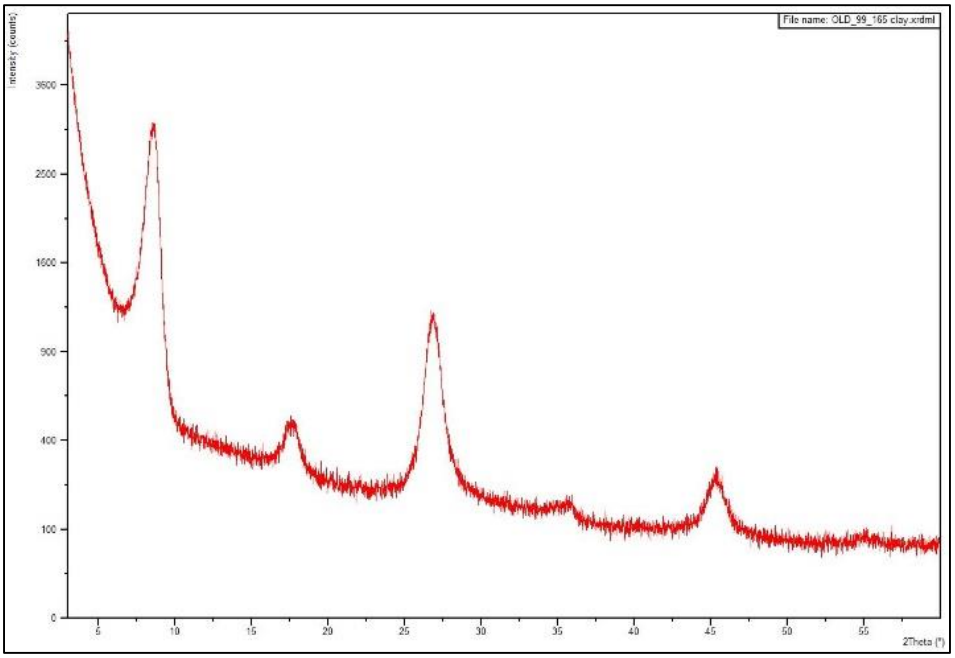

B

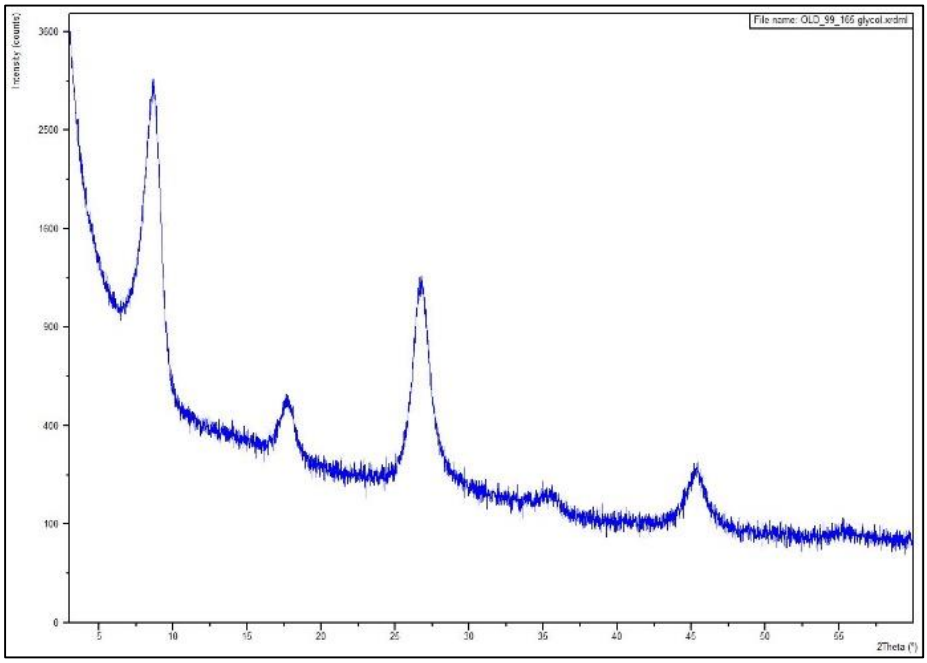

GA-L-99-165 XRD Diffractograms; air-dried (A) and glycolated (B)

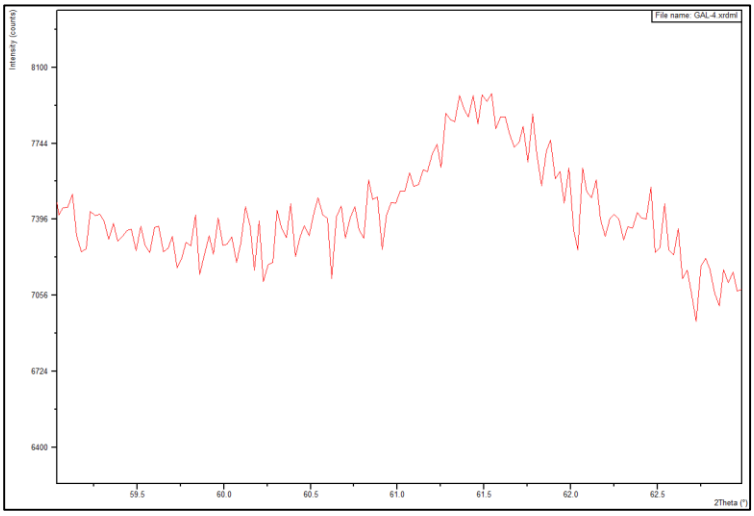

GA-L-99-4 XRD d060 Diffractogram

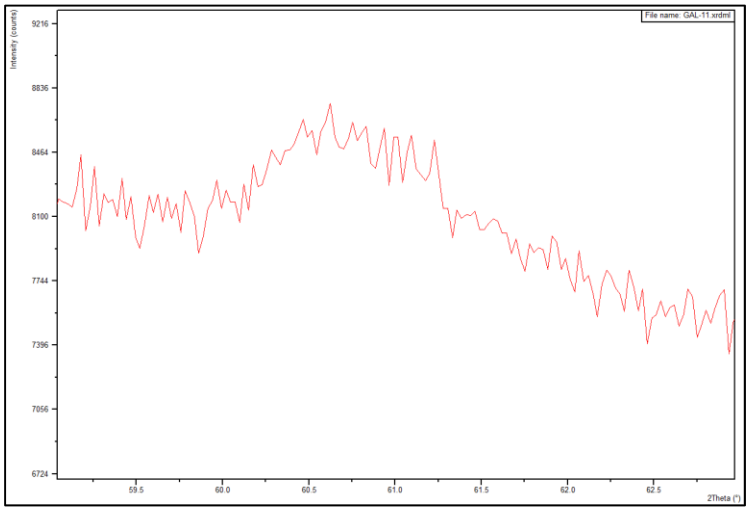

GA-L-99-11 XRD d060 Diffractogram

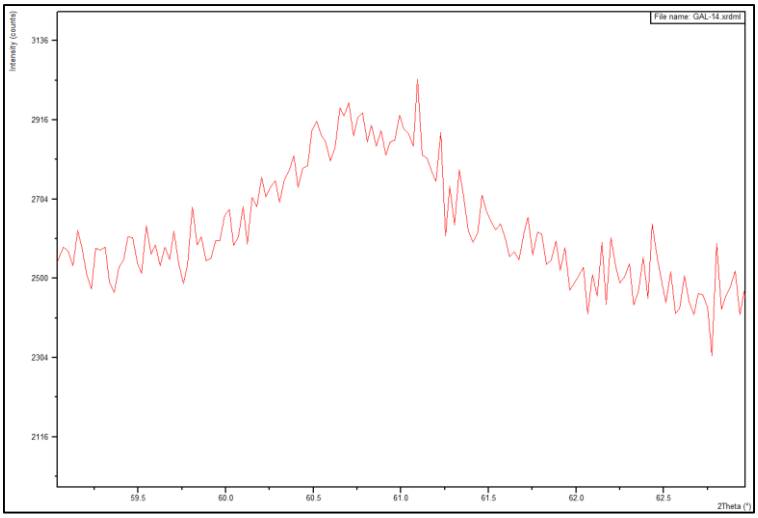

GA-L-99-14 XRD d060 Diffractogram

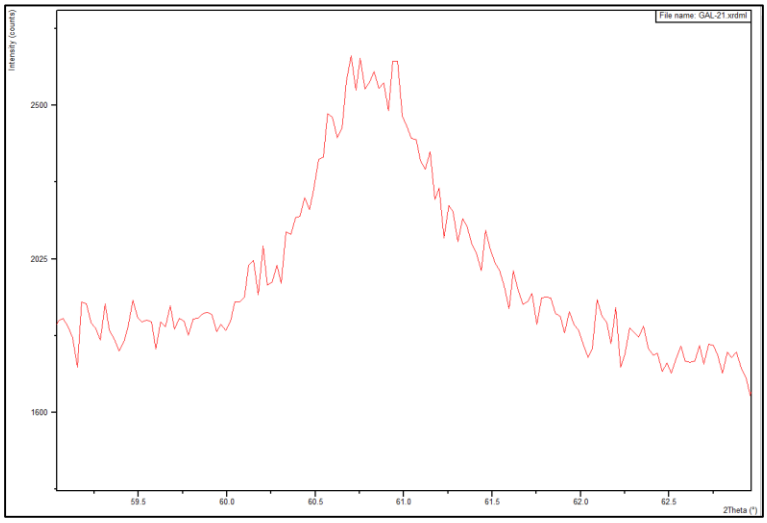

GA-L-99-21 XRD d060 Diffractogram

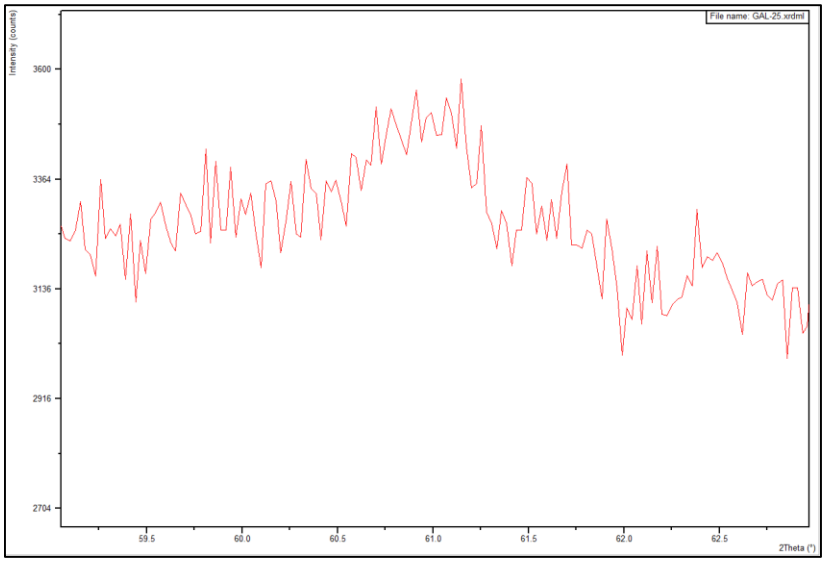

GA-L-99-25 XRD d060 Diffractogram

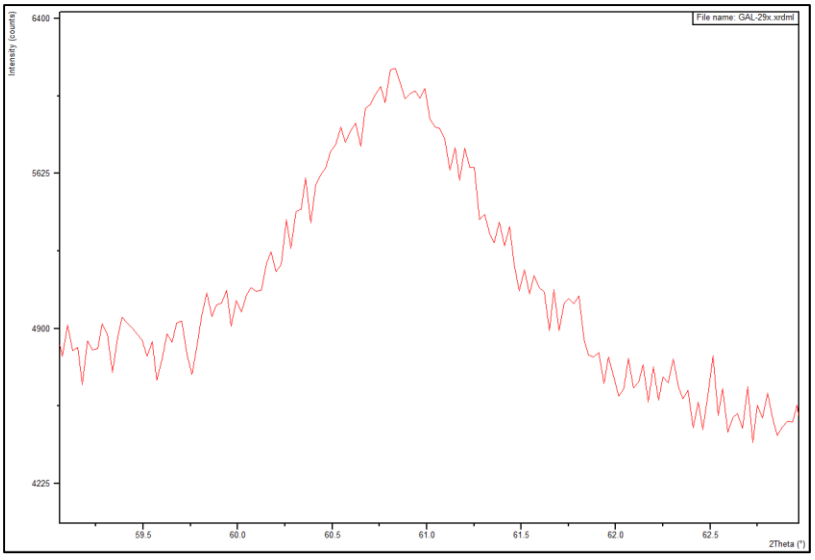

GA-L-99-29 XRD d060 Diffractogram

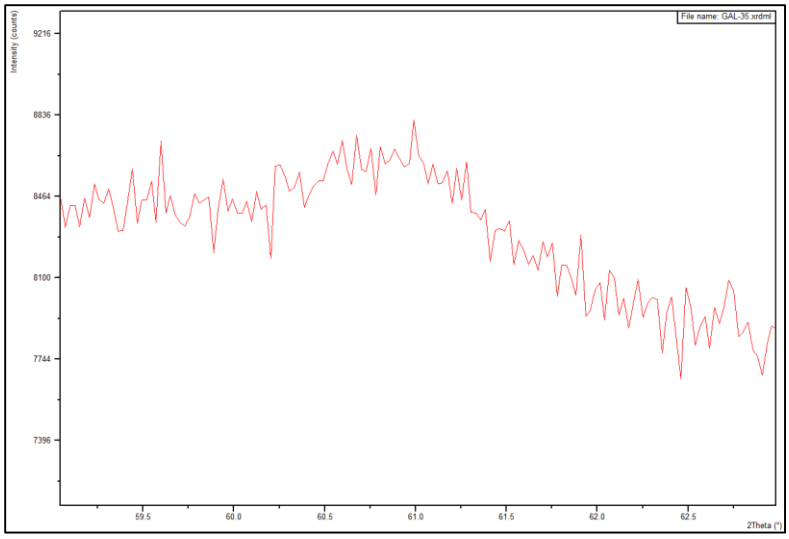

GA-L-99-35 XRD d060 Diffractogram

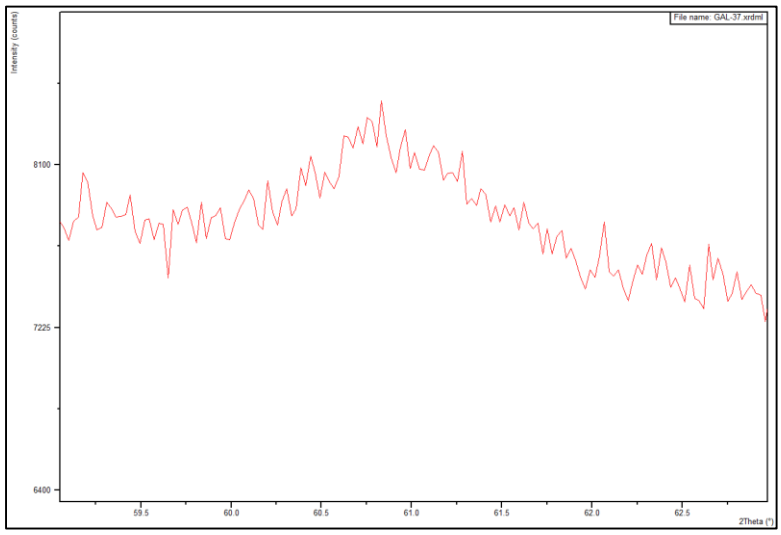

GA-L-99-37 XRD d060 Diffractogram

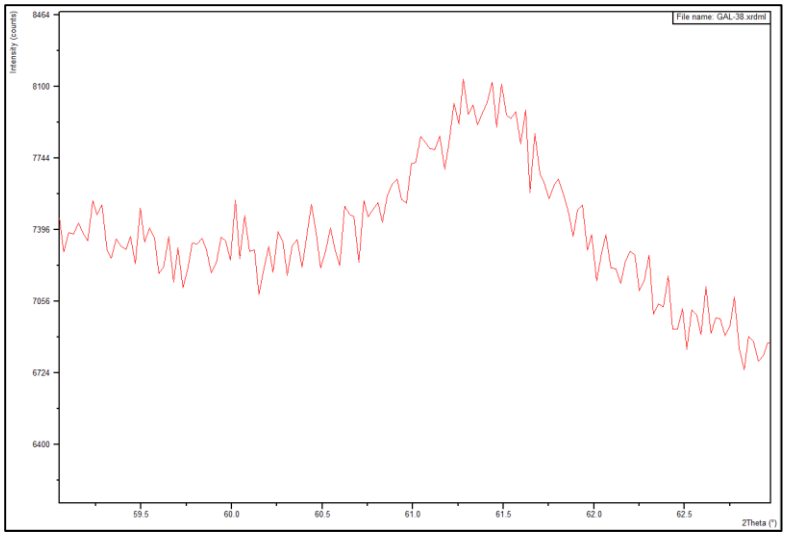

GA-L-99-38 XRD d060 Diffractogram

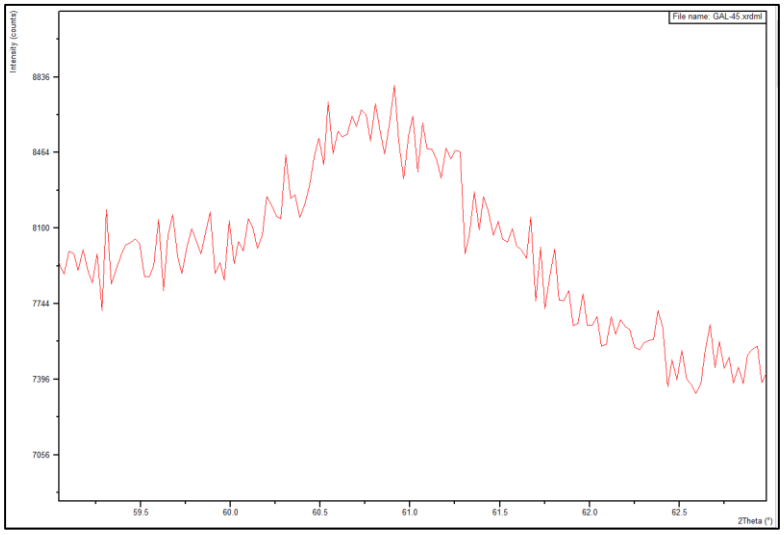

GA-L-99-45 XRD d060 Diffractogram

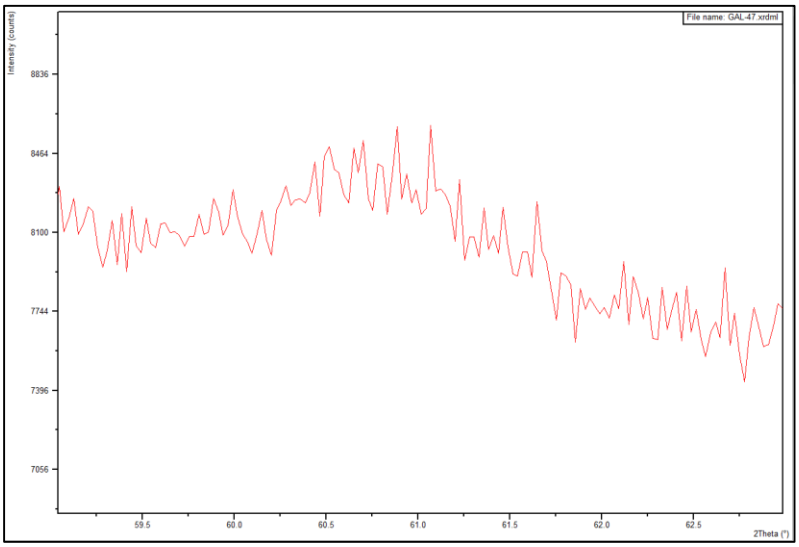

GA-L-99-45 XRD d060 Diffractogram

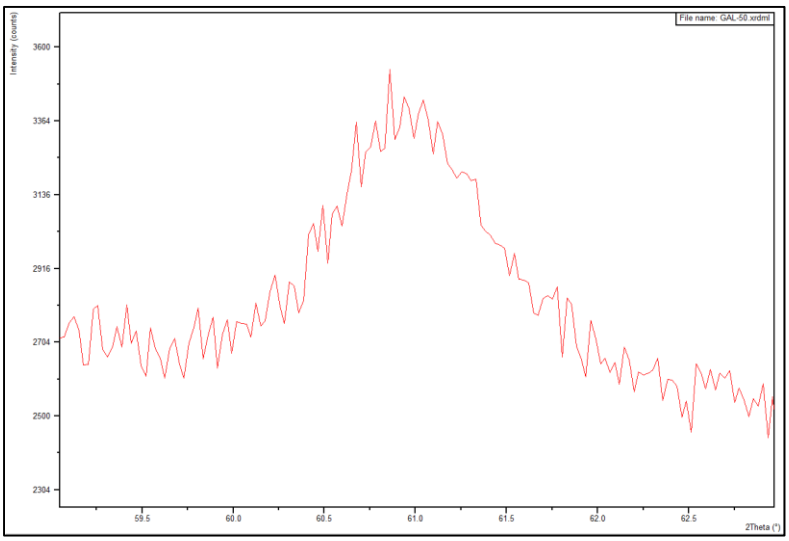

GA-L-99-50 XRD d060 Diffractogram

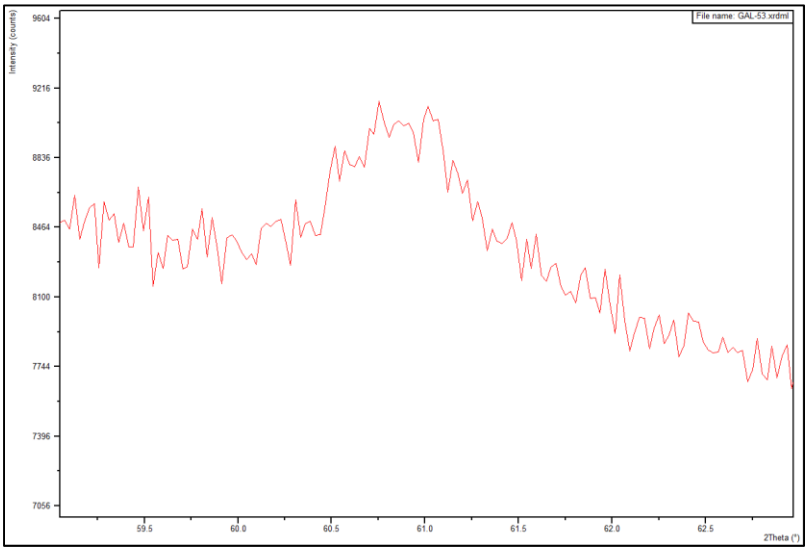

GA-L-99-53 XRD d060 Diffractogram

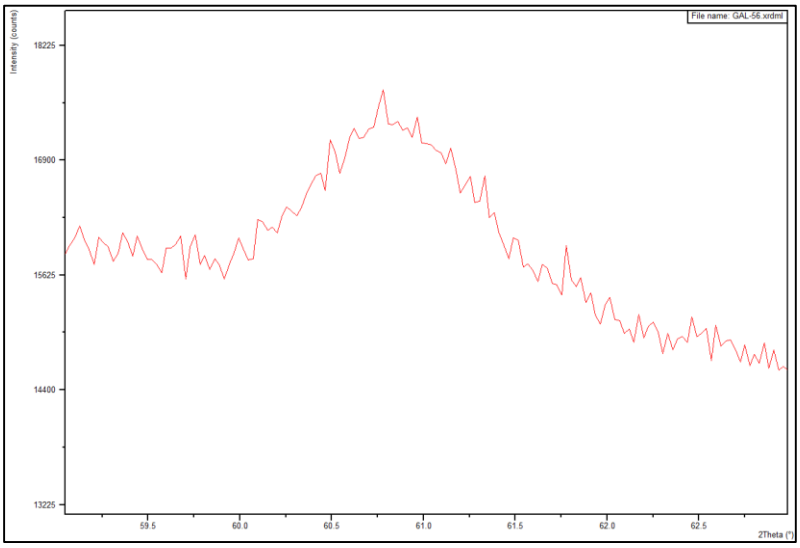

GA-L-99-56 XRD d060 Diffractogram

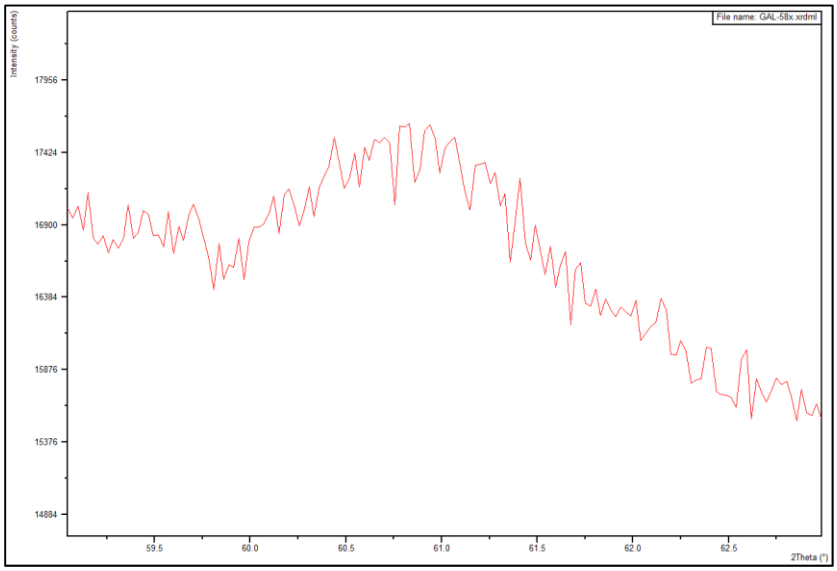

GA-L-99-58 XRD d060 Diffractogram

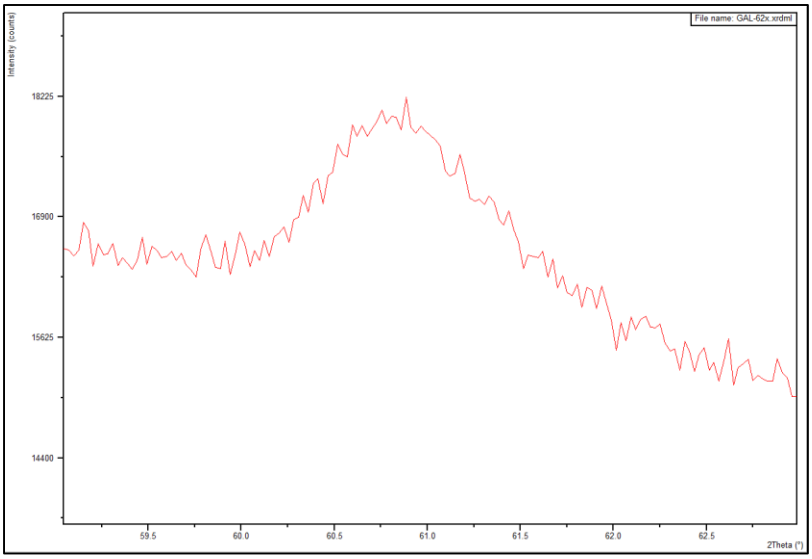

GA-L-99-62 XRD d060 Diffractogram

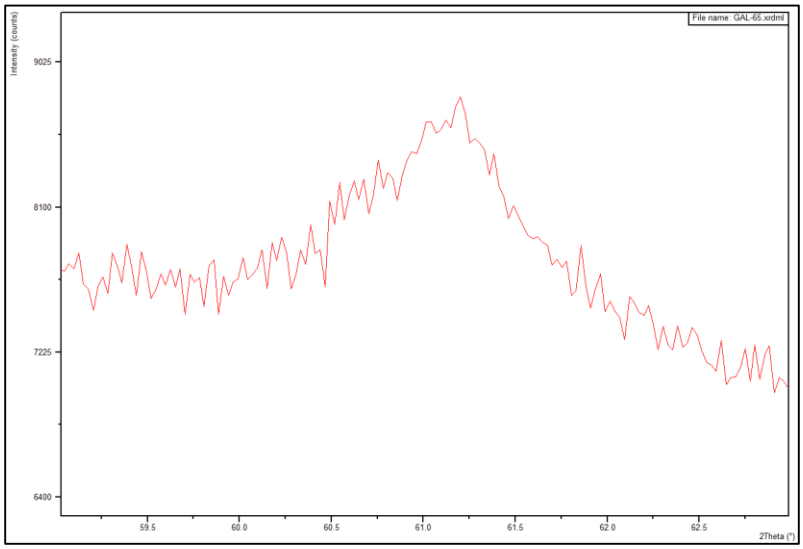

GA-L-99-65 XRD d060 Diffractogram

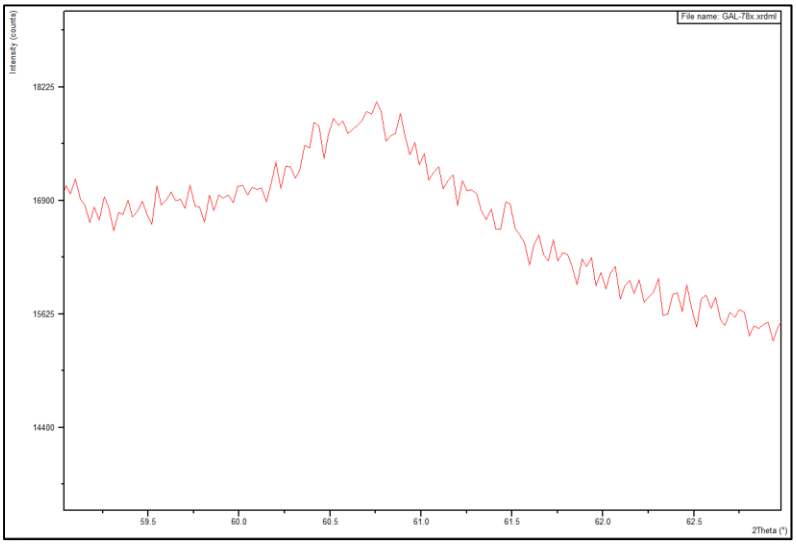

GA-L-99-78 XRD d060 Diffractogram

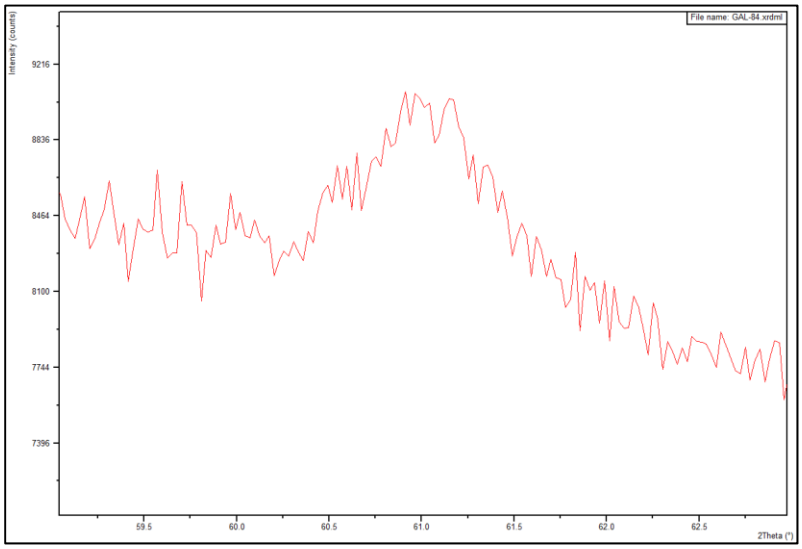

GA-L-99-84 XRD d060 Diffractogram

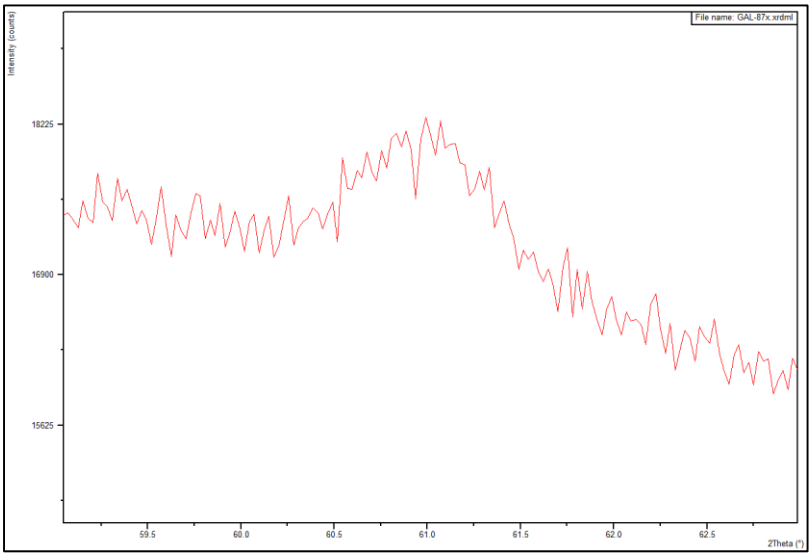

GA-L-99-87 XRD d060 Diffractogram

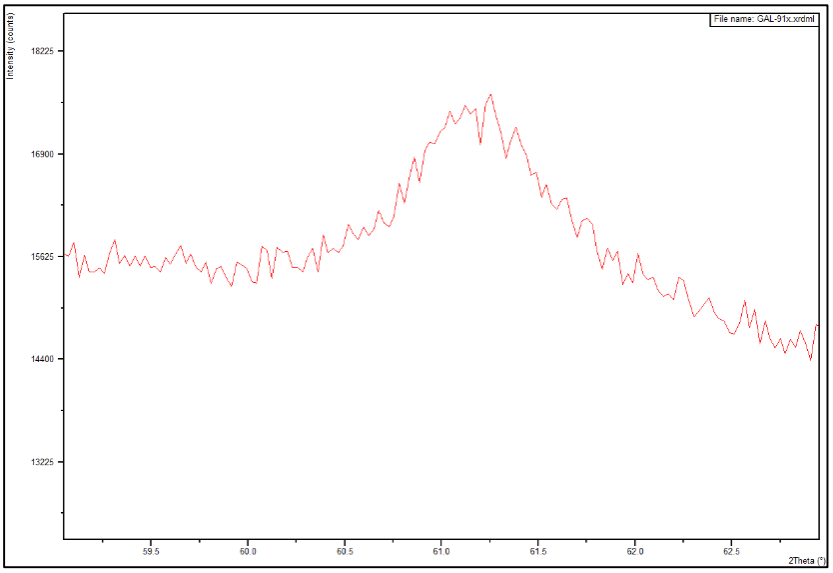

GA-L-99-87 XRD d060 Diffractogram

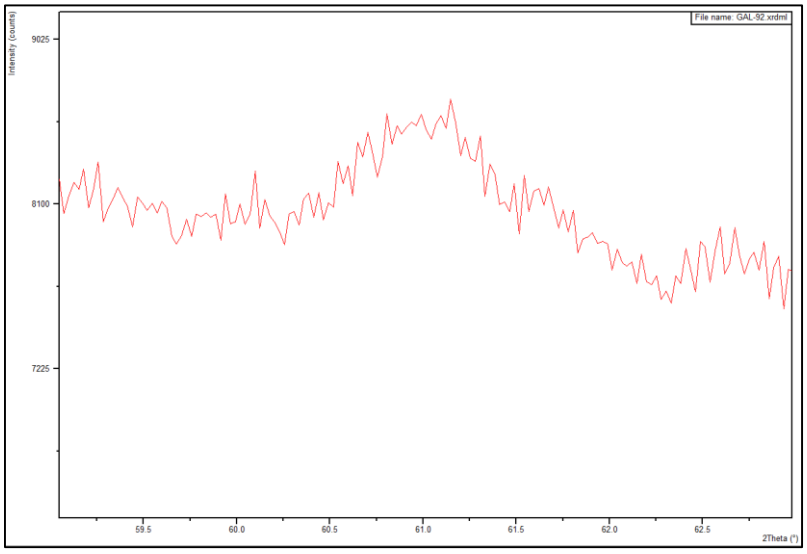

GA-L-99-91 XRD d060 Diffractogram

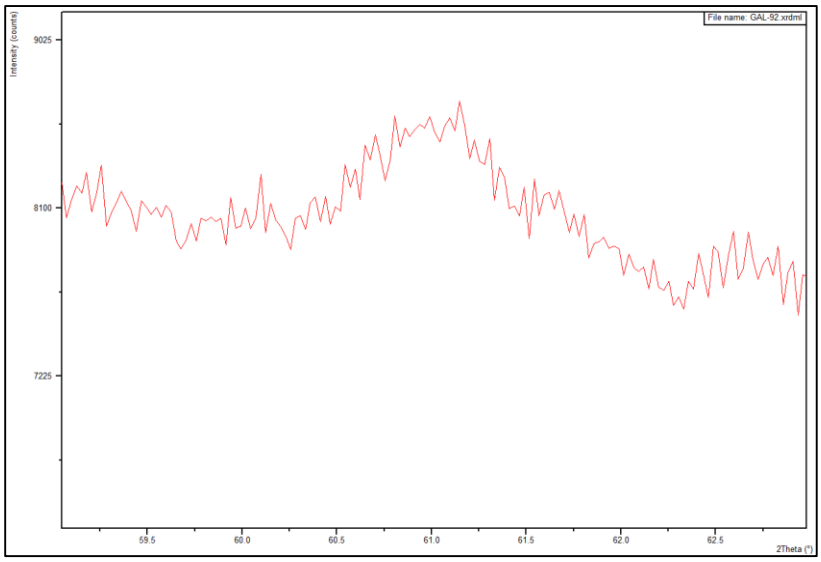

GA-L-99-92 XRD d060 Diffractogram

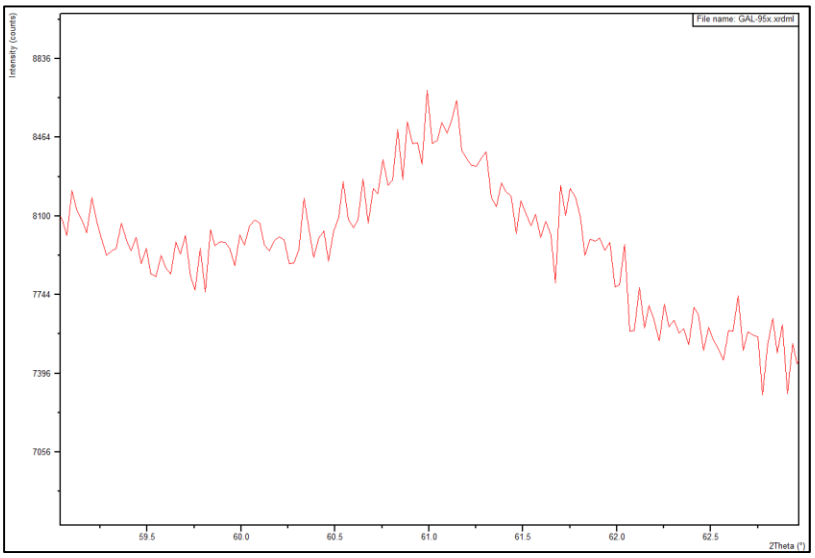

GA-L-99-95 XRD d060 Diffractogram

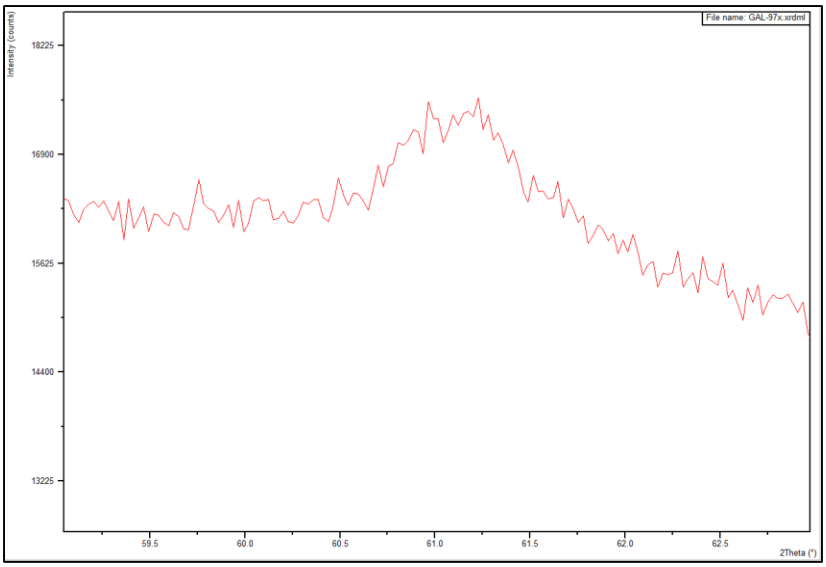

GA-L-99-97 XRD d060 Diffractogram

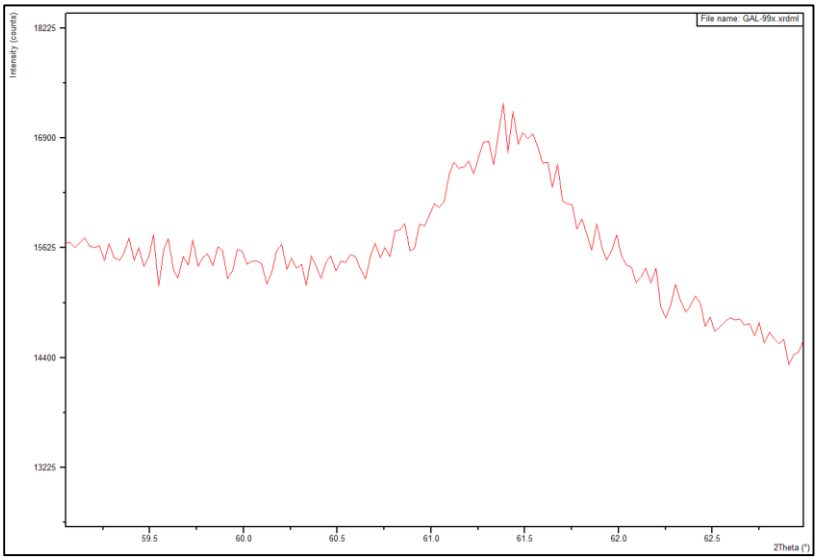

GA-L-99-99 XRD d060 Diffractogram

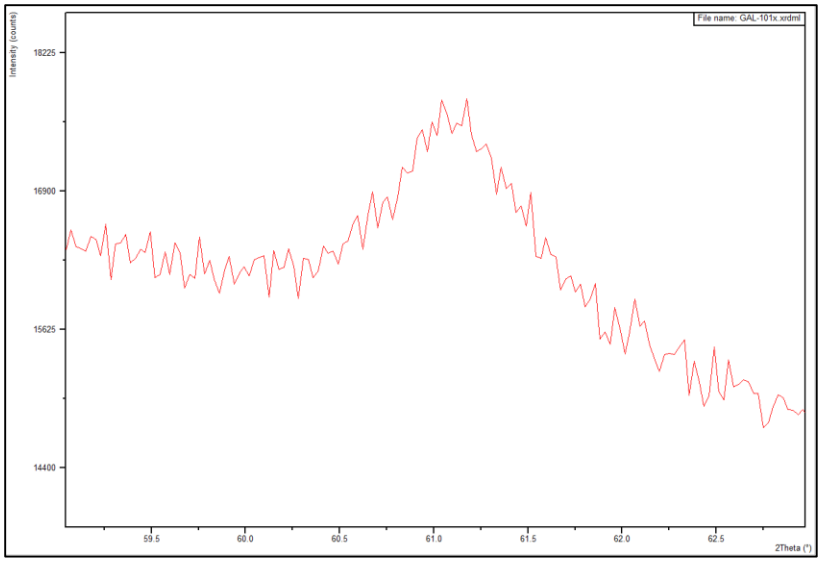

GA-L-99-101 XRD d060 Diffractogram

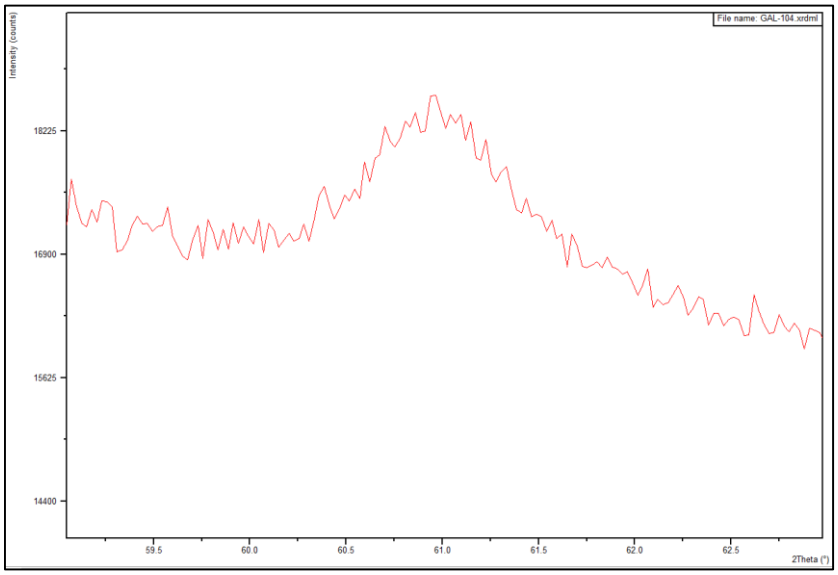

GA-L-99-104 XRD d060 Diffractogram

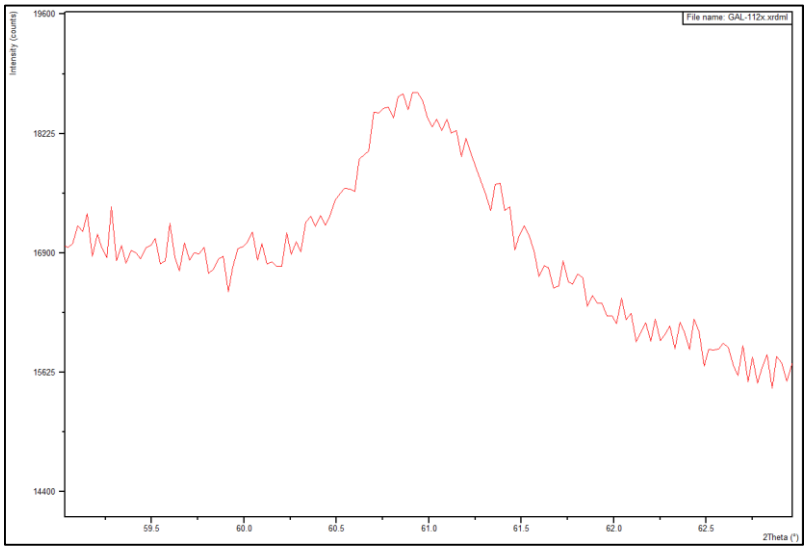

GA-L-99-112 XRD d060 Diffractogram

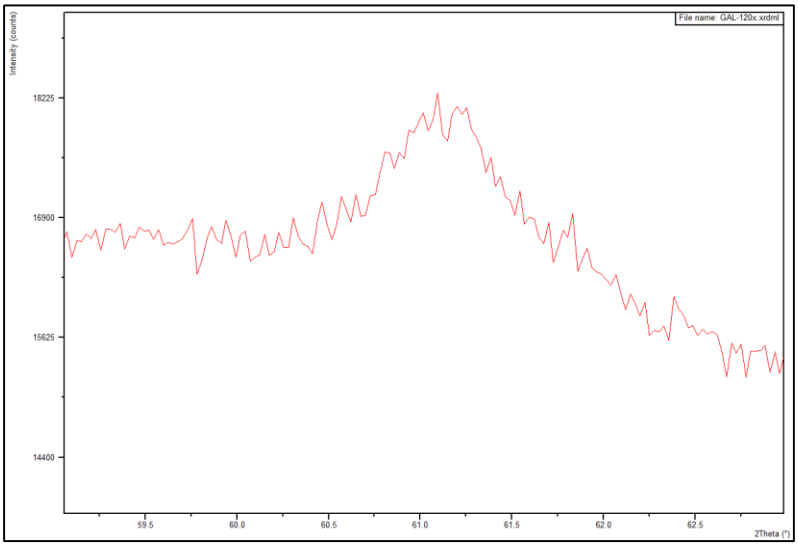

GA-L-99-120 XRD d060 Diffractogram

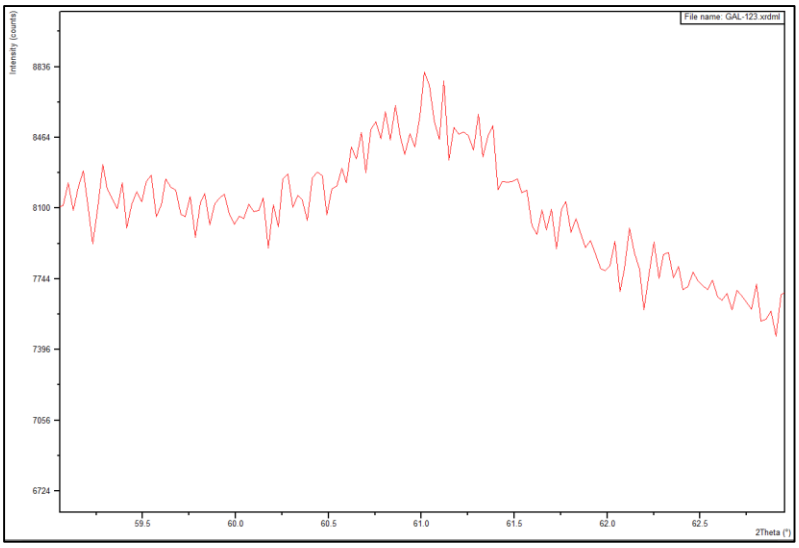

GA-L-99-123 XRD d060 Diffractogram

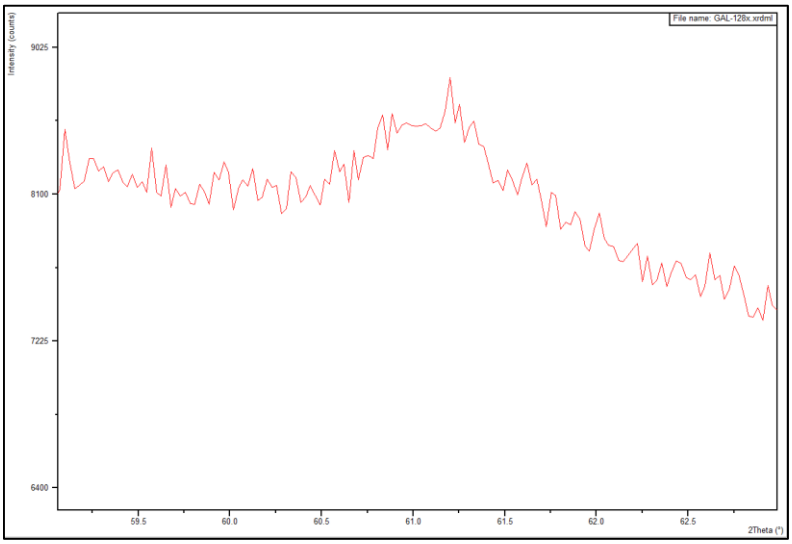

GA-L-99-128 XRD d060 Diffractogram

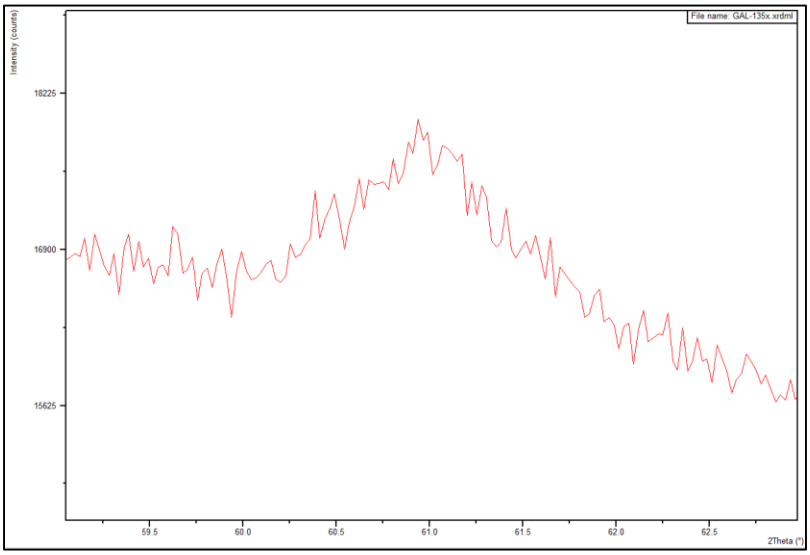

GA-L-99-135 XRD d060 Diffractogram

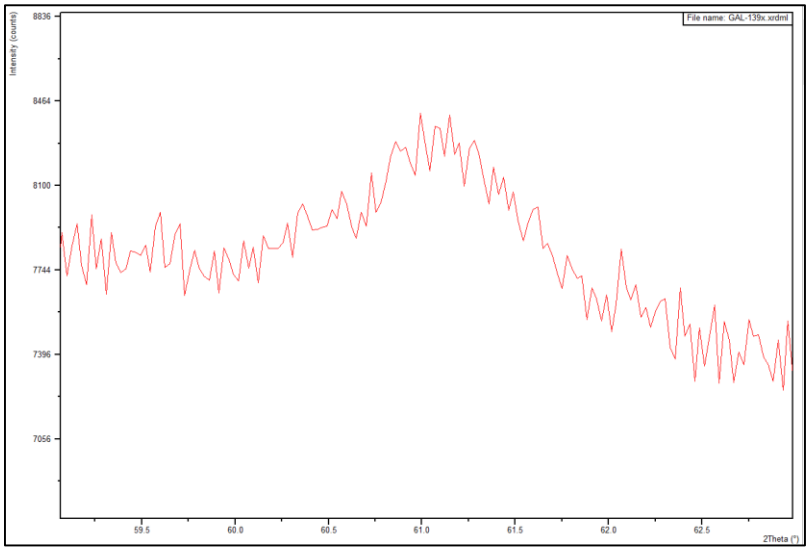

GA-L-99-139 XRD d060 Diffractogram

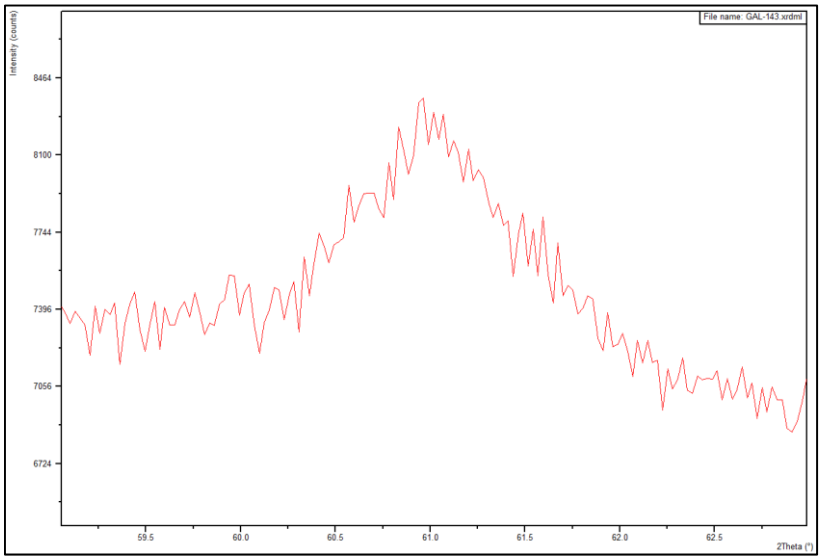

GA-L-99-143 XRD d060 Diffractogram

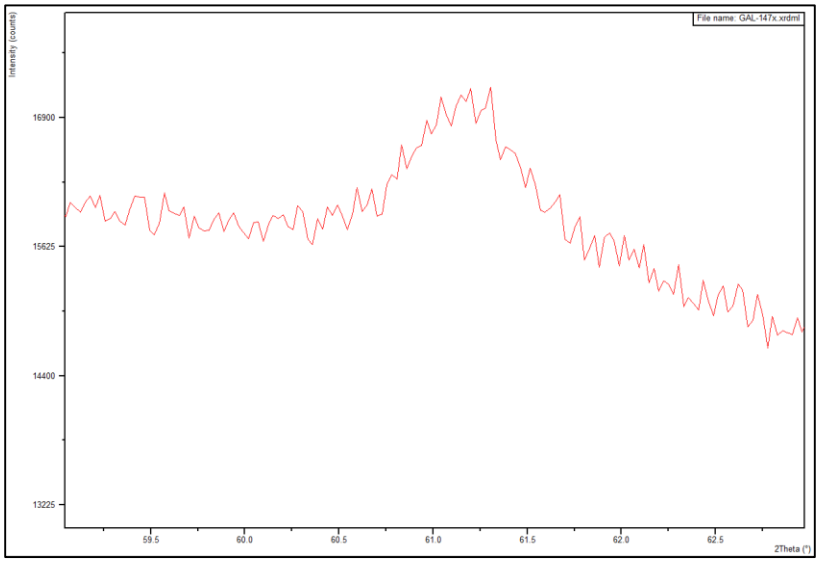

GA-L-99-147 XRD d060 Diffractogram

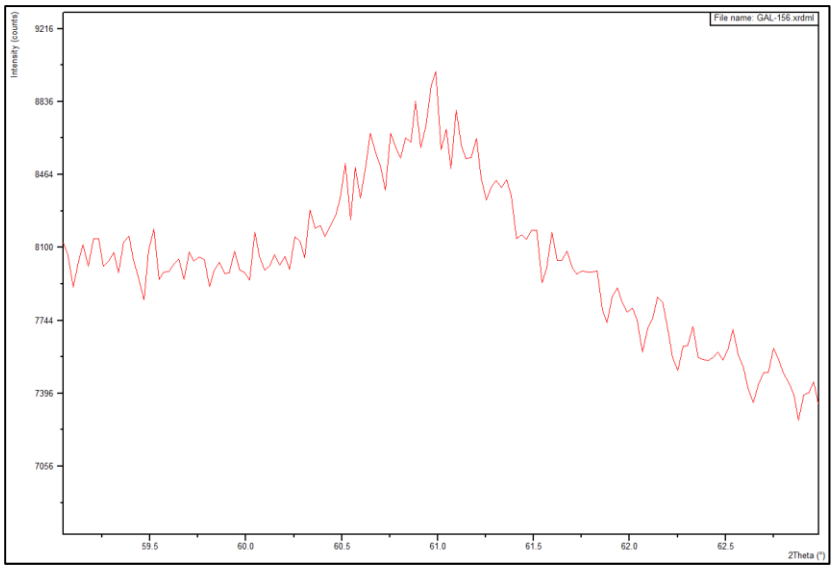

GA-L-99-156 XRD d060 Diffractogram

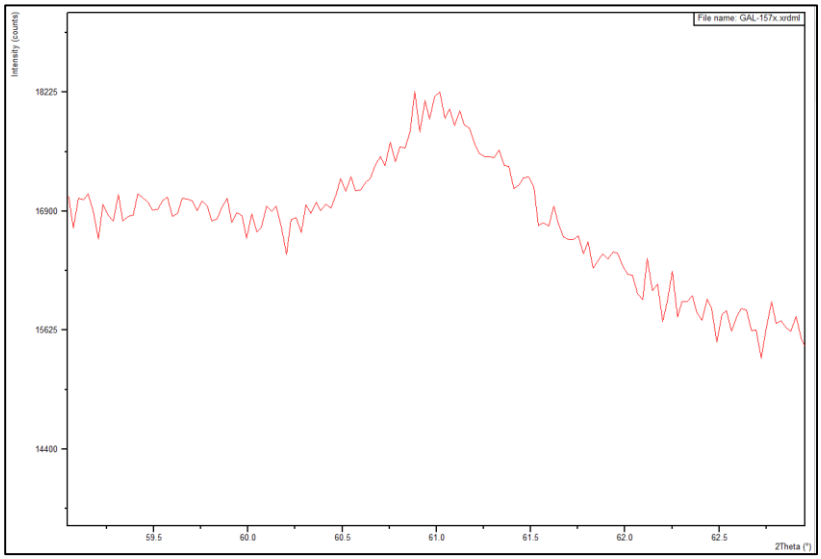

GA-L-99-157 XRD d060 Diffractogram

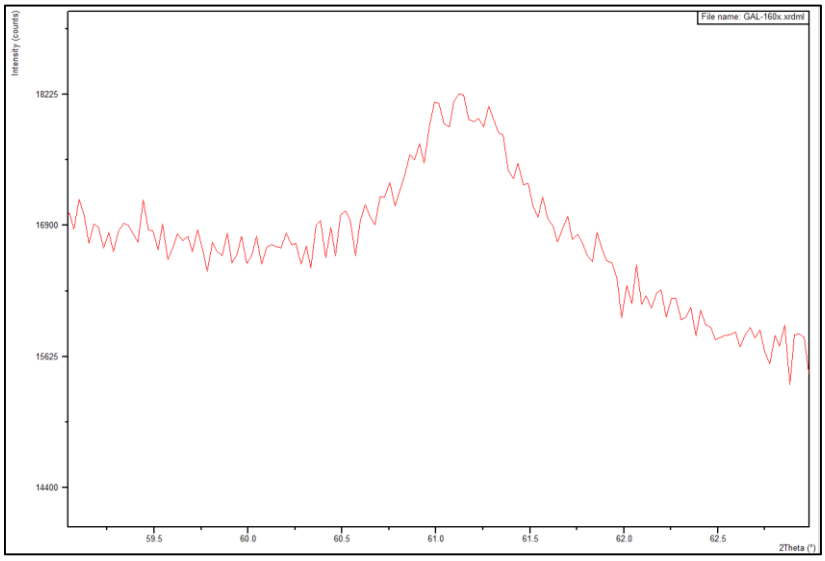

GA-L-99-160 XRD d060 Diffractogram

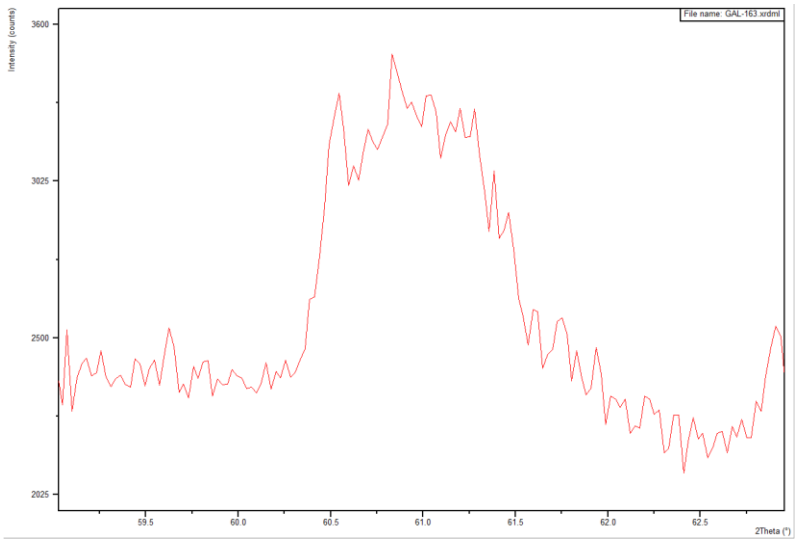

GA-L-99-163 XRD d060 Diffractogram

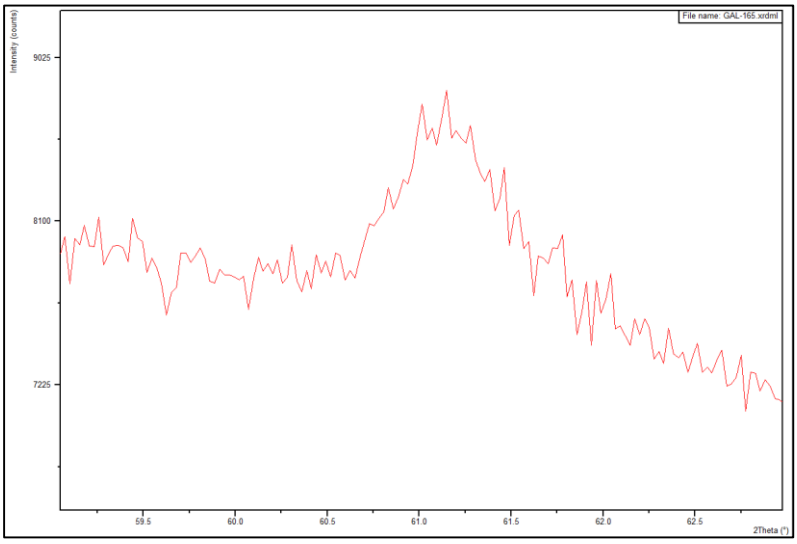

GA-L-99-165 XRD d060 Diffractogram